

Transdermal Delivery of Vaccines using Microneedle Array

Dissertation submitted in partial fulfillment of the requirements of

M.Tech. Project Stage I

By

Pinaki Chandra Dey

(Roll No: 113300003)

Under the supervision of

Prof. Rohit Srivastava

Prof. Siddhartha P. Duttagupta



Department of Biosciences and Bioengineering (BSBE)

Indian Institute of Technology Bombay

Mumbai - 400076

Oct, 2012



Department of Biosciences and Bioengineering (BSBE)
Indian Institute of Technology Bombay

Dissertation Approval for M.Tech. Project Stage I

This dissertation entitled **Transdermal Delivery of Vaccines using Microneedle Array** submitted by **Pinaki Chandra Dey** is approved for the completion of M.Tech Project Stage I.

Examiner:

Supervisor:

Chairman:

Date: _____

Place: _____

Acknowledgment

At the very onset I would like to convey my heartfelt gratitude to Prof. Rohit Srivastava for his continuous encouragement, support and critical suggestions throughout the course of this work. There were times when he kept on having faith in me, although I, myself, was a little apprehensive about the progress of my work; I truly appreciate that. It is only because of him I have generated a sheer interest towards this domain of science.

It might be the best opportunity to pay a tribute to Prof. Siddhartha P. Duttagupta for his unstinted support and technical guidance in numerous occasions. I have always enjoyed our frequent lively discussions which kept my interest and commitment towards my work high. It is only because of him I could have a chance to use modern day softwares like IntelliSuite™ for flawless simulation of my work before actual fabrication, which saved a lot of my time and effort.

A person, whom I will always be indebted to, is our beloved Mani madam. She has been guiding me since I was a novice in the CEN lab and still I find her as my last hope whenever I need any sort of logistical help.

I would also like to express my cordial appreciation to the seniors, staffs and officials in CEN facility viz. Ms. Jayasree, Ms. Neha Raorane, Ms. Manali Khare, Ms. Gayatri Vaidya, Ms. Divya N, Mr. Nikhilendu Tiwary, Mr. Arun Bhagwaniya, Mr. Sandeep SS, Mr. Sunil Kale, Mr. Dinesh Dixit, Mr. Prasenjit Ray, Mr. Swapnil Pandey, Mr. Tarkeshwar Patil, Mr. Shreyas Shyamsunder and above all Mrs. Satyavalli Paluri.

I cannot forget appreciating my friend Ms. Anjali Khatri for her motivation and technical advices and Mr. Ajay Sisodia for being the only person to accompany me from hostel to the lab every day.

And at last, I recall my mother's pain and sacrifice, in not seeing her son for last one year, and am forever indebted to her for bestowing upon me her blessings and providing me emotional support and determination. It is only because of her, which makes me what I am today and where I will be tomorrow.

At the end, I thank my sister and Divya, to whom I could hardly give any time since a year.

Declaration

I declare that this written submission represents my ideas in my own words and where others' ideas or words have been included, I have adequately cited and referenced the original sources. I also declare that I have adhered to all principles of academic honesty and integrity and have not misrepresented or fabricated or falsified any idea/data/fact/source in my submission. I understand that any violation of the above will be cause for disciplinary action by the Institute and can also evoke penal action from the sources which have thus not been properly cited or from whom proper permission has not been taken when needed.

(Signature)

Pinaki Chandra Dey

Roll No.: 113300003

Date: _____

Abstract

The skin, which has immunocompetent cells, is an attractive target for vaccine delivery. Transdermal immunization is the most effective immunization, though it requires considerable technical skills. A promising approach to transdermal immunization is microneedle array technology. Transdermal vaccination can offer simplified logistics and improved immunogenicity without the dangers posed by hypodermic needles. This report presents an insight into the transdermal route of drug and vaccine delivery (Chapter 1), followed by a comprehensive description of different fabrication methods for solid and hollow microneedles as well as various aspects of vaccination using these microneedles (Chapter 2). The current study also illustrates the development of microneedles by reactive ion etching (RIE), using an optimized novel recipe of gases and other parameter (Chapter 3 and 4).

Keywords:

Microneedles, Vaccine, Immunization, Transdermal delivery, MEMS, RIE, Influenza.

Table of Contents

Acknowledgment	i
Declaration	ii
Abstract	iii
Table of Contents	iv
List of Figures	vii
List of Tables.....	xi
PART I: INTRODUCTION	1
Chapter 1: Introduction.....	2
1.1. Introduction to vaccine.....	2
1.1.1. How vaccines work?	2
1.1.2. Types of vaccines	3
1.1.3. Vaccines and preventable diseases.....	3
1.2. Conventional methods of vaccine delivery	4
1.3. Limitations of conventional methods	5
1.4. Alternative methods of vaccine delivery.....	5
1.5. Transdermal delivery of vaccines.....	6
1.6. Role of microneedle in transdermal delivery of vaccines	6
1.7. Skin as a target site.....	7
1.7.1. Anatomy and immunology of skin.....	7
1.7.2. Mechanical properties of skin	8
1.8. Aim and scope of current studies	9
1.9. Significance of current study.....	9
PART II: LITERATURE REVIEW	10
Chapter 2: Review of Literature.....	11
2.1. History of microneedles	11
2.2. Microneedles in medical use	11
2.3. Classification of microneedles	12
2.3.1. Based on fabrication process.....	12
2.3.2. Based on geometry	12
2.3.3. Based on material	13
2.4. Different approaches of drug delivery by microneedles	14
2.5. Application of microneedles in vaccine delivery	15

2.6.	Fabrication of microneedles	17
2.6.1.	Solid microneedles	18
2.6.1.1.	Coated microneedles	18
2.6.1.1.1.	<i>Sharp-tip Chitosan-coated Silicon microneedles using RIE and Bosch Process</i>	18
2.6.1.1.2.	<i>Grooves-embedded microneedle arrays of bio-compatible polymer using hot embossing process</i>	19
2.6.1.1.3.	<i>Silicon microneedles array with Biodegradable tips using RIE and Anodization</i>	22
2.6.1.2.	Dissolving microneedles	25
2.6.1.2.1.	<i>Multilayered, Densely-Packed Dissolving Microprojection Arrays using DRIE and polymer casting</i>	25
2.6.1.2.2.	<i>Sharp-tip Tapered-cone Dissolving Microneedles made of Hyaluronic acid</i>	29
2.6.1.2.3.	<i>Biodegradable Polymeric Microneedles, having High Aspect-ratio, based on Micromolding</i>	31
2.6.2.	Hollow microneedles.....	37
2.6.2.1.	<i>Sharp-tip Cylindrical Silicon Microneedles with Side-openings using Bi-mask technique and DRIE</i>	37
2.6.2.2.	<i>Hollow Polymeric Microneedles using Integrated Lithographic Micromolding</i>	40
2.7.	Characterization of Microneedles	44
2.7.1.	Modeling, Simulation and Finite Element Analysis before fabrication	44
2.7.2.	Mechanical Analysis	51
2.7.3.	Flow Analysis.....	52
2.7.4.	CFD Analysis	53
2.8.	Delivery of vaccines using microneedle	54
2.8.1.	Coating of vaccines on microneedles	54
2.8.2.	Preparation of skin	56
2.8.3.	Penetration of skin.....	56
2.8.4.	Dissolution of microneedles and Release kinetics of vaccine	58
2.8.5.	Permeation studies.....	60
2.8.6.	Transport studies and Transdermal diffusion	62
2.8.7.	Stability of vaccine.....	63
2.8.8.	Characterization of immune responses.....	65
PART III: REPORT ON THE PRESENT INVESTIGATION.....		68
Chapter 3: Fabrication of Microneedles		69
3.1.	Desired characteristics of microneedles for vaccine delivery	69
3.2.	Design and Simulation	69
3.2.1.	Hollow Cylindrical Silicon Microneedles	69

3.2.2.	3D sharp-tip Hollow Silicon Microneedles	72
3.2.3.	Tapered-tip Solid Silicon Microneedles	76
3.2.4.	Chisel-tip Hollow SU-8 Microneedles	77
3.2.5.	In-plane Sharp-tip Silicon Microneedle	79
3.3.	Fabrication methodologies	81
3.3.1.	Fabrication of Hollow Cylindrical Silicon Microneedle Array	81
3.3.2.	Fabrication of Tapered-tip Solid Silicon Microneedle Array	83
Chapter 4: Results and Discussions		86
4.1.	Fabrication Results of Hollow Cylindrical Silicon Microneedle Array	86
4.2.	Fabrication Results of Tapered-tip Solid Silicon Microneedle Array	91
Chapter 5: Conclusions and Future Work		93
References		94

List of Figures

Sr. No.	Caption	Page
Figure 1.1	How Vaccines work	2
Figure 1.2	Anatomy of human skin	7
Figure 2.1	Structure and dimensions of the Out-of plane and In-plane micro-needles	12
Figure 2.2	SEM images of solid and hollow microneedles	13
Figure 2.3	Different approaches of drug delivery by hollow and solid microneedles	14
Figure 2.4	Methods of drug delivery to the skin using microneedles	17
Figure 2.5	Scanning electron micrograph shows stereoscopic view of a section of 20x20 microneedle array with 130- μ m height, 80- μ m base diameter, and 200- μ m spacing	19
Figure 2.6	Design and fabrication of grooves-embedded microneedles	20
Figure 2.7	SEM images of PLLA microneedle with its dimensions and dimensions of the master mold	21
Figure 2.8	SEM picture of the fabricated microneedle	22
Figure 2.9	Notching effect of reflected charges on the mask	23
Figure 2.10	Fabrication process	23
Figure 2.11	Fabrication process flow for the porous tips	24
Figure 2.12	Schematic view of the electrochemical anodization process and SEM image of the porous silicon tip	25
Figure 2.13	SEM images showing a) gold-coated silicon Nanopatch (NP) array template; b) cross-sectioned polydimethylsiloxane (PDMS) mold; c) corresponding dissolving Nanopatch(dNP) array comprising carboxymethylcellulose (CMC) with insert showing magnified image of a single projection; and d) graph showing the lengths of the template projections	26
Figure 2.14	Schematic of the fabrication process and dNPs fabrication	28

Figure 2.15	Fluorescent microscopy images showing rhodamine-dextran dNPs penetrating and dissolving in mouse ear skin	29
Figure 2.16	SEM image of a section of insulin-loaded microneedle arrays	31
Figure 2.17	Schematic of process to fabricate beveled-tip microneedles	34
Figure 2.18	Schematic of process to fabricate chisel-tip microneedles	35
Figure 2.19	Schematic of integrated lens process to fabricate tapered-cone microneedles	36
Figure 2.20	SEM images of (a) Beveled-tip PGA microneedles, (b) Chisel-tip PGA microneedles, and (c) Tapered-cone PGA microneedles	37
Figure 2.21	Process flow of the microneedle fabrication using bi-mask technique	39
Figure 2.22	SEM image of a single microneedle and a microneedle array	40
Figure 2.23	Schematic of fabrication process steps of polymer microneedles on preprocessed v-grooves	41
Figure 2.24	SEM of lithographically formed SU-8 microneedles formed on top of v-grooves	42
Figure 2.25	Multilevel SU-8 process with subsequent lithographic forming of a microfluidic back plate	43
Figure 2.26	Array of needles achieved by the lithographic molding process	44
Figure 2.27	Modeling of the Micro Needle as cantilever	45
Figure 2.28	Region of maximum stress in the (a) out-of-plane and (b) in-plane needles for buckling and bending forces, respectively	47
Figure 2.29	Variation of (a) Deflection and (b) Maximum stress with tip angle for out-of-plane needle	48
Figure 2.30	Variation of (a) Deflection and (b) Maximum stress with tip angle for in-plane needle	48
Figure 2.31	Variation of (a) deflection, (b) maximum stress and flow rate with needle bore area for out-of-plane needle	48
Figure 2.32	Variation of (a) deflection, (b) maximum stress and flow rate with needle bore area for in-plane needle	49
Figure 2.33	Bending stress analysis	50
Figure 2.34	Axial stress analysis	50
Figure 2.35	FEM simulation analysis for the stress of microneedle shaft.	51
Figure 2.36	Velocity and pressure distribution in CFD static analysis	53

Figure 2.37	Images of protein-coated microneedles of the three types of microneedles	55
Figure 2.38	Dissolving polymer microneedle patches	57
Figure 2.39	Piercing of 9×9 hollow silicon microneedle arrays across dermatomed human skin	58
Figure 2.40	Delivery to skin using microneedles	59
Figure 2.41	Influenza VLP vaccine delivery from coated microneedles into skin	60
Figure 2.42	(a) In vitro transdermal permeation of calcein (b) In vitro transdermal permeation of BSA in the matrix of chitosan loaded onto a microneedle array	61
Figure 2.43	Holes pierced across human cadaver skin.	62
Figure 2.44	Skin permeability to molecules and particles of different sizes after treatment with microneedles	63
Figure 2.45	Effect of PVP and lyophilization on vaccine immunogenicity	65
Figure 2.46	Microneedle immunization studies	66
Figure 3.1	Simulation of hollow cylindrical silicon microneedle array with backside reservoir	71
Figure 3.2	Mask layout	73
Figure 3.3	Simulation of hollow silicon microneedle array with 3D tip	75
Figure 3.4	Simulation of tapered-tip solid silicon microneedle array	76
Figure 3.5	Simulation of chisel-tip hollow SU-8 microneedles	78
Figure 3.6	Simulation of in-plane sharp-tip silicon microneedle array	80
Figure 3.7	Layout of 8 x 8 mask (dark-field) for pattern transfer onto SiO ₂	81
Figure 3.8	Schematic representation of fabricated hollow cylindrical silicon microneedle array (8x8)	83
Figure 3.9	Mask layout (bright-field) for pattern transfer onto SiO ₂	84
Figure 3.10	Schematic representation of fabricated tapered-tip solid silicon microneedle array (11x11)	84
Figure 3.11	Silicon etch-depth calculation	85
Figure 4.1	SEM image ($\alpha=60^\circ$) of a portion of the microneedle array showing height of an individual microneedle to be 65.35 μm	86
Figure 4.2	SEM image showing the diameter and area of the inner lumen of two individual microneedles	88

Figure 4.3	SEM image showing the outer diameter and total area of an individual microneedle	88
Figure 4.4	SEM image showing the center-to-center distance between two adjacent columns of microneedles	89
Figure 4.5	SEM image (bird's eye view) of an array of (8x8) hollow silicon microneedle arrays	89
Figure 4.6	Surface Profilometry of microneedle array showing feature heights of five individual microneedles	90
Figure 4.7	Surface Profilometry of microneedle array showing feature heights of five individual microneedles	91
Figure 4.8	Surface Profilometry of microneedle array showing tip diameter of an individual microneedle	92

List of Tables

Sr. No.	Title	Page
Table 1.1	Types of vaccines	3
Table 1.2	Vaccine-Preventable Diseases	4
Table 1.3	Vaccine Administration Site & Route	4
Table 2.1	Categories of Microneedles	14
Table 2.2	Main features of the different approaches of drug delivery by microneedles	15
Table 2.3	Overview of the lithographic parameters	42
Table 2.4	Hypotheses of microneedle induced protein degradation mechanisms, which may occur during protein delivery by microneedles	64
Table 3.1	Process sequence used in the simulation of hollow cylindrical silicon microneedle array fabrication	70
Table 3.2	Process sequence used in the simulation of 3D sharp tip hollow cylindrical silicon microneedle array fabrication using bi-mask technique	72
Table 3.3	Process sequence used in the simulation of tapered-tip solid silicon microneedle array fabrication	76
Table 3.4	Process sequence used in the simulation of chisel-tip hollow microneedles fabrication	77
Table 3.5	Process sequence used in the simulation of in-plane sharp-tip silicon microneedle array fabrication	79
Table 3.6	Process parameters for fabrication of hollow cylindrical silicon microneedle array	82
Table 3.7	Process parameters for fabrication of tapered-tip solid silicon microneedle array	84

PART I: INTRODUCTION

Chapter 1: Introduction

1.1. Introduction to vaccine

A vaccine is a product that produces immunity therefore protecting the body from the disease [1]. A vaccine is any preparation intended to produce immunity to a disease by stimulating the production of antibodies [2]. Vaccines include a suspension of attenuated or killed microorganisms or of antigenic proteins derived from them, administered for prevention, amelioration, or treatment of infectious diseases.

1.1.1. How vaccines work?

Vaccines work by mimicking disease agents and stimulating the immune system to build up defenses against them. The immune system protects the body from pathogens. Pathogens are covered with antigens that can trigger specific immune response. Vaccination exposes the body to antigens that are similar to the antigens found on a pathogen. By posing as a specific pathogen, the vaccine primes the immune system to respond with speed and intensity if the body encounters the pathogen in future.

Vaccine antigens are captured by Antigen Presenting Cells (APCs), such as dendritic cells, macrophages and B-cells; internalized, processed and presented by major histocompatibility complex (MHC), present on their surface, to the T-cell receptors (TCRs) of T-Cells, in turn activating them. These activated T-cells (T_h -cells) help in maturation of B-cells, which in turn produce antibodies specific to the vaccine antigen, and cytotoxic T-cells which are responsible for cell-mediated cytotoxicity [3].

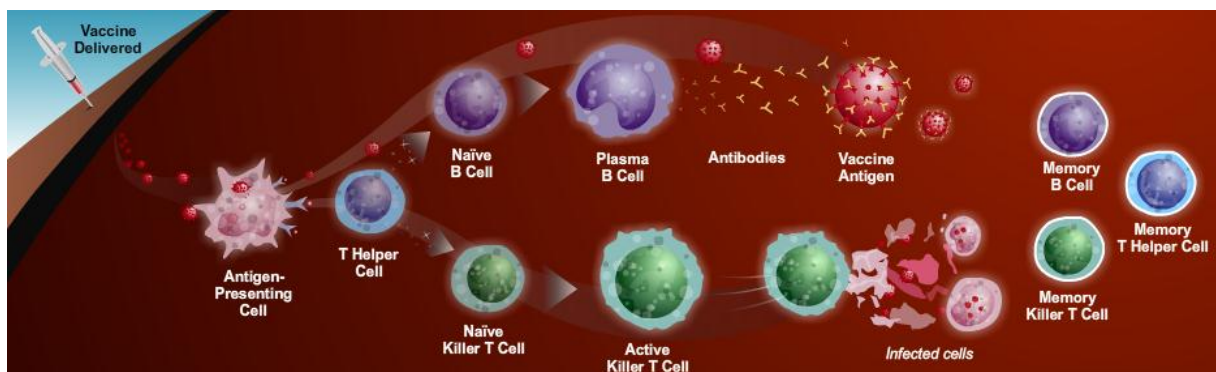


Figure 1.1: How Vaccines work [4]

Vaccination “programs” the immune system to remember a particular disease agent, by allowing it to elicit primary response against attenuated or killed form of pathogens, in the form of “memory B-cells and T-cells”. In case of future incidence of same pathogen, body elicits swift and intense “secondary immune response” to tackle the attack.

1.1.2. Types of vaccines

Vaccines can be differentiated into multiple groups based on their method of production. Table 1.1 represents different types of vaccines along with representative vaccines of those types, used in mainstream vaccination program [5].

Table 1.1

Types of vaccines

Vaccine type	Vaccines of this type on U.S. Recommended Childhood (ages 0-6) Immunization Schedule
Live, attenuated	Measles, mumps, rubella (MMR combined vaccine) Varicella (chickenpox) Influenza (nasal spray) Rotavirus
Inactivated/Killed	Inactivated poliovirus vaccine (IPV) Hepatitis A
Toxoid	Diphtheria, tetanus
Subunit/conjugate	Hepatitis B (recombinant vaccine) Human papillomavirus (HPV) Influenza (injection) <i>Haemophilus influenza</i> type b (Hib) Pertussis (subunit)

1.1.3. Vaccines and preventable diseases

Vaccine-preventable disease levels have been reduced significantly in last few decades. As per National Vaccine Policy of India, also known as Universal Immunization Programme (UIP), introduced in 1985 by Department of Health & Family Welfare Department, India; series of primary vaccination against *Bacillus Calmette-Guerin* (BCG), tetanus toxoid (TT), diphtheria (DPT), diphtheria toxoid (DT), oral polio vaccine (OPV), typhoid and measles is administered to every child before reaching the age of one year [6] [7]. Centers for Disease Control and Prevention (CDC), Department of Health and Human Services, U.S. recommends vaccination against the preventable diseases listed in Table 1.2 [8] [9].

Table 1.2

Vaccine-Preventable Diseases

Anthrax	Lyme Disease	Rotavirus
Cervical Cancer	Measles	Rubella (German Measles)
Diphtheria	Meningococcal	Shingles (Herpes Zoster)
Hepatitis A	Monkey pox	Smallpox
Hepatitis B	Mumps	Tetanus (Lockjaw)
<i>Haemophilus influenzae</i>	Pertussis (Whooping Cough)	Tuberculosis
type b (Hib)	Pneumococcal	Typhoid Fever
Human Papillomavirus	Poliomyelitis (Polio)	Varicella (Chickenpox)
(HPV)	Rabies	Yellow Fever
H1N1 Flu (Swine Flu)		
Influenza (Seasonal Flu)		
Japanese Encephalitis (JE)		

1.2. Conventional methods of vaccine delivery

A vaccine administration may be oral, by injection (intramuscular, intradermal, and subcutaneous), by puncture, transdermal or intranasal [10]. Table 1.3 illustrates the sites and routes of administration of conventional vaccines [11].

Table 1.3

Vaccine Administration Site & Route

Route	Site	Vaccines
Oral (PO)	One side of the inside of the cheek (between the cheek and gum) toward the back of the mouth.	Rotavirus(RV1/Rotarix, RV5/RotaTeg), Oral typhoid (TY21a/Vivotif), Inactivated poliovirus vaccine (IPV)
Intranasal (NAS)	Into both the naris using a special sprayer device. Dose: 0.2 mL.	Live Attenuated Influenza Vaccine (LAIV, FluMist)
Subcutaneous (SC)	Left/Right AnteroLateral Fat of Thigh (LALT/RALT) for infants. Left/Right Posterolateral Fat of Upper Arm (LPUA/RPUA) for children and adults. Needle Size 23-25g, 5/8"	Measles, Mumps, Rubella (MMR) Meningococcal polysaccharide (MPSV4) Pneumococcal polysaccharide (PPV) Polio, inactivated (IPV) Varicella (Var)

Intramuscular (IM)	Left/Right Vastus Lateralis (LVL/RVL) for infants. Left/Right Deltoid (LD/RD) for children and adults. Needle Size 22-25g, 1-2"	Diphtheria, Tetanus, Pertussis (DTaP, DT, Tdap, Td) Haemophilus influenzae B (Hib) Hepatitis A (HepA) Hepatitis B (HepB) Influenza, trivalent inactivated (TIV) Meningococcal conjugated (MCV4) Pneumococcal Conjugate (PCV7) Pneumococcal Polysaccharide (PPV) Polio, inactivated (IPV)
Intradermal (ID)	Deltoid region of upper arm. Needle Size 30g, 1.5 mL. Dose: 0.1 mL	Fluzone

1.3. Limitations of conventional methods

Delivery methods of majority of the vaccines involve the use of hypodermic needle which comes with its own limitations causing pain, anxiety, patient discomfort, tissue damage, possible infection and needle phobia. Inappropriate use of needle, mostly in IM mode of administration, causes 5 accidental sticks per 100 worldwide [12]. The needle-free mode of administration is only limited to a few sets of vaccines and have its own limitation, such as degradation and inefficient absorption [13]. All of the modes of administration of vaccines illustrated in Table 1.3 require trained professionals, which is a crucial drawback in rural areas. Injection practices incur huge costs and complexity for safe disposal of sharps needles and these waste disposal practices are often hazardous [7].

These limitations have led to extensive research and development of alternative methods for vaccine delivery across the skin.

1.4. Alternative methods of vaccine delivery

Needle-free, painless, easy to administer mode of vaccine delivery is the need of the hour to achieve complete immunization. Intensive research is in progress in developing and testing alternative modes for vaccine delivery, such as, transdermal delivery [14] [15], electroporation, live bacterial vaccines [16] and oral delivery of lipid coated protein antigens [17].

1.5. Transdermal delivery of vaccines

Transdermal mode of delivery of vaccines, across the skin, bears rich prospect in replacing conventional needle-based mode of delivery. The skin immune system arises from cellular and humoral components of the epidermis and the dermis. Among the most important components of the skin immune system are the Langerhans cells, which are specialized Antigen Presenting Cells (APCs), found in the viable epidermis. The Langerhans cells detect and internalize antigens, and carry them to draining lymph nodes where they are presented to T-cells, invoking an immune response [13]. The incidence of such APCs is much higher just beneath the epidermis than that in the underlying dermis or muscular layer.

Jet injectors deliver can deliver vaccines through high-speed pressurized liquid penetration of the skin without a needle. But, such devices are costly and require sophisticated control, resulting in their limitation in wide public use [14].Antigens can be delivered in solid form which is more stable and does not require cold storage. Gold particles coated DNA vaccine in solid form has been delivered successfully [18].Recent trends in fabricating microstructured microneedle arrays, using technologies conventionally used for microelectronics and VLSI fabrication, has proven the tremendous prospects of such devices and put them in the forefront as the alternative needle-free painless mode of vaccine delivery.

1.6. Role of microneedle in transdermal delivery of vaccines

Microneedles and other nano-/micro-structured transdermal systems are highly efficient in delivering vaccines in close proximity to the antigen presenting cells in the epidermis [53], and thus it is possible to achieve excellent immune response with smaller quantities of antigen than used in subcutaneous injection. The small size of microneedles causes comparatively less mechanical trauma to the skin and these are painless upon insertion. Arrays of vaccine-coated microneedles are typically held within a patch that secures them against the skin; vaccine is released once these penetrate the epidermis layer of the skin [13] [15].It causes no pain induction as the needles have a short length and they do not arrive at nerves in deeper dermis layer.

1.7. Skin as a target site

Skin makes an excellent site for drug and vaccine delivery due to easy accessibility, immunosurveillance functions, avoidance of macromolecular degradation in the gastrointestinal tract and possibility of self-administration.

1.7.1. Anatomy and immunology of skin

The outer section of the skin is the epidermis, made of stratified squamous epithelium (Figure 1.2), is usually about 50-150 μm thick [63], non-vascular and nourished by tissue fluid from the inner region of the skin [19].

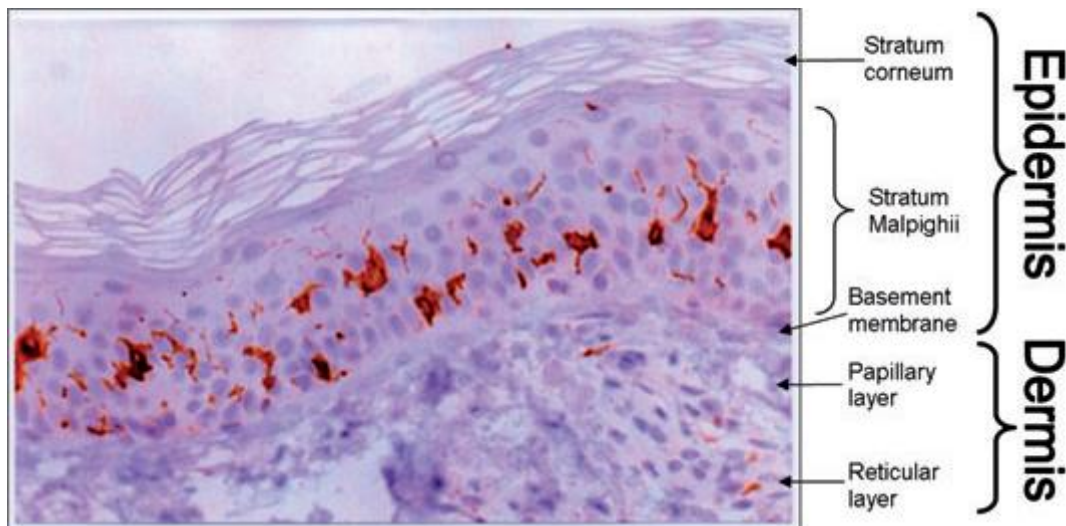


Figure 1.2: Anatomy of human skin. Activated Langerhans cells (dark stain) within epidermal Malpighian layer 48 hours after immunization by application of cutaneous patch containing heat-labile enterotoxin (LT) of *E. coli*. (Photograph from G.M. Glenn et al. "Transcutaneous immunization: a human vaccine delivery strategy using a patch." *Nature Medicine*, vol. 6, issue.12, pp. 1403–1406, 2000 (Fig. 3b, page 1405))

Epidermis serves both a structural function in limiting the passage of water and other molecules, due to the presence of keratinohyalin; and an immunologic role[20] [21]. The outermost dead layer of the epidermis, 10-15 μm thick and made of keratinocyte cells, is the stratum corneum. These cells are flat, hexagonal shaped with diameter of approximately 30 μm . This layer provides epidermis its characteristic toughness and barrier functionalities towards water and germs. Stratum corneum is the principal obstacle to the introduction of vaccine antigen for transdermal vaccination. The innermost layer of epidermis is known as stratum germinativum and is composed of columnar cells. The cells of this region are active and hence multiply [19]. Below the epidermis and basement membrane lies the dermis, about 1.5 to 3 mm

thick, in which fibroblasts, fine collagen, elastic fibers and most skin organelles are found, including small blood vessels, lymphatic vessels, nerves, hair follicles, sweat and sebaceous glands. The subcutaneous tissue below is referred to as the hypodermis and consists primarily of fat and varies widely in thickness among different body surfaces and, of course, individuals. Faster passive diffusion of therapeutic substances transcellularly through the dead and living keratinocytes, and via intercellular channels between them, correlates with smaller molecules (<500 Da), lower melting points, increased lipophilicity (and correspondingly lower water solubility), higher (saturated) concentrations, and the scarcity of side groups, that form hydrogen bonds, slow that diffusion [22] [23].

Upon stimulation by vaccine antigens, keratinocytes can produce pro-inflammatory cytokines (Interleukin 1 or IL-1) and can themselves function as antigen-presenting cells by displaying major histocompatibility complex (MHC) class II antigens (HLA-DR), as well as intercellular adhesion molecules (ICAM-1) [24]. Epidermal Langerhans cells are believed to play a key role in cutaneous immunization, although other well-known immune system players also circulate or reside in the epidermis or dermis, such as CD8+ and CD4+ T lymphocytes, mast cells, macrophages, and dermal dendritic cells.

The immature Langerhans cells reside among the keratinocytes in the epidermis, comprising about a quarter of the skin surface area, where they efficiently capture foreign antigen by phagocytosis or endocytosis. As with similar dendritic cells in other tissues, upon activation these professional antigen-presenting cells (APC) process the antigen as they migrate to draining lymph nodes. There, now mature, they express high levels of class II MHC molecules, and present the antigen brought from the skin to T helper (Th) lymphocytes, a critical step for the subsequent immune responses orchestrated by the latter cells, such as B-cells [22].

1.7.2. Mechanical properties of skin

Human skin is a complex tissue consisting of several distinct layers, each consisting of their own components and structure. Skin behaves as a non-homogeneous, anisotropic, non-linear viscoelastic material subjected to a pre-stress. Experimentally obtained Young's moduli of the layers vary considerably ($E_{\text{stratum corneum}} \approx 1000 \times E_{\text{dermis}}$) [25]. Maximal elastic modulus (Y_{max}) for human skin lie within the range $2 \times 10^3 \text{ Ncm}^{-2}$ to $11 \times 10^3 \text{ Ncm}^{-2}$ of cross-sectional area. The elastic modulus increase with age of the individual and appears to be lower in females

than in males [26]. Theoretically human skin resistance is 3.18 MPa while penetrating the skin [27]. Once the skin has been penetrated, the pressure reduces to 1.6 MPa [28].

1.8. Aim and scope of current studies

In the present study a thorough critical review of previously reported works and progress on transdermal vaccine delivery will be presented. Feasibility studies and materialization of different fabrication approaches for microneedle manufacturing shall be investigated along with their suitability in transdermal vaccination. A comparative analysis of efficacy of different vaccines, their stability upon administration and capability to induce immune response is also the matter of interest. This study aims to provide a proven MEMS-based delivery device template for extension into human studies, which could uniquely address the problems of vaccination by alleviating needle-phobia and the need for trained practitioners to administer vaccines.

1.9. Significance of current study

Use of microneedle in transdermal vaccination is still in its research stage. There are very few marketed products which use microneedles for drug delivery to skin. Vaccination using low-cost disposable microneedle array can greatly increase its reach to the developing countries such as ours. A painless, self-administrable, fast and robust mode of drug and vaccine delivery is the need of this century, when patient compliance is a vital factor in medical and pharmaceutical field. Present study will come up with inexpensive fabrication methods to batch-fabricate low-cost microneedle array devices for vaccination. These devices, if marketed, can reach the mass, primarily the poorer parts of the world, and can significantly increase the incidence rate of timely vaccination and eradication of vaccine-preventable diseases.

PART II: LITERATURE REVIEW

Chapter 2: Review of Literature

2.1. History of microneedles

Microneedles are micron-scaled needles that are so small (20-1000 μm), that they are able to painlessly penetrate the skin. Microneedles were first conceptualized for drug delivery many decades ago, but only became the subject of significant research starting in the mid-1990's when microfabrication technology enabled their manufacture as (i) solid microneedles for skin pretreatment to increase skin permeability, (ii) microneedles coated with drug that dissolves off in the skin, (iii) polymer microneedles that encapsulate drug and fully dissolve in the skin and (iv) hollow microneedles for drug infusion into the skin [29]. Fabrication methods of microneedles were the major concern of researchers in the early years as the fabrication technology was increasing. But now the major concern has been shifting to testing of microneedles in-vivo and in-vitro, analyzing the strength of microneedles and its biocompatibility and related issues.

2.2. Microneedles in medical use

Microneedles have been used to deliver a broad range of different low molecular weight drugs, biotherapeutics and vaccines [29]. Influenza vaccination using a hollow microneedle is in widespread clinical use [30] [31] and a number of solid microneedle products are sold for cosmetic purposes [32]. In addition to applications in the skin, microneedles have also been adapted for delivery of bioactives into the eye [33] and into cells [34]. Successful application of microneedles depends on device function that facilitates microneedle insertion and possible infusion into skin, skin recovery after microneedle removal, and drug stability during manufacturing, storage and delivery, and on patient outcomes, including lack of pain, skin irritation and skin infection, in addition to drug efficacy and safety. Building off a strong technology base and multiple demonstrations of successful drug delivery, microneedles are poised to advance further into clinical practice to enable better pharmaceutical therapies, vaccination and other applications.

2.3. Classification of microneedles

2.3.1. Based on fabrication process

The microneedles are classified as in-plane and out-of-plane microneedles based on the fabrication process (Figure 2.1) [28]. In in-plane microneedles, the microneedle shaft is parallel to the substrate surface. Length and high aspect ratio can be precisely obtained but it is difficult to make 2-D array of in-plane microneedles. In out-of-plane microneedles, the length of the microneedles protrudes out of the substrate surface. It is easy to fabricate a 2-D array of out-of-plane microneedles but length and high aspect ratio is a challenge [38].

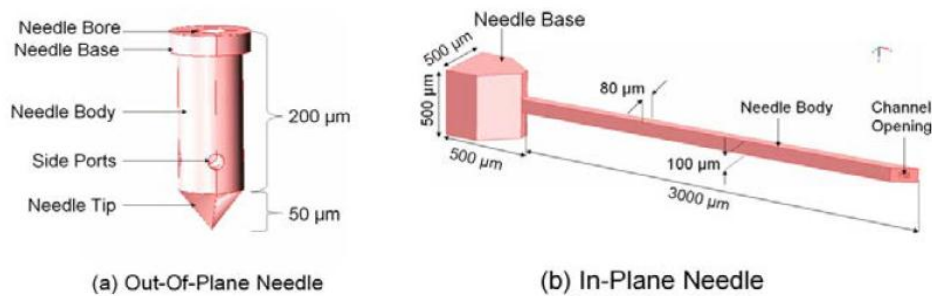
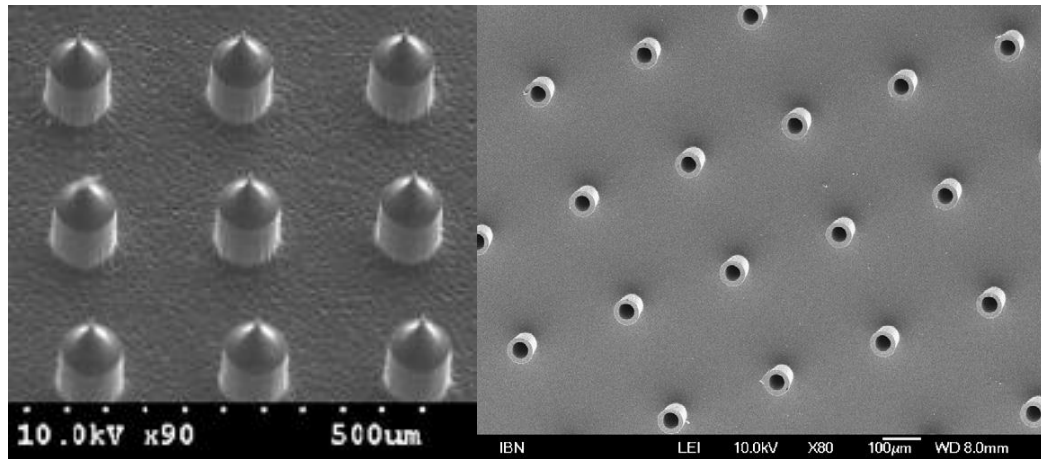


Figure 2.1: Structure and dimensions of the Out-of plane and In-plane micro-needles [28].

2.3.2. Based on geometry

According to the geometry, the microneedles can be solid or hollow (Figure 2.2). In hollow microneedles, an internal lumen is present which allows flow of fluid and macromolecules through the microneedles, which can be easily controlled using a micropump [37]. Solid microneedles are useful as biodegradable needles and with needles having drug pre-coated on them. Drug release will be passive depending upon the rate of degradation or dissolution of drug into the body [38].



(a) Solid microneedle

(b) Hollow microneedle

Figure 2.2: SEM images of solid [35] and hollow [36] microneedles.

2.3.3. Based on material

Microneedles can be classified based on the materials they are made of. The first produced microneedles for drug delivery were made from silicon wafers by photolithography and deep reactive ion etching [39]. Silicon micromachining uses the already rich technologies developed for the production of integrated circuits, which can enable highly-reproducible mass production of silicon microneedles. Prospect of easy integration of silicon microneedles with other devices, such as, micropumps and sensors, is driving the research trends in current microneedle technology. Although, it is easy to fabricate sharp tip microneedles of good aspect ratio from silicon, the cost of fabrication process and fragile nature of silicon, causing breakage upon insertion, added with its non-biodegradable and non-biocompatible nature are limiting its widespread use in medical aspects. Microneedles made of metals, such as titanium [40], stainless steel [41], can meet the need of biocompatibility and mechanical strength. Polymeric microneedles, made of materials like SU-8 [42], PGA [42], Hyaluronic acid [43], have been found to be beneficial over microneedles made of other materials, because polymers are inexpensive, can be biocompatible, and they are amenable to mass production. Furthermore, viscoelastic nature of polymeric microneedles makes them less sensitive to shear-induced breakage, and drugs may be incorporated into biodegradable polymeric microneedles for controlled drug delivery [39].

Microneedles also vary according to structure, tip shape and overall shape. The details of microneedles categories are shown in Table 2.1 [27].

Table 2.1

Categories of Microneedles

Material	Structure	Tip shape	Overall shape	Medical Application
Silicon	Solid	Beveled tip [44]	Cylindrical	Vaccine delivery
Silicon dioxide	Hollow	Chiseled tip [44]	Pyramidal	Drug delivery
Glass	In-plane	Tapered tip [44]	Spear	Fluid extraction
Metals	Out-of plane	3-D tip [42] [45]	Spike	Micro-dialysis
Polymer			Square	Electro-diagnostics Sensing

2.4. Different approaches of drug delivery by microneedles

There are three main mechanisms by which microneedles can be used to deliver drugs into the skin, which include the “poke and flow” approach, “poke and patch” approach, the “poke and release” approach, and the “coat and poke” approach, as schematically shown in Figure 2.3 [39]. The advantages and limitations of each of the methods are illustrated in Table 2.2 [39].

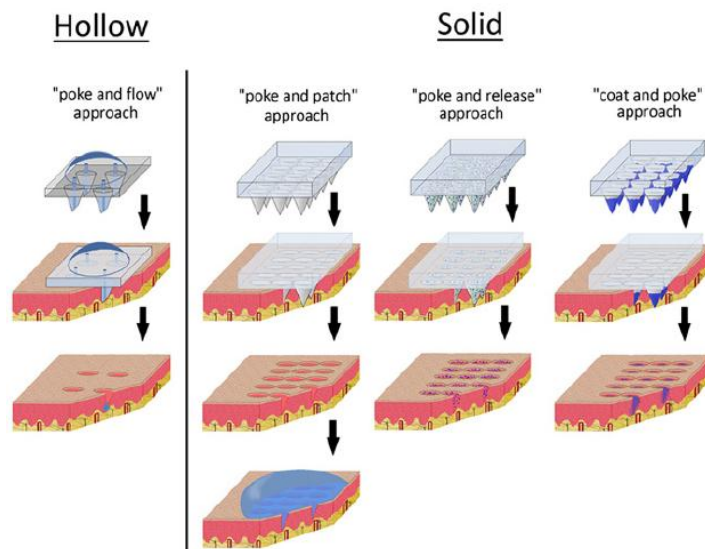


Figure 2.3: Different approaches of drug delivery by hollow and solid microneedles [39].

Table 2.2

Main features of the different approaches of drug delivery by microneedles

Drug delivery approach	Rate-limiting step of drug delivery	Main advantages	Main disadvantages
“poke and flow”	Solvent flow through microchannel. Pressure resistance of the skin.	Rate of drug delivery can be regulated. Delivery of high volumes. Integration into lab-on-a-chip systems. Precise dosing.	Risk of clogging. Impaired microneedle strength. Increased risk of leakage for arrays. More complex device.
“poke and patch”	Diffusion of the drug through the micropores. Dependent on the pore size and number, and concentration of the drug	Technically simple. Extended release.	Low fraction of the drug may be delivered. Two-step administration process. No precise dosing. Reformulation of the drug needed.
“poke and release”	Dissolution rate of dissolving microneedles.	Least wastage of drug. No sharp waste (dissolving microneedles). Precise dosing.	Impaired microneedle strength. Decreased penetrability. Small dose. Reformulation of the drug needed.
“coat and poke”	Detachment of the coating from microneedle surface. Dissolution rate of the coating.	Microneedle strength is retained after coating. Precise dosing. No patch required.	Requires an efficient coating procedure. Small dose. Reformulation of the drug needed. Reduction of microneedle sharpness/penetrability.

2.5. Application of microneedles in vaccine delivery

Vaccination using microneedles is especially attractive because it simplifies vaccine distribution and improves patient compliance, and also enables targeting of vaccine antigen to the skin, which offers immunologic advantages over conventional intramuscular injection, but until now there have not been any simple, reliable methods to vaccinate in the skin. Microneedles—both solid microneedle patches and hollow microneedles for intradermal injection—address this limitation and can make skin vaccination a practical clinical reality [29]. Motivated by these opportunities, vaccine delivery has been the most widely investigated use of microneedles.

Skin pretreatment with microneedles has been employed to vaccinate with diphtheria toxoid with cholera toxin as adjuvant, which generated similar immune responses compared to subcutaneous injection, although this approach failed to generate significant immune response to influenza vaccine [46]. Using a related approach, the skin has been scraped with blunt-tipped microneedles to increase delivery of a DNA vaccine against hepatitis B, recombinant anthrax vaccine, and live attenuated Japanese encephalitis vaccine in animal models as well as rabies vaccine in human subjects [29]. These approaches were found to be less effective than intradermal injection mainly due to inefficient delivery into skin from the topical formulations.

To enable more controlled and efficient delivery of vaccines, coated microneedles have been the most extensively studied technique for vaccination with microneedles. Influenza vaccination with coated microneedles has been extensively studied in recent years, showing complete protection against lethal viral infection after vaccination using H1N1 and H3N2 seasonal strains in mice. Use of trehalose into the coating formulation as a stabilizer was shown to prevent antigenicity loss of the influenza vaccine [29]. Studies suggest enhanced memory responses after microneedle vaccination, using whole inactivated influenza virus as well as virus-like particle (VLP) vaccine and recombinant subunit vaccine, compared to intramuscular injection, to the extent of reduced levels of detectable virus titers in mouse lung after viral challenge and higher levels of IgG, improved induced cellular recall responses [41]. Site-selective coating of vaccine on the tip of microneedle resulted in improved dose-sparing and better delivery efficiency and managed to induce strong immune response against influenza in mice [47]. Influenza vaccination has also been carried out using dissolving microneedles made of PVP encapsulating lyophilized inactivated influenza vaccine. Use of lyophilized vaccine showed improved stability and enhanced protective immunity [29]. Human trial of intradermal influenza vaccination in healthy adults, using a needle array of four silicon microneedles measuring 450 μm in length and using 3-6 μg of influenza vaccine, induced similar immune responses compared to intramuscular injection of 15 μg of vaccine [29].

Bacillus Calmette–Guérin (BCG) vaccine has been administered in guinea pigs using coated microneedles, which resulted in improved immunity compared to intradermal injection [48]. A DNA vaccine encoding hepatitis C virus protein was coated on microneedles and induced an effective cytotoxic T lymphocyte response in mice [49] [29]. Metal microneedles coated with hepatitis B surface antigen, using poly[di(carboxylatophenoxy)phosphazene] as both a

coating excipient and as an immuno-adjuvant, induced superior antigen-specific IgG in pigs. [29].

Microneedles, used for intradermal vaccination with anthrax recombinant protective antigen, have shown complete protection of immunized rabbits against lethal challenge with anthrax spores as well as 50-fold dose sparing compared to the intramuscular route [29].

2.6. Fabrication of microneedles

Low-cost microneedle arrays were envisioned for drug delivery in 1970's. Although, it is only after the advancement in microfabrication technologies in 1990's, researchers focused on the production of microneedles suitable for pharmaceutical applications, such as, vaccine delivery [29].

In this section, numerous successful fabrication methodologies of microneedles of different types, viz. solid, hollow, coated and dissolving, are illustrated. As shown schematically in Figure 2.4, each of these microneedle designs enables vaccine delivery by different mechanisms [29].

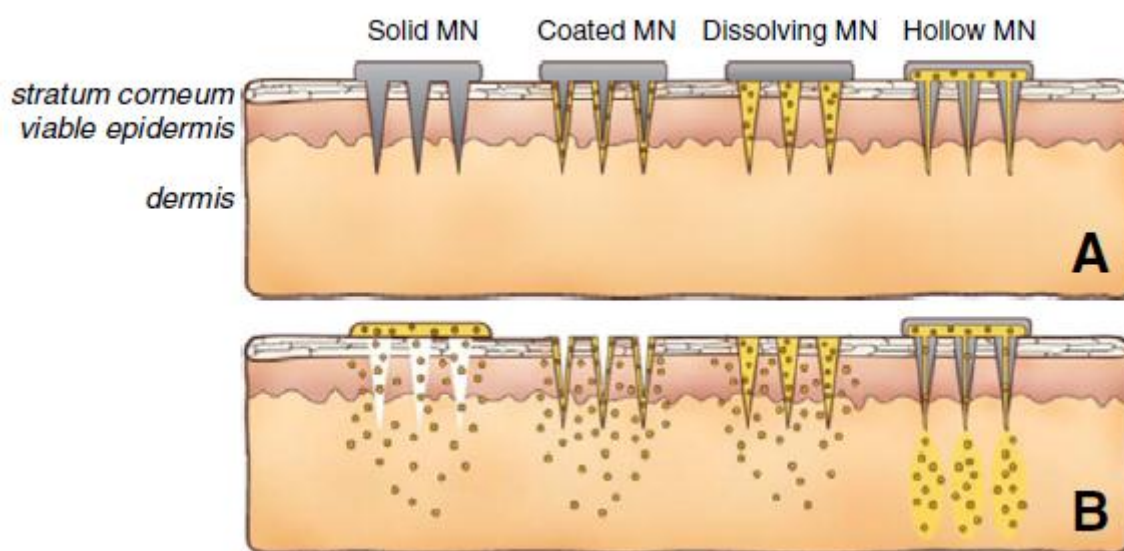


Figure 2.4: Methods of drug delivery to the skin using microneedles (MN). Microneedles are first applied to the skin (A) and then used for drug delivery (B) [29].

2.6.1. Solid microneedles

Solid microneedles can be especially beneficial for pretreatment of skin for pore formation before delivery of liquid form of vaccines from a transdermal patch. Sharp microneedles penetrate into or scrape the skin in order to make holes through which drugs can transport, either for local effect in the skin or for systemic delivery after uptake by skin capillaries. The fabrication of solid microneedles has focused on providing sufficient mechanical strength through choice of microneedle material and geometry and reducing the force needed to insert microneedles into tissue by increasing tip sharpness [29]. Solid microneedles, suitable for vaccine transdermal delivery of vaccines, have been fabricated out of various materials using different methodologies, and in this section few of them will be reviewed.

2.6.1.1.Coated microneedles

2.6.1.1.1. Sharp-tip Chitosan-coated Silicon microneedles using RIE and Bosch Process

Microneedles were fabricated using a series of photolithography, thin-film deposition, and reactive ion etching techniques using single-crystal Si as starting material [35].

After deposition and patterning of square or circular oxide patterns (50 to 100 μm in diameter) on a Si substrate, the portion of the Si wafers not covered by these patterns was etched away by an isotropic-reactive ion etching (RIE) process using SF_6/O_2 plasma. When a proper tip pattern was formed, the needle body was then formed using the anisotropic Bosch process. Needle diameter was controlled by mask layout, and needle height was determined by etch time and HNA (a combination of nitric, fluoric, and acetic acids) wet etch. The height of the microneedles fabricated in this method was 130 μm , with a base diameter of 80 μm and needle-to-needle spacing of 200 μm (Figure 2.5). The microneedles were uniform in size with very sharp tips (i.e., radius of curvature $<1\ \mu\text{m}$) [35].

A thin silicon nitride film of less than 100 nm was deposited to ensure biocompatibility. Pure chitosan plus 1% acetic solution containing calcein or BSA (bovine serum albumin), as model drug, was used to prepare thin film on the microneedles using casting method [35].

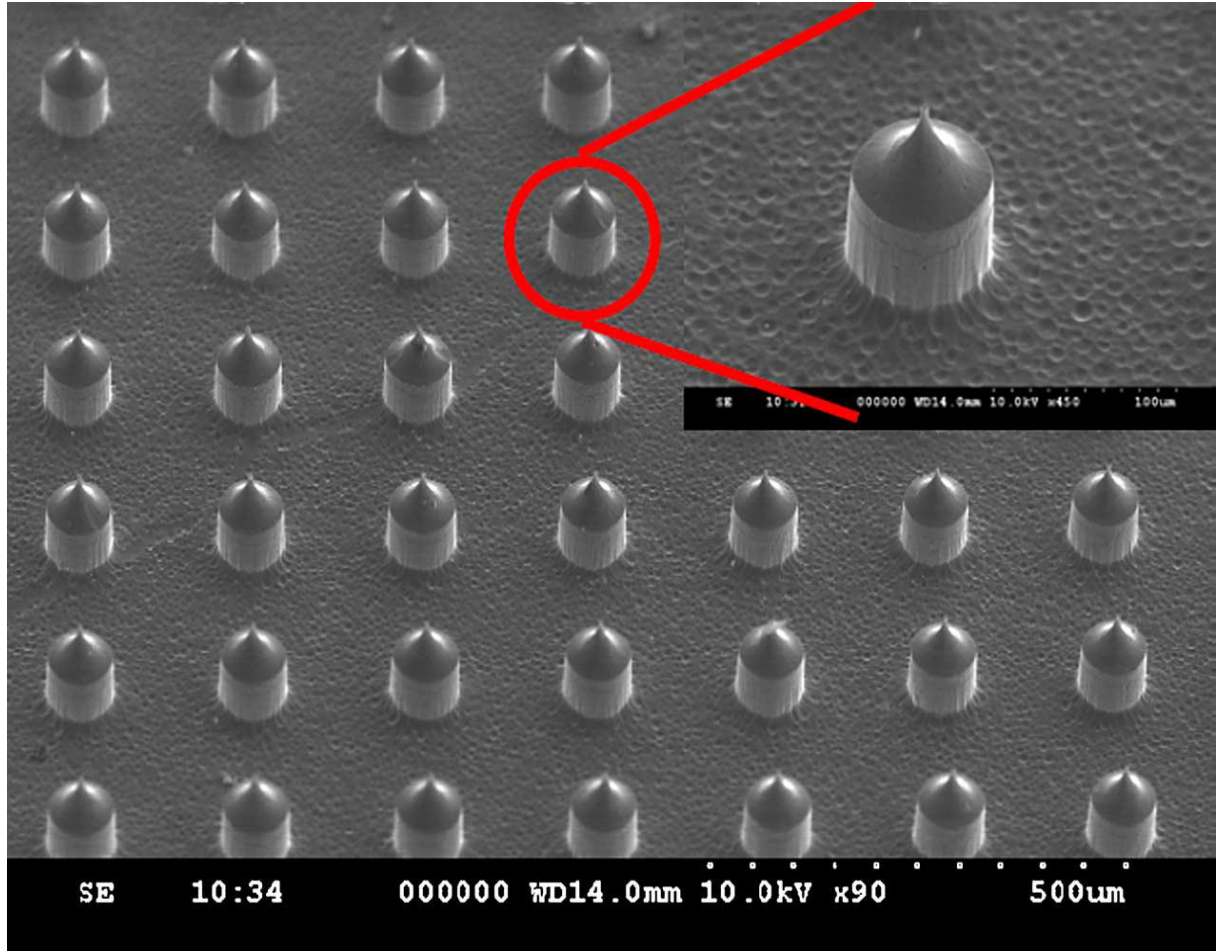


Figure 2.5: Scanning electron micrograph shows stereoscopic view of a section of 20x20 microneedle array with 130- μm height, 80- μm base diameter, and 200- μm spacing [35].

2.6.1.1.2. *Grooves-embedded microneedle arrays of bio-compatible polymer using hot embossing process*

An efficient microneedle should have a sharp 3D tip to reduce insertion force and a large base to increase the fracture force [50]. In this section the fabrication of grooves-embedded microneedle with sharp 3D tip and large base is illustrated (Figure 2.6 (a)). In general, the microneedles which had a pointed sharp tip had a cone or a pyramid shape, and the microneedles which had a complicated side shape had a flat top. Microneedle with pointed sharp tip to reduce insertion force can be fabricated with inclined ultraviolet (UV) lithography and a hot embossing process, as illustrated in Figure 2.6 (b).

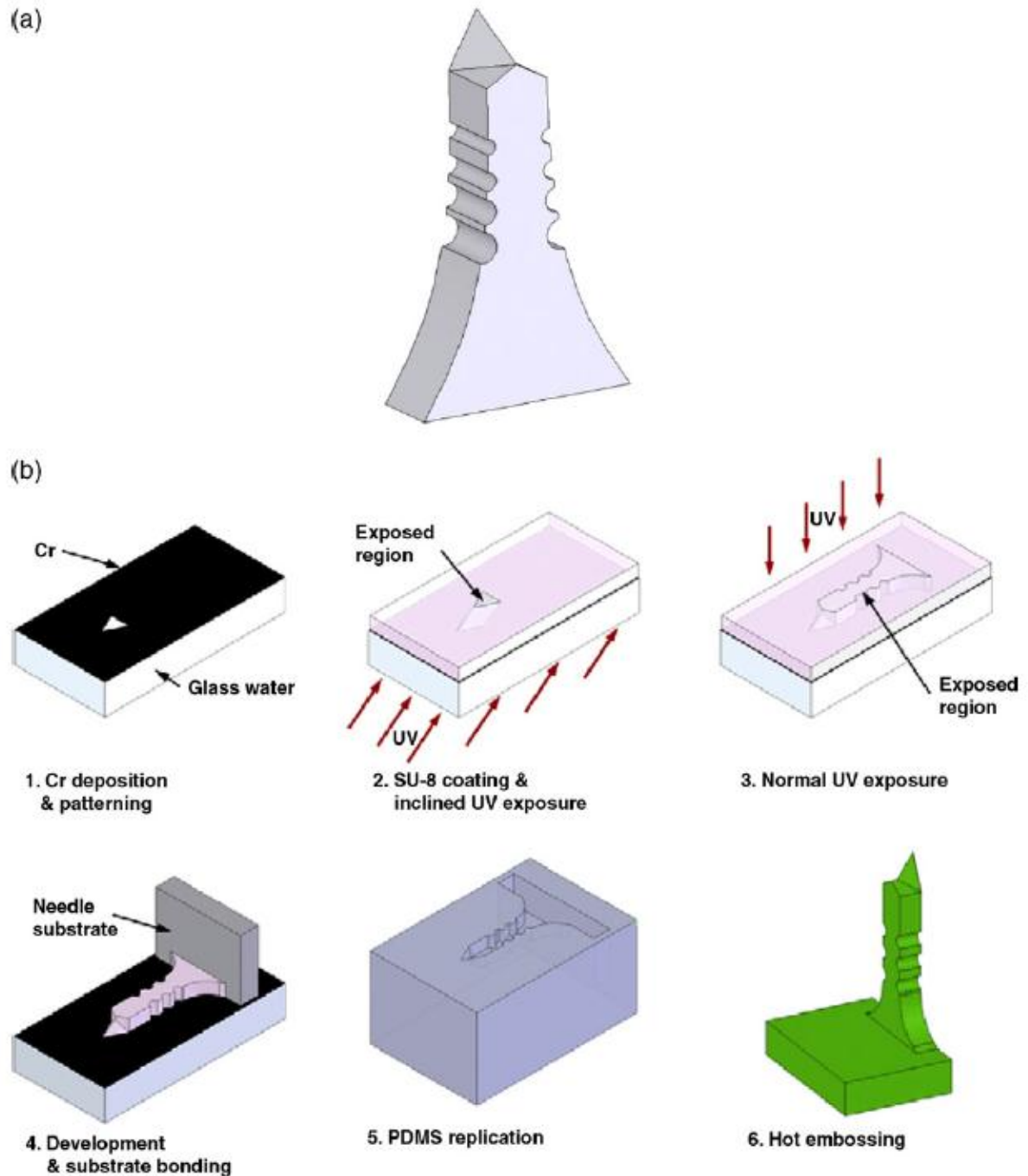


Figure 2.6: Design and fabrication of grooves-embedded microneedles: (a) design, (b) fabrication process [50].

The fabrication process starts with 150-nm-thick chromium (Cr) deposition onto a Pyrex glass wafer (Corning). After the Cr layer is patterned to define the tip of the microneedle, the negative thick photoresist SU-8 is coated on the wafer. Inclined UV is applied from the backside of the wafer to define the sharp 3D tip and normal UV is applied from the front side of the wafer to define the grooves-embedded side shape [50]. After development of the SU-8, grooves-embedded microneedles of SU-8 appear on the wafer. The master mold of the grooves-embedded microneedle array is completed by attaching a piece of silicon wafer as a

substrate of the microneedle array. A negative mold for the hot embossing process is fabricated by replicating the master mold using a poly dimethylsiloxane (PDMS) replication technique. A grooves-embedded microneedle array of poly-l-lactic acid (PLLA) is fabricated by replicating the negative mold using the hot embossing process. The mold and PLLA grains are heated to 190°C and pressed with a pressure of 20 kg/cm² for 10min. After the mold is cooled to room temperature, the grooves-embedded microneedle array is de-molded [50]. Figure 2.7 shows the fabrication results.

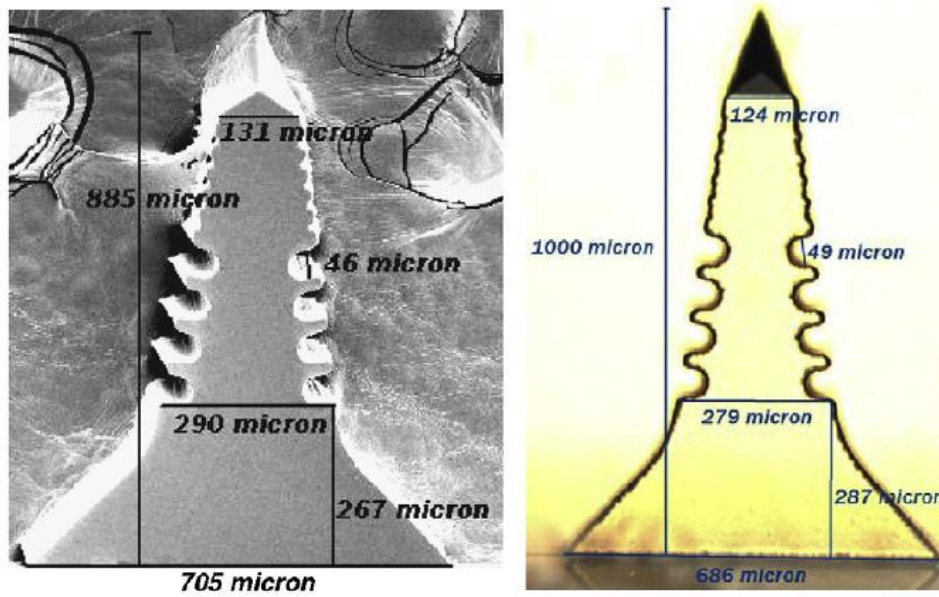


Figure 2.7: SEM images of (a) PLLA microneedle with its dimensions and (b) dimensions of the master mold [50].

The fabricated PLLA microneedles have sharp 3D tips, smooth or grooves-embedded shafts, and large bases. The height, base width, and thickness are 880 ± 20 , 710 ± 15 , and 145 ± 15 μm , respectively (Figure 2.7 (a)). Although the dimensions of the master molds (Figure 2.7 (b)) were similar to those of the mask design, they were dissimilar to those of the PLLA microneedles. The PLLA microneedles are wider but shorter than the master mold; this happened because pressured PLLA pushed PDMS molds in the hot embossing process. If a pressed polymer resin pushes a soft mold, the cavity in the mold expands, and thus, the molded structure has increased dimensions. However, the heights of PLLA microneedles were decreased in this study. The reason for the decreased heights; the pressed PLLA in the cavity for a substrate of a microneedle array pushed the microneedle-engraved part of the PDMS mold.

The grooves-embedded microneedle array was found to be capable of delivering higher antigen load, by providing increased surface area, than array of smooth microneedles having similar dimensions [50].

2.6.1.1.3. Silicon microneedles array with Biodegradable tips using RIE and Anodization

One of the main challenges faced by Silicon microneedles is their vulnerability to shear forces while penetration of skin resulting in bending and buckling and, in turn, breakage of the microneedle tips inside human body. This increases the possibility of infection as silicon is neither bio-degradable nor bio-compatible [51]. To address this shortcoming of silicon microneedles a novel fabrication method is illustrated in this section to fabricate microneedles having biodegradable tips of porous silicon material. Porous silicon is nano-structured silicon and is good for biological applications because of its bioactive and biodegradable properties [51]. These porous tips may break off after the drug delivery process and be allowed to remain in the skin, as it can be easily biodegraded within 2 to 3 weeks. The macroporous tips were fabricated using a classical anodization or electrochemical etching process in MeCN/HF/H₂O solution.

Microneedles must be at least 50 μm in length, but not more than 150 μm , in order to penetrate the stratum corneum without reaching the nerves in the dermis layer. High aspect ratio silicon microneedles (Figure 2.8) were fabricated using optimized SF₆/O₂ RIE process. The isotropic profile of the microneedles was fabricated using two effects: flowing of thick photo-resist mask at 120 °C and notching effect (Figure 2.9) of the reflected charges on mask.

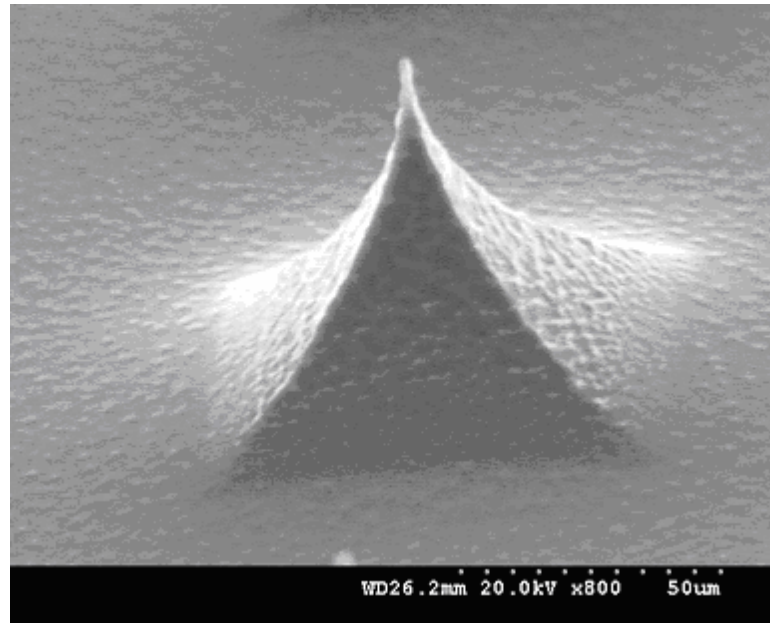


Figure 2.8: SEM picture of the fabricated microneedle [51].

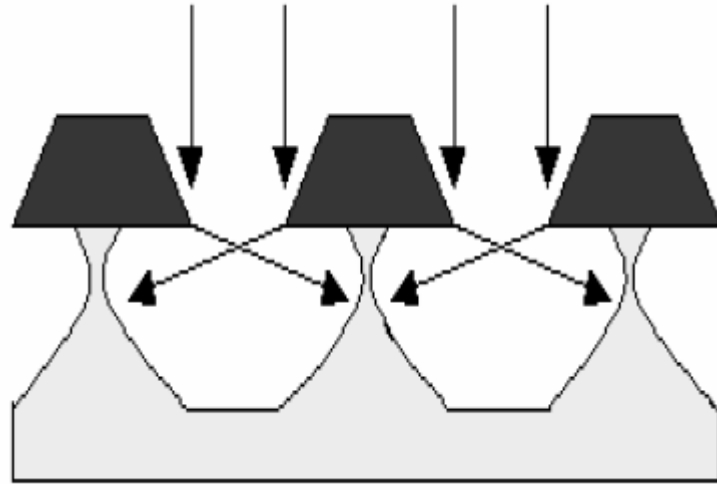


Figure 2.9: Notching effect of reflected charges on the mask where ions and radicals with high energy are reflected by the oblique profile of the photoresist and generate an increased etching under the mask [51].

The main steps of the fabrication process of the microneedles are presented in Figure 2.10 [51]. A 4" silicon wafer with <100> crystal-

lographic orientation, n type 1-10 ohm-cm was initially cleaned in piranha solution (H_2SO_4 : H_2O_2 2:1) at 120°C for 20 minutes and then rinsed in DI water and spun dried (Figure 2.10a). On the silicon wafer a 0.5 μm -thick SiO_2 was deposited at 300°C, from SiH_4 and N_2O , at a pressure of 700 mTorr and a power of 300W using PECVD (Figure 2.10b). A photoresist mask using AZ9260 positive photoresist, with a thickness of 8 μm , was used for the patterning of the SiO_2 layer (Figure 2.10c). The pattern is transferred to the SiO_2 layer using RIE with CHF_3 and He gases (Figure 2.10d). After the patterning of the oxide layer, the tips were generated using an isotropic RIE process (Figure 2.10e and 2.10f) with SF_6/O_2 in an ICP DRIE system. The process was optimized for a better control undercut, and with a depth to-width aspect ratio of 3:1 [51].

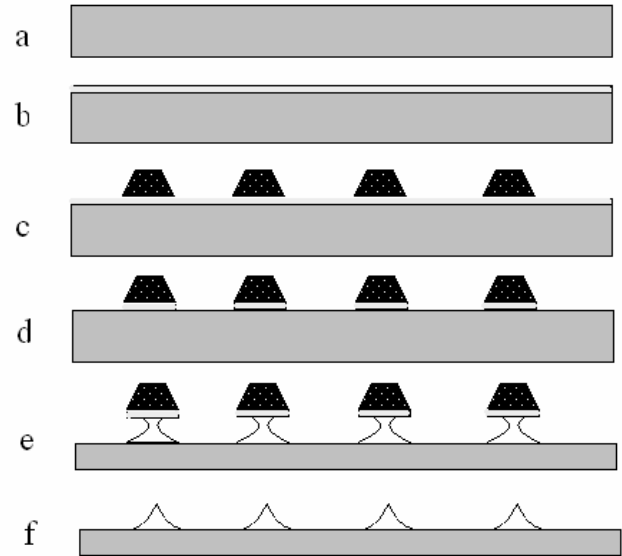


Figure 2.10: Fabrication process: a) silicon wafer, b) PECVD SiO_2 , c) Photoresist mask d) etching of SiO_2 , e) plasma etching in SF_6 , f) sharp-tip microneedles [51].

After the fabrication of the silicon microneedles array, an anodization process was used for the conversion of a single crystal silicon material of the tip into a porous structure. The main steps of the porous tips fabrication are shown in Figure 2.11 [51] [52].

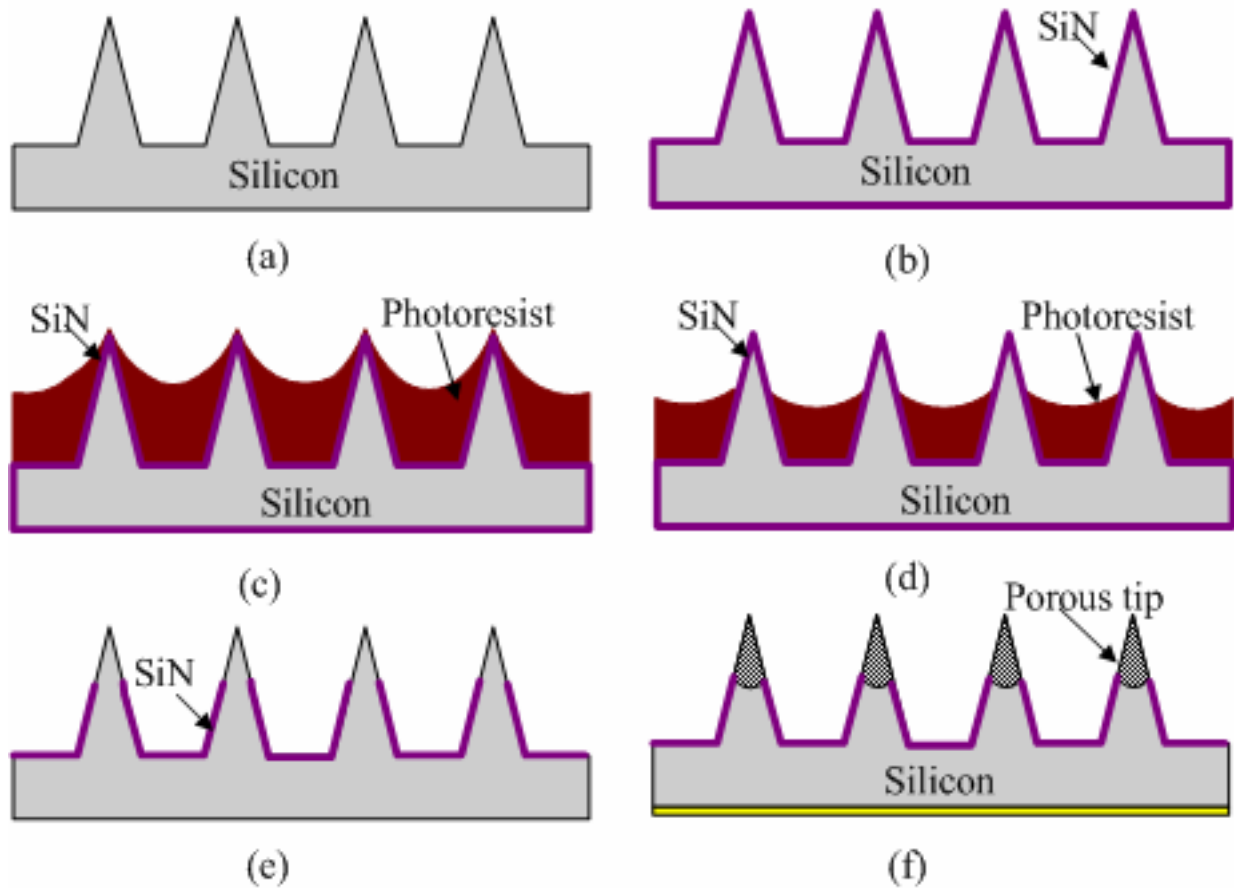


Figure 2.11: Fabrication process flow for the porous tips: (a) LPCVD Si_3N_4 deposition, (b) photoresist coating, (c) photoresist reflowing and O_2 plasma, (d) Si_3N_4 etching in RIE and photoresist removal, (e) Al deposition (back of the wafer), (f) anodization [51].

After cleaning, a 500 nm Si_3N_4 passivation layer was deposited on the microneedles surface in LPCVD furnace at 725 °C (Figure 2.11a). A thick layer of photoresist AZ9260 was spun twice on the surface of the microneedles, followed by baking at 120°C for 15 min (Figure 2.11b). Due to the flowing effect, the photoresist covering the tips of the needles was much thinner than those at the body and at the bottom. Thus the photoresist on the tips of the microneedles was removed with an O_2 plasma etching process using RIE (Figure 2.11c). Thus the top part of the needle became free of photoresist and the Si_3N_4 layer on the microneedle tips could be removed with a RIE process using CHF_3/He chemistry (Figure 2.11d). The Si_3N_4 layer, from the backside of the wafer, was also removed using a similar RIE process. On the back of the wafer, an aluminum layer was sputtered in order to achieve a good electric contact for next electrochemical process (Figure 2.11e). Then the porous silicon was generated only on the tip of the microneedle using a classical anodization process, while as the needle body was protected by the remaining Si_3N_4 layer (Figure 2.11f).

Figure 2.12a shows the experimental setup of the anodic electrochemical etching process [51]. The Pt electrode was used as the cathode and silicon wafer as anode. ADC power of 36~72V was used as the source. The used electrolyte was a mixture of acetonitrile (MeCN) and diluted hydrofluoric acid (HF). The mixture has two compounds of MeCN: HF (4M):H₂O = 92%:4%:4% by weight. The electrochemical anodization process was carried out at a current intensity of 10 mA cm⁻² for 30 minutes.

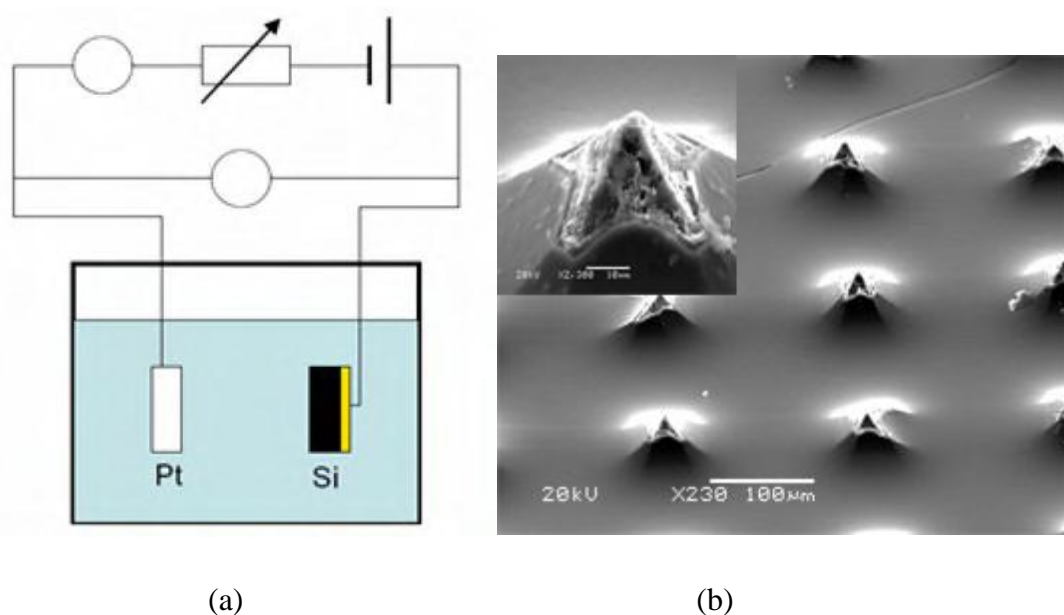


Figure 2.12: (a) Schematic view of the electrochemical anodization process [51], (b) SEM image of the porous silicon tip [52].

Figure 2.12b shows a SEM picture of the porous silicon tip after the completion of the anodization process. These microneedles were shown to enhance the drug release rate by five times compared to conventional transdermal drug delivery methods without enhancers [51].

2.6.1.2. Dissolving microneedles

2.6.1.2.1. Multilayered, Densely-Packed Dissolving Microprojection Arrays using DRIE and polymer casting

In this section, a new approach of very small and densely packed (20000 projections cm⁻²) microprojections (henceforth referred as Nanopatch [NP]) (Figure 2.13a) was conceived for direct and precise delivery of vaccine to immunocompetent cells of skin [53] [54]. These NPs are fabricated from the active/excipient material, which dissolve upon application to the skin. Such dissolving microneedles have the promise of 1) greater payload delivery, 2) increased control over release, and 3) the reduced risk of irritation because projections comprise bio-compatible and biodegradable materials. These NPs are suitable for robust penetration and

substrata skin targeting and meet the other practical needs of a viable vaccine delivery platform, including (i) maintaining vaccine viability during formulation (e.g., avoiding high temperatures and/or an adverse pH), (ii) enhanced thermostabilization of antigen molecules obtained by dry-coating method [55] and (iii) achieving the release of vaccine in skin within minutes of application (ideally dissolving within 5 min, post administration). These multi-layered NPs facilitate the delivery of multiple payloads within the one array, and overcome excess payload on the surface of the skin by eliminating the variations in payload yield due to encapsulation efficiency and non-uniform layering. These NPs successfully delivered two vaccines (ovalbumin protein as a model antigen, and in separate experiments, Fluvax2008, a commercial influenza vaccine) resulting in more efficient antibody generation than standard needle and syringe delivery [53].

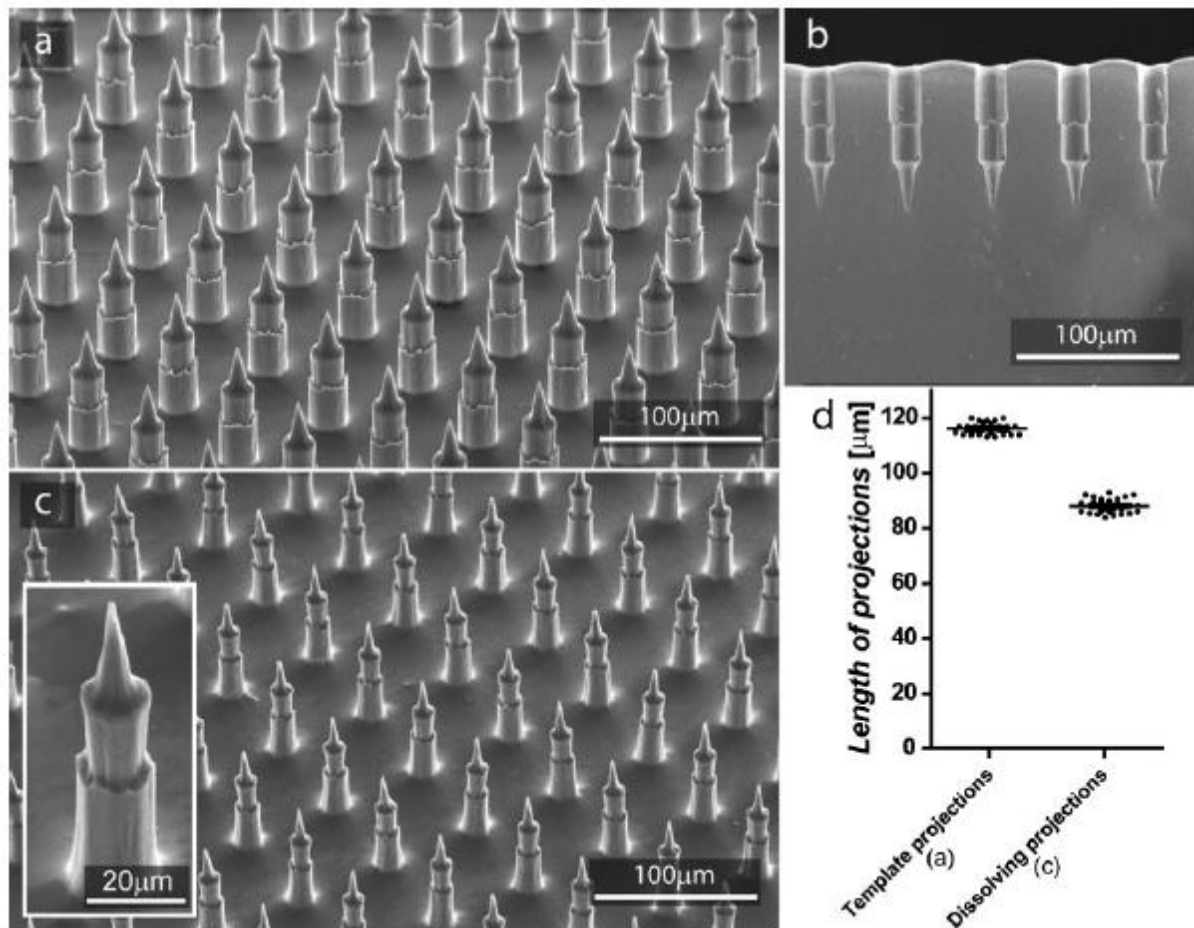


Figure 2.13: Scanning electron microscopy (SEM) images showing a) gold-coated silicon Nanopatch(NP) array template; b) cross-sectioned polydimethylsiloxane (PDMS) mold; c) corresponding dissolving Nanopatch(dNP) array comprising carboxymethylcellulose (CMC) with insert showing magnified image of a single projection; and d) graph showing the lengths of the template projections (a) compared to the dissolving projections (c) [53].

The NPs were fabricated from silicon using a process of Deep Reactive Ion Etching (DRIE) according to a patent [56]. The NPs are solid silicon, sputter coated with a thin layer of gold (~100 nm in thickness) [54]. These NPs were later used as template for making polydimethylsiloxane (PDMS) mold for fabricating dissolving Nanopatches or dNPs. Each projection on the template consists of a total length of 116 ± 2 μm (mean \pm standard deviation) with a base diameter of 23 ± 1 μm (Figure 2.13a). ANP is 5×5 mm in size and the central 4×4 mm area contains 3364 densely packed microprojections. The diameter of the microprojections at their base is 25–30 μm . The distance between the centers of adjacent microprojections is 70 μm . A size reduction of approximately 6% was observed between the projection dimensions of the silicon template and PDMS mold (Figure 2.13b) [53].

Carboxymethylcellulose (CMC) was then used for casting the PDMS mold to fabricate biodegradable dissolving Nanopatches (dNPs) (Figure 2.13c) mirroring the silicon NP template. During the casting process, the payload solution was added to the surface of the mold and centrifuged so that it flowed into the holes of the mold. The surface of the PDMS is highly hydrophobic, resulting in excess solution ‘rolling’ off the mold during the casting process. To evenly disperse the payload solution across the surface of the mold, an absorbent dispersion membrane was placed on the surface prior to casting [53]. The dNP projections were 88 ± 3 μm in length and a base diameter was 17 ± 1 μm corresponding to a $32 \pm 5\%$ reduction in size from the NP template (Figure 2.13d). The decrease in dimensions is attributed to the loss of moisture during the casting process, leading to contraction and solidification of the solution.

Then the more complex multilayered dNPs incorporating multiple layers of different payload solutions were fabricated, in order to reduce the wastage of payload during administration and gain fine control over release properties within the skin layers. A schematic of the casting process is outlined in Figure 2.14a, showing the steps to form an n-layer dNP array with different payloads localized to specific length segments within the projections. First, step 2 shows the placement of a porous membrane on the surface of the mold prior to adding the payload solution. Then the payload solution is absorbed into the membrane, dispersing across the surface of the mold before casting (Figure 2.14a: step 3–4). A secondary solution is cast and dried to form a dNP array (Figure 2.14a: step 5–7). During the casting of the secondary layer, the previous layer is hydrated facilitating fusion between the two different layers. This

can be repeated for n layers, resulting in the formation of solid projections during the drying process and a single solid structure upon removal from the mold [53].

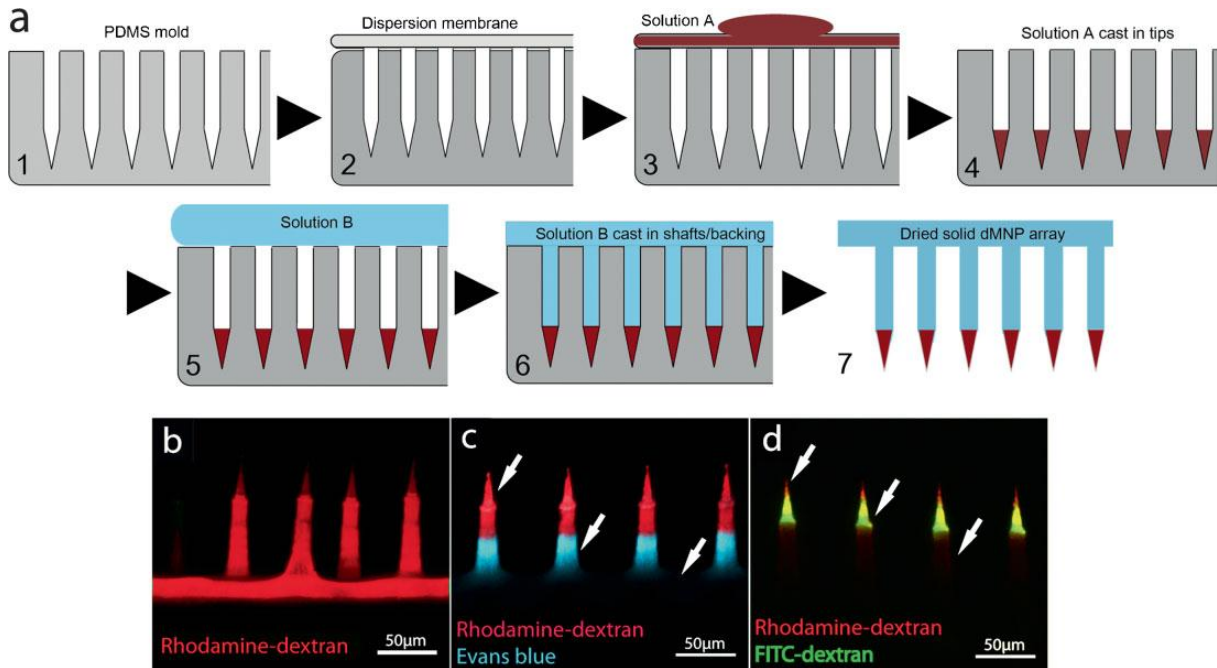


Figure 2.14: Schematic of the fabrication process and dNPs fabricated using this process. a) Schematic diagram of an example casting process to produce an ‘n’-layered dNP array with payload in the tips; b) dNP array consisting of rhodamine-dextran; c) layered dNP array consisting of rhodamine-dextran, Evans blue, and CMC backing (arrows indicating specified layer); and d) layered dNP array consisting of rhodamine-dextran, FITC-dextran and CMC backing (arrows indicating specified layer) [53].

Distribution of multiple fluorescent payloads on dNPs was investigated via fluorescence microscopy (Figure 2.14b–d). A uniform formulation throughout the dNP projections and backing using a rhodamine-dextran payload was used first (Figure 2.14b). The dimensions of these projections were $92 \pm 5 \mu\text{m}$ in length with a $23 \pm 1.1 \mu\text{m}$ in base diameter. Dual layered dNPs (Figure 2.14c) with discrete layers of two payloads, i.e., rhodamine-dextran, localized to the projection tips ($56 \pm 2 \mu\text{m}$ measured from the tip) and Evans blue (measuring $33 \pm 1 \mu\text{m}$ from the rhodamine-dextran/Evans blue boundary towards the base) were fabricated. The third layer (dNP backing) contained CMC without fluorescent payload constituting the base of the array. This dNP array was replicated, and comparison between the arrays resulted in a difference of up to $10 \mu\text{m}$ in length of the rhodamine-dextran layer and up to $3 \mu\text{m}$ in length of the Evans blue layer. A four-layer dNP array (Figure 2.14b) was fabricated, in similar way, with rhodamine-dextran localized to the projection tips ($19 \pm 2 \mu\text{m}$ measured from the tip) while a secondary layer of fluorescein isothiocyanate (FITC)-dextran presented a discrete layer measuring $22 \pm 2 \mu\text{m}$ from the rhodamine-dextran/FITC-dextran boundary towards the base. A third layer containing a mixture of rhodamine-dextran and CMC in the shafts ($54 \pm 1 \mu\text{m}$) was fol-

lowed by a backing layer of CMC without fluorescent payload constituting the base of the array [53].

It was found that greater than 50% of the length of the microprojections was dissolved and diffused within the layers of the skin (Figure 2.15d–f) only two minutes after successful penetration of skin (Figure 2.15a–c) [53].

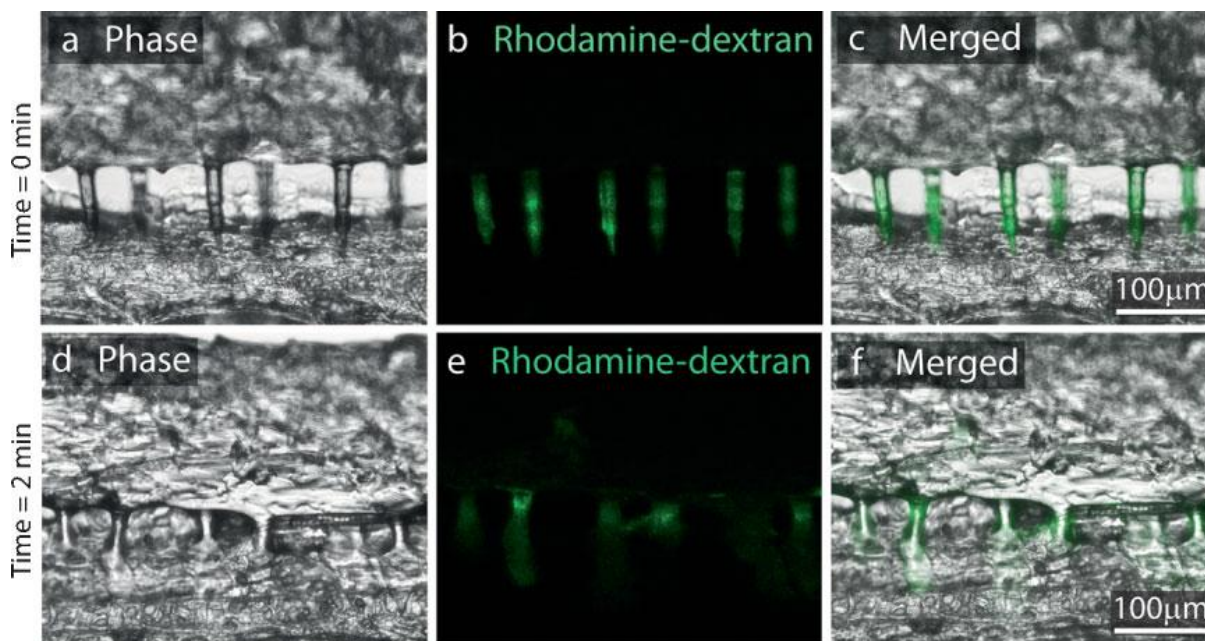


Figure 2.15: Fluorescent microscopy images showing rhodamine-dextran dNPs penetrating and dissolving in mouse ear skin at a–c) time=0 and d–f) time=2 min: image phase (a, d), fluorescence only (b, e), and merged phase and fluorescence (c, f) [53].

Such reduction in dissolution time can be attributed to the significant increase in surface area achieved by thousands of microprojections. In the context of vaccine delivery, 5 min delivery time using such dNPs is highly relevant. Vaccinations should be quick, preferably not much longer than current needle/syringe administration; therefore the relatively fast dissolution rate is an important platform characteristic in vaccine delivery.

2.6.1.2.2. *Sharp-tip Tapered-cone Dissolving Microneedles made of Hyaluronic acid*

In this section, fabrication of sharp tip tapered-cone dissolving microneedles made of hyaluronic acid (HA), using micromolding technique is illustrated. Hyaluronic acid is a common ingredient in care skin products, highly biocompatible and offers enough resistance to deformation. These microneedles were fabricated without the using any heating step and organic solvent, which is a notable advantage in preserving the stability of incorporated drugs or vaccine. Sharp tips of these microneedles are short enough to reduce damage to skin nerves and

pain, and narrow enough to induce minimal trauma and reduce the opportunities for infections to develop during insertion [43]. This method combines the efficacy of conventional injection needles with the convenience of transdermal patches, while minimizing the disadvantages of these administration methods.

Microneedles (MNs) were fabricated via micromolding technologies, with HA as the base material, and then, were loaded with 0.13, 0.25, and 0.44 IU of bovine insulin. The fabrication process of MNs can be considered as transcription from the micromold with needle-shape in place. In detail, 15% HA solution was obtained by mixing well with distilled water. Insulin solution dissolved in 0.1M HCl solution was added to the 15% HA solution and mixed well to prepare HA solution containing insulin. 0.3 ml of the resulting HA solution containing insulin was placed on a 2 cm×2 cm micromold at room temperature. After 2 h drying in desiccator, the remaining solution was removed on the surface of mold with cotton, then 0.1 ml of 20% HA solution was placed on the same place of micromold. After drying the micromold completely, a 2 cm×2 cm polyethylene terephthalate (PET) adhesive tape was attached on the baseplate for reinforcing. A sheet of insulin-loaded MNs was obtained by peeling the mold off. Insulin-loaded MNs in circular area with a diameter of 10mm were obtained by cutting the sheet with a punch. The thickness of the MNs base plate was $50\pm5\text{ }\mu\text{m}$. According to the fabrication process, the baseplate was considered to consist of HA and a small amount of insulin. The amount of insulin was determined in needles and baseplate, and more than 90% of insulin was detected in the needles. By cutting circular area of insulin loaded MNs from resulting sheet with a punch as shown in the process above, there was no sidewall formation in the resulting insulin loaded microneedles [43].

The resulting tapered-cone MNs were uniform in size with sharp tips. Each needle was approximately 800 μm in height, with a diameter of 160 μm at the base and 40 μm at the tip, and an interspacing of 600 μm between the rows of needles (Figure 2.16). There were approximately 190 needles in a circular area with a diameter of 10 mm. The failure force of our MNs was 17.5 N/cm^2 [43].

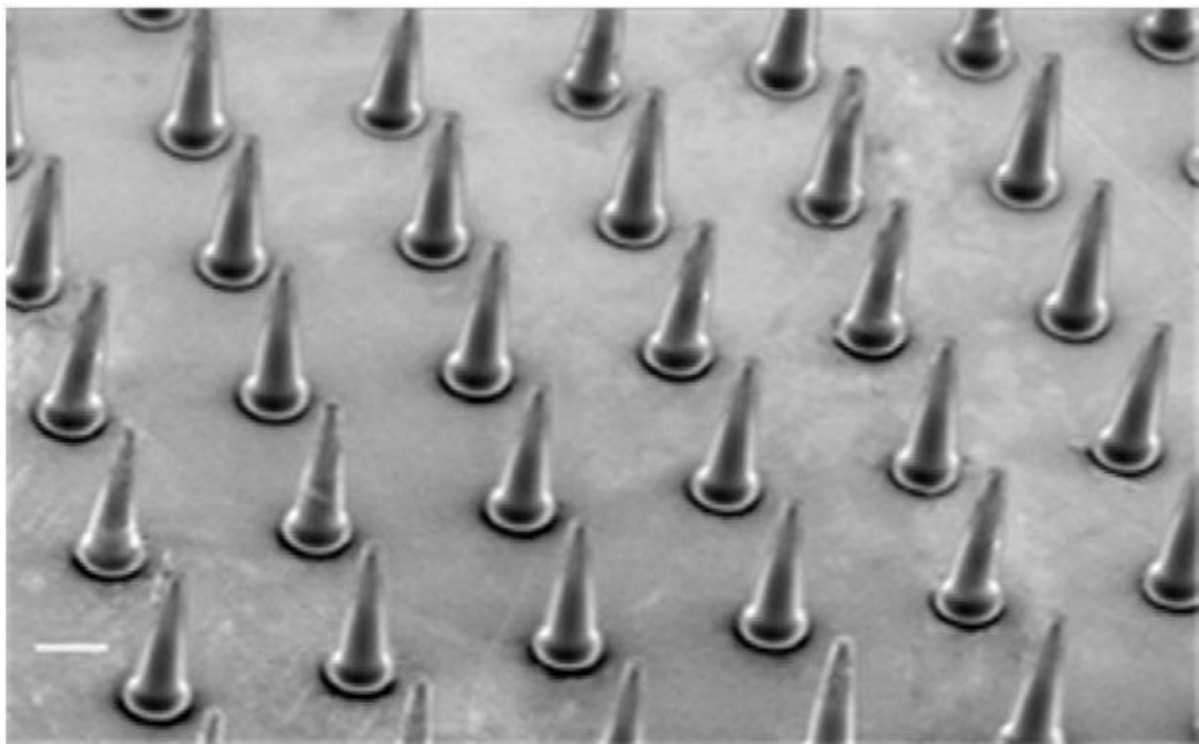


Figure 2.16: SEM image of a section containing insulin-loaded microneedle arrays (MNs) with lengths of 800 μm , and diameters of 160 μm at the base and 40 μm at the tip. Bar = 200 μm [43].

MNs were found to maintain their skin piercing abilities for at least 1 h, even at a relative humidity of 75% indicating suitable hygroscopy. After storing insulin-loaded MNs for a month at -40 , 4, 20, and 40 $^{\circ}\text{C}$, more than 90% of insulin remained in MNs at all temperatures, indicating that insulin is highly stable in MNs at these storage conditions. It was also shown that the skin damage incurred by the insertion of these microneedles was recovered within 24 hours. All the microneedles were completely dissolved within 1 hour of drug delivery, indicating efficient dissolution properties of such needles [43].

2.6.1.2.3. *Biodegradable Polymeric Microneedles, having High Aspect-ratio, based on Micromolding*

This study addresses microneedles made of biocompatible and biodegradable polymers, which are expected to improve safety and manufacturability. To make biodegradable polymer microneedles with sharp tips, optimized masking and etching techniques were adapted to produce beveled- and chisel-tip microneedles and a new fabrication method was developed to produce tapered-cone microneedles using an in situ lens-based lithographic approach [44]. To replicate microfabricated master structures, PDMS micromolds were generated and a novel

vacuum based method was developed to fill the molds with polylactic acid (PLA), polyglycolic acid (PGA), and their co-polymers PLGA. These polymers are highly biocompatible, biodegradable, inexpensive and mechanically strong.

a) Fabrication of Beveled-tip master structures

Microneedles with beveled tips were fabricated by first creating a master structure from SU-8 epoxy using ultraviolet (UV) lithography (Figure 2.17). A 300–350 μm thick layer of SU-8 epoxy with photoinitiator (SU-8 100) was coated onto a silicon wafer and lithographically patterned into 100 μm diameter cylinders, which defined the shape of the desired needles. A different mask was also used to create cylinders with a notch of 30- μm radius cut out of one side. These cylinders were arranged in an array, where the center-to-center spacing between cylinders in each row was 1400 μm and between each column was 400 μm . The 20x6 array had a total area of 9x9 mm^2 . PLGA 85/15 was used to fill the space between cylinders and the entire surface was coated with a 600-nm thick layer of copper by electron beam deposition. This copper layer was etched with acid ($\text{H}_2\text{SO}_4\text{:H}_2\text{O}_2\text{:H}_2\text{O}$ at a volumetric ratio of 1:1:10) to leave a pattern of rectangles with 0.6 mm width and 10 mm length that asymmetrically covered the tops of the epoxy cylinders and some of the sacrificial polymer (PLGA) on one side of each cylinder. Reactive ion etching (RIE) was used to partially remove the uncovered sacrificial layer and asymmetrically etch the tip of the adjacent epoxy cylinders. All remaining sacrificial polymer was removed by ethyl acetate, leaving an array of epoxy cylinders with asymmetrically beveled tips [44].

b) Fabrication of Chisel-tip master structures

Chisel-tip microneedles were fabricated using a combination of wet silicon etching and reactive ion etching of polymers (Figure 2.18). Silicon nitride was deposited onto a (100) silicon wafer to a thickness of 400 nm by chemical vapor deposition (PECVD) to make a hard mask to protect silicon against KOH etching. Next, the silicon nitride layer was lithographically patterned to expose a 15x 15 array of square dots each measuring 100 μm in width with 600- μm center-to-center spacing. From the exposed area silicon nitride layer was removed using RIE and the photoresist was then removed using acetone. KOH (30 wt. %), heated to 80 $^\circ\text{C}$, was then applied to the wafer to etch inverted pyramid-shaped holes. Etching occurred along the crystal plane to form 54.74 $^\circ$ -tapered walls terminating in a sharp point, which provide the chisel shape of the needle tips. To form the shape of the needle shaft, SU-8 epoxy photoresist

with photoinitiator was spin-coated onto the etched wafer to form a 500- μm thick film. A second mask was aligned with the wafer to expose the SU-8 coating to UV light in the same 15 x 15 array of square dots in vertical alignment with the silicon nitride pattern. After post-baking to crosslink the UV-exposed SU-8 on a hotplate for 30 min at 100 °C and then cooling, the non-crosslinked epoxy was developed with PGMEA (Propylene Glycol Methyl Ether Acetate) to leave behind obelisk-shaped SU-8 structures with their tips still embedded in the silicon wafer. To finally make master needle structures, the space between the obelisk structures was filled with PDMS (Sylgard 184). The crosslinked SU-8 was removed by reactive ion etching with oxygen plasma to leave a PDMS-silicon mold. Subsequently, polyurethane (Poly 15) was poured into the mold and crosslinked to form polymeric microneedles with chisel tips. Removal of these needles from the mold yielded the final master structure [44].

c) Fabrication of Tapered-cone master structures

Tapered-cone microneedles were fabricated using a novel lens-based technique (Figure 19). A 530 nm thick, opaque chromium (Cr) layer was sputter-deposited and lithographically patterned on a sodalime glass substrate to form a 20x10 array of circular dots each measuring 100 μm in diameter with 400 μm center-to-center spacing. Glass etchant (HF: HCl: H₂O at a volumetric ratio of 1:2: 17) was used to isotropically etch the glass substrate through the openings in the patterned chromium layer to create concave holes in the glass of 70 μm radius/depth. Casting of SU-8 photoresist with photoinitiator created a 1000- or 1500- μm thick film on the substrate with bumps that filled the concave holes. After soft-baking (100 °C, 12 h), the film was exposed from the bottom (through the glass substrate) to UV light. Due to the refractive index difference between the glass substrate and SU-8 resist, the bumps formed integrated microlenses. Light was blocked from passing through the areas between the microlenses due to the opaque chromium layer. Light shining through the lenses was focused within the SU-8 film to give latent images in the shape of tapered cones with a base diameter equal to the circular dot diameter of the chromium mask (i.e., 100 μm) and a length of, for example, 1000 μm , as determined by microlens geometry. Subsequent development of the unexposed SU-8 left a master structure of tapered cone microneedles [44].

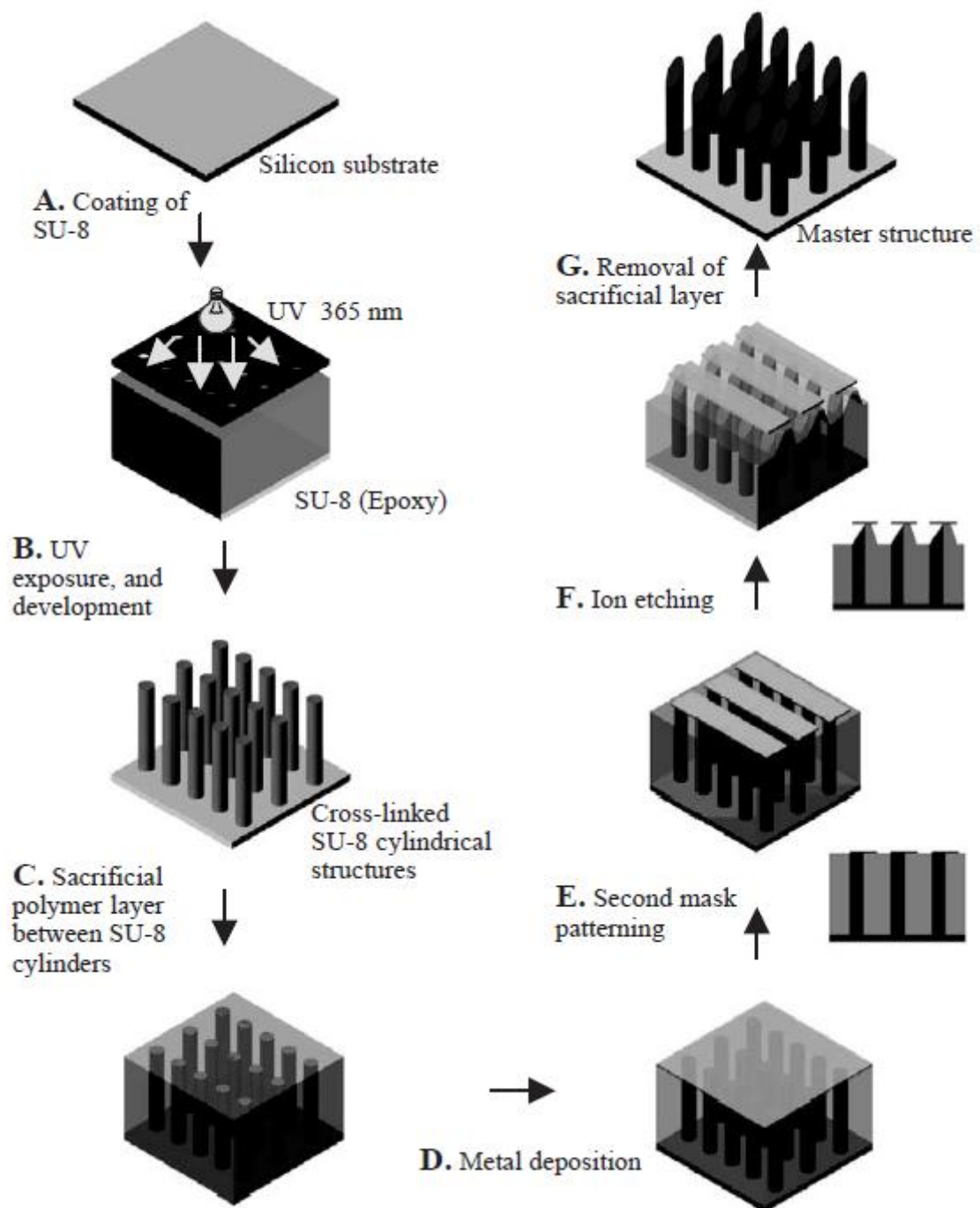


Figure 2.17: Schematic of process to fabricate beveled-tip microneedles. SU-8 photoresist is lithographically defined and developed to yield an array of cylinders. After filling the spaces between cylinders with a sacrificial polymer and lithographically placing a metal mask asymmetrically on top of each row of cylinders, the cylinders are ion etched to produce an array of microneedles with beveled tips to be used as a master structure for subsequent molding [44].

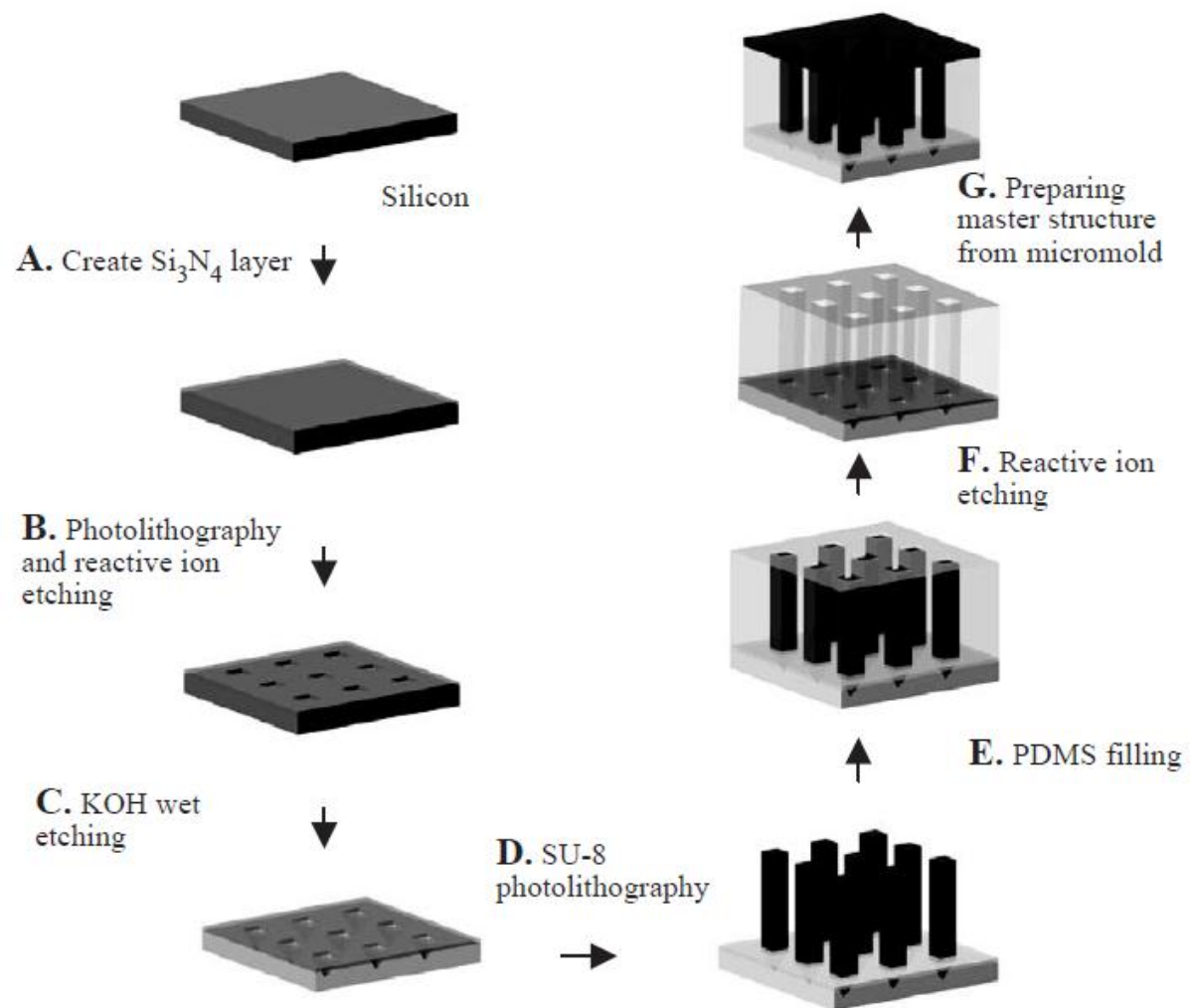


Figure 2.18: Schematic of process to fabricate chisel-tip microneedles. Using a lithographically defined Si_3N_4 mask, inverted pyramids are wet-etched into a $\langle 100 \rangle$ silicon substrate. SU-8 photoresist is lithographically patterned into each pyramid hole and as square columns on top. After surrounding the array of SU-8 structures with PDMS and removing SU-8 by reactive ion etching, the resulting mold is used to form an array of chisel-tip microneedles out of polyurethane to be used as a master structure for subsequent molding [44].

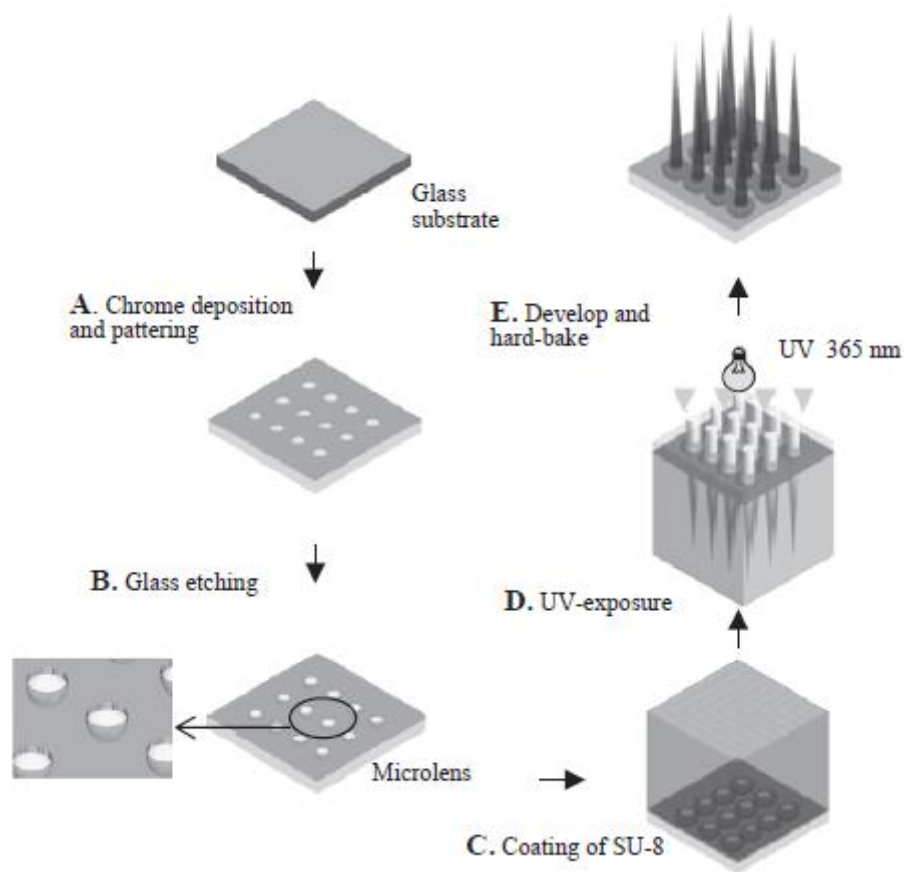


Figure 2.19: Schematic of integrated lens process to fabricate tapered-cone microneedles. Using a lithographically defined metal mask, a glass substrate is wet-etched to produce an array of hemispherical invaginations that form microlenses. After filling and covering these invaginations with a thick layer of SU-8 photoresist, UV light is shined through the glass substrate, forming latent images in the SU-8 layer that define the shape of an array of tapered-cone microneedles produced after development that are used as a master structure for subsequent molding [44].

d) Micromolding methods

To make molds for replication, these master structure arrays of SU-8 or polyurethane needles were coated with PDMS (10 mm thick; Sylgard 184) and allowed to cure for 12 h at 40 °C. After removing the master structures, the molds were covered with pellets of biocompatible polymer—polylactic acid (PLA, 1.1 dL/g), polyglycolic acid (PGA, 1.4–1.8 dL/g), or polylactic-co-glycolic acid (PLGA 50/ 50, 0.5 and 1.2 dL/g)—and placed in a vacuum oven under 70 kPa vacuum for 5 min at 140, 230 or 180 °C, respectively. Vacuum was applied to remove entrapped bubbles and help pull the polymer melt into the mold. The oven temperatures were selected to be just above the polymer melting points. The samples were then put into the freezer at 20 °C for 30 min before releasing the polymer needles from the PDMS mold by hand. The final polymer needles were stored in a desiccated container in the refrigerator for future use. The molds were also saved for re-use [44].

Figure 2.20 represents the microneedles formed by three different methods described above.

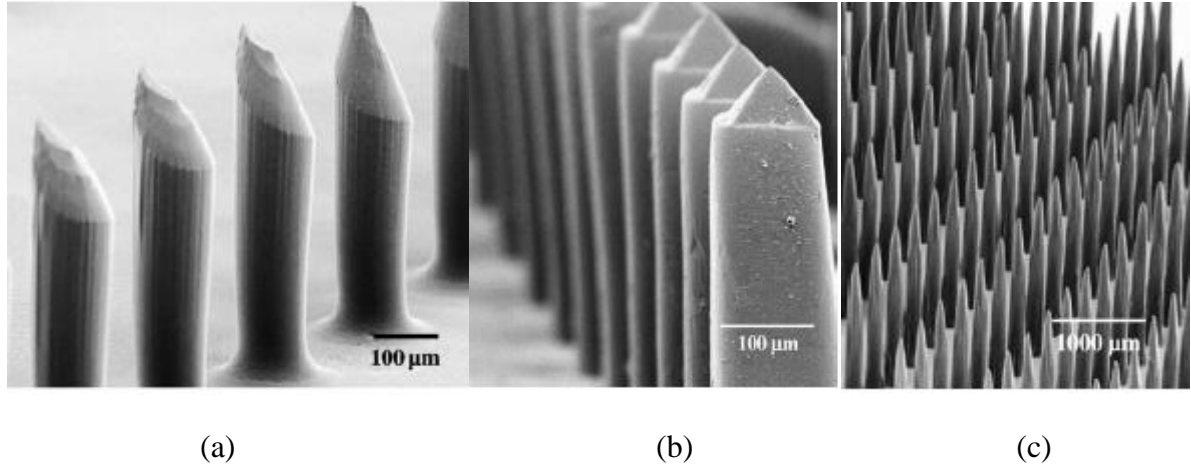


Figure 2.20: SEM images of (a) Beveled-tip PGA microneedles having shaft diameter 100 μm , tip diameter 10 μm , needle length 600 μm , (b) Chisel-tip PGA microneedles having square shaft width 100 μm , tip width 10 μm , needle length 570 μm , and (c) Tapered-cone PGA microneedles having base diameter 200 μm , tip diameter 20 μm , needle length 1500 μm [44].

2.6.2. Hollow microneedles

Hollow microneedles can play important role in biological fluid extraction and liquid drug or vaccine delivery.

2.6.2.1. Sharp-tip Cylindrical Silicon Microneedles with Side-openings using Bi-mask technique and DRIE

Microneedles with side openings are of particular importance, as standard tip microneedles are prone to having tissue clog their openings during skin penetration. The geometries of the needle tip have a great effect on the forces required for insertion and fracture. Insertion force can be shown to be independent of wall thickness; thin-walled hollow needles and solid needles with the same outer tip radii require the same insertion force [45]. Fracture force increases with increasing wall thickness and decreases with increasing wall angle, but is independent of tip radius [45]. Therefore, needles with a small tip radius and large wall thickness are considered the best option.

In this section fabrication of microneedles with an optimized design has been illustrated.

The microneedle array fabrication process flow is shown in Figure 2.21. First, an oxide layer is thermally grown onto a silicon wafer and patterned (Figure 2.21a). Holes are then anisotropically etched by RIE into the front side of the wafer (Figure 2.21b). These holes will be used as etch-stop markers for the next etching step. A thin film of SiO_2 is then deposited onto the backside of the wafer by using LPCVD. The SiO_2 is then patterned to form holes for both the microneedle channels and the etch-stop markers (Figure 2.21c). The channels are then anisotropically etched by DRIE from the backside of the wafer, as shown in Figure 2.21d. The etching continues until the special marker channels are exposed. The marker channels are etched along with the needle channels, but they etch through to a previous surface etch (on the order of $20\text{ }\mu\text{m}$ below the original wafer surface) on the front of the wafer. At this step, the depth of the needle channels, as blind holes, are the same as the depth of the anisotropic etch (Figure 2.21b). After the SiO_2 is removed (either by wet etching or RIE) the wafer is given another thermal growth of oxide. The next step is forming the bi-mask structure (Figure 2.21e), which is aligned to the center of the hole on the front side of the wafer. An anisotropic ICP-RIE step forms the body of the needle. Then, the wafer is given another thermal growth of oxide (Figure 2.21f), which forms a thin film of SiO_2 on the surface of both needle bodies and channels and is used to protect both the needle bodies and channels during the subsequent steps, thereby ensuring the needle thickness. After the upper mask from the bi-mask is removed by RIE, the wafer is isotropically etched using ICP-RIE (Figure 2.21g). Following that, a second anisotropic ICP is carried out. During this step, the side ports are formed (Figure 2.21h). In order to guarantee a sharp needle tip, a third isotropic ICP is employed (Figure 2.21i). Finally, the SiO_2 is etched (Figure 2.21j), and the processing is complete [45].

Figure 2.22 shows the SEM of the fabricated microneedle arrays. The needle array was $3 \times 3\text{ mm}$, containing 110 needles in a 10×11 configuration. The needles were $200\text{ }\mu\text{m}$ long with an internal diameter of $40\text{ }\mu\text{m}$ and three side openings of $28 \times 50\text{ }\mu\text{m}^2$ each. The tip of the needle was extremely sharp, having submicron dimensions of approximately 450 nm , as is clearly shown in Figure 2.22a [45].

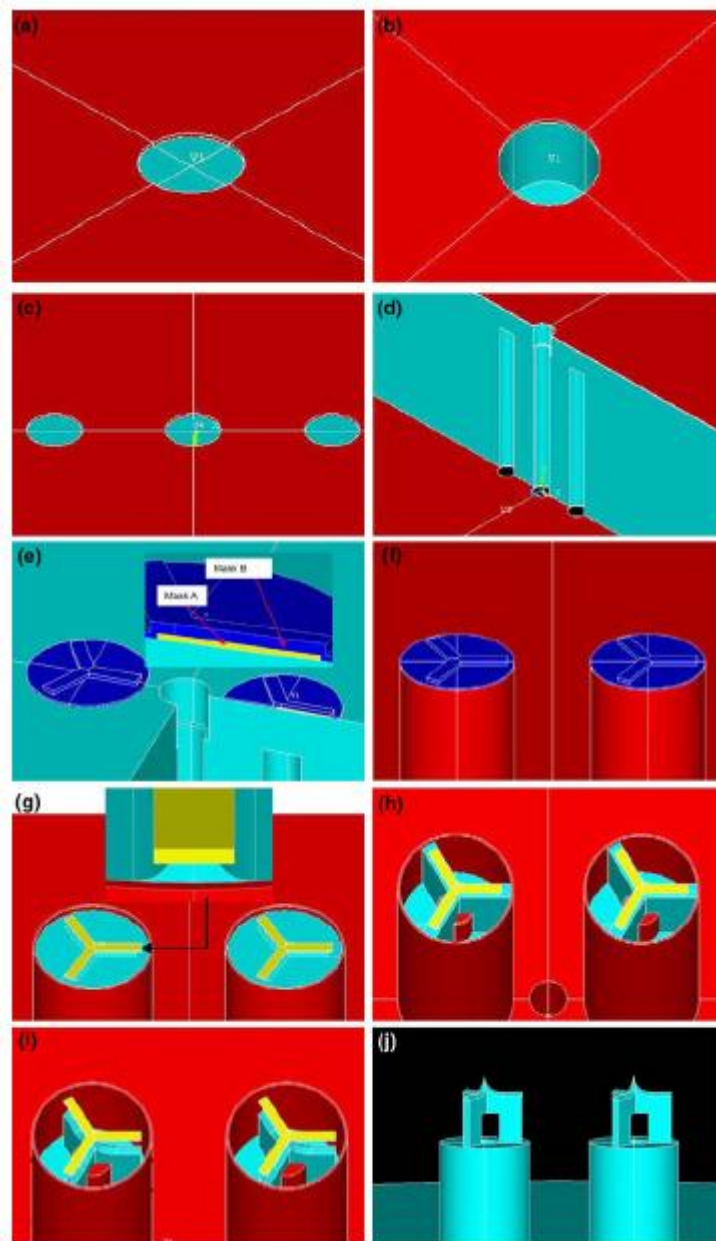


Figure 2.21: Process flow of the microneedle fabrication [45].

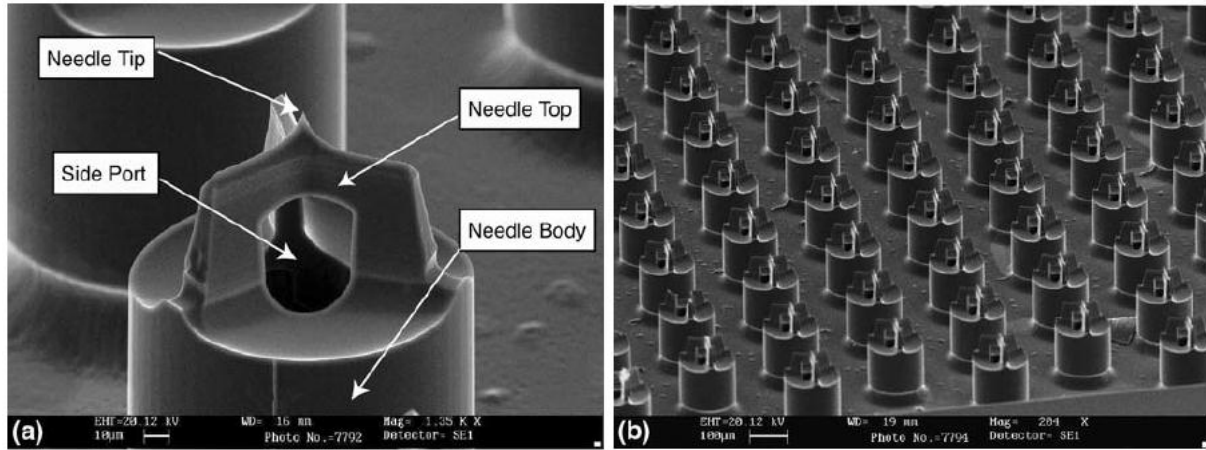


Figure 2.22: SEM image of (a) a single microneedle and (b) a microneedle array [45].

2.6.2.2. Hollow Polymeric Microneedles using Integrated Lithographic Micromolding

Microneedles can be formed by lithographic processing onto a patterned substrate surface. In this section batch fabrication of thick photoresist microneedles using SU-8 and anisotropic silicon wet etching is illustrated.

The fabrication steps are depicted in Figure 2.23. Step 1 consists of the preparation of the silicon surface. The thermally oxidized silicon wafer *a* is lithographically patterned (mask 1) and etched in BHF. Subsequently, the silica *b* is used as a mask for KOH etching of the v-grooves *c* [42]. The substrate crystallography and the mask pattern is designed such that the (111) planes meet at a depth, which is predefined by the size of the mask openings *d*, in this case 550 μm . In step 2, a first level of SU-8 100 is dispensed on the pre-patterned silicon substrate *a*, spin-coated to the according thickness *e*, which leads to the desired needle height. In step 3, the photoresist is lithographically processed using the mask 2. This forms an equidistant array of 5×5 needles with a diameter of 250 μm , a through-hole with a diameter of 75 μm and a pitch *f* of 925 μm within a total device area of the needle array of 3.95 mm \times 3.95 mm, which is aligned with a center-point symmetry in the overall back plate dimensions of 10 mm \times 10 mm after dicing. Subsequently, the exposed and baked layer *g* is developed supplying a continuous flow of propylene glycol methyl ether acetate (PGMEA) to the substrate surface. Step 4 shows the developed polymer needles *h* that are free-standing on the oblique surfaces of the v-grooves [42].

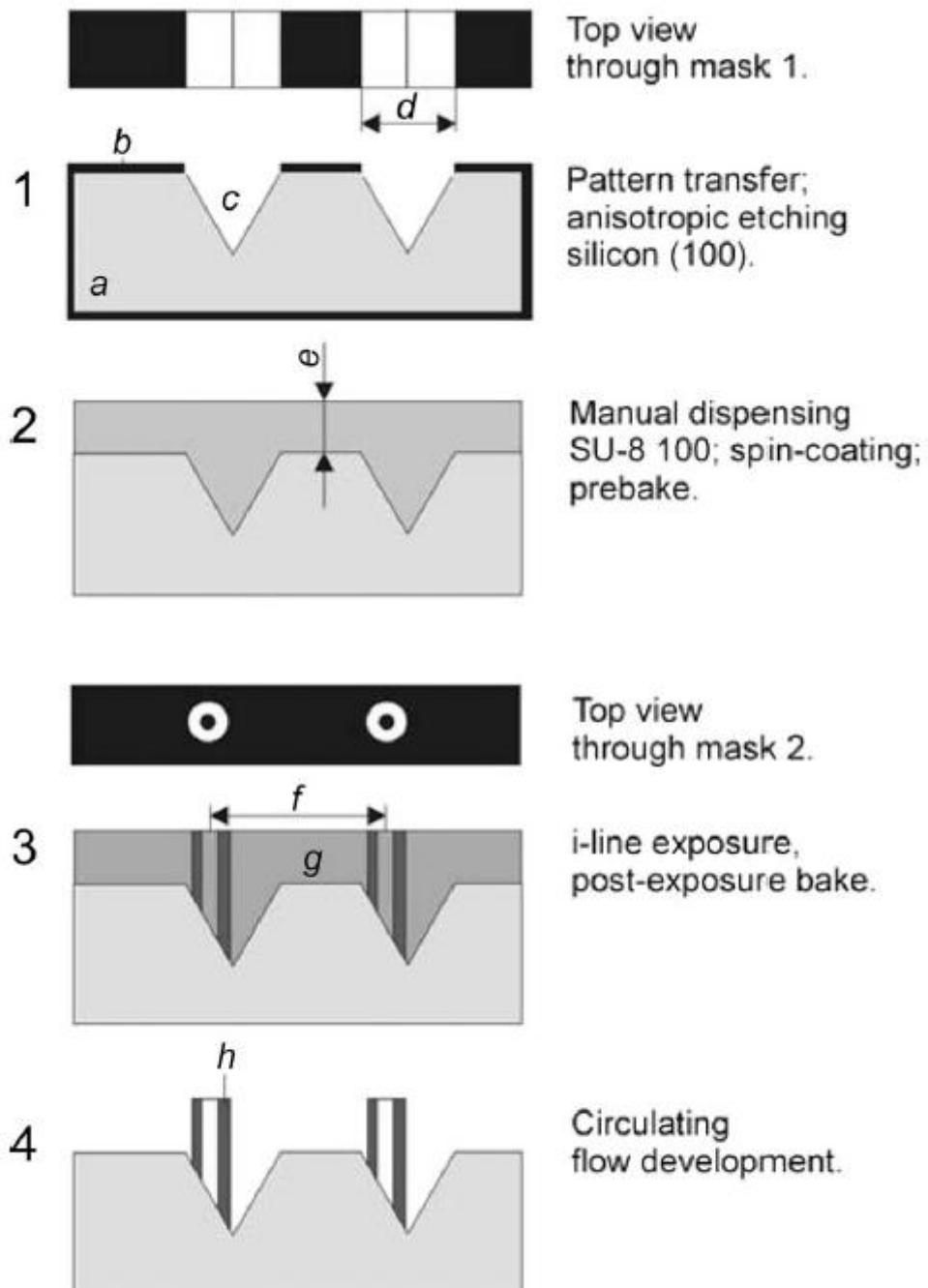


Figure 2.23: Schematic of fabrication process steps of polymer microneedles on preprocessed v-grooves [42].

Figure 2.24 shows the resulting structures fabricated in this process. An overview of the lithographic parameters for both the needles and the back plate is given in Table 2.3 [42].

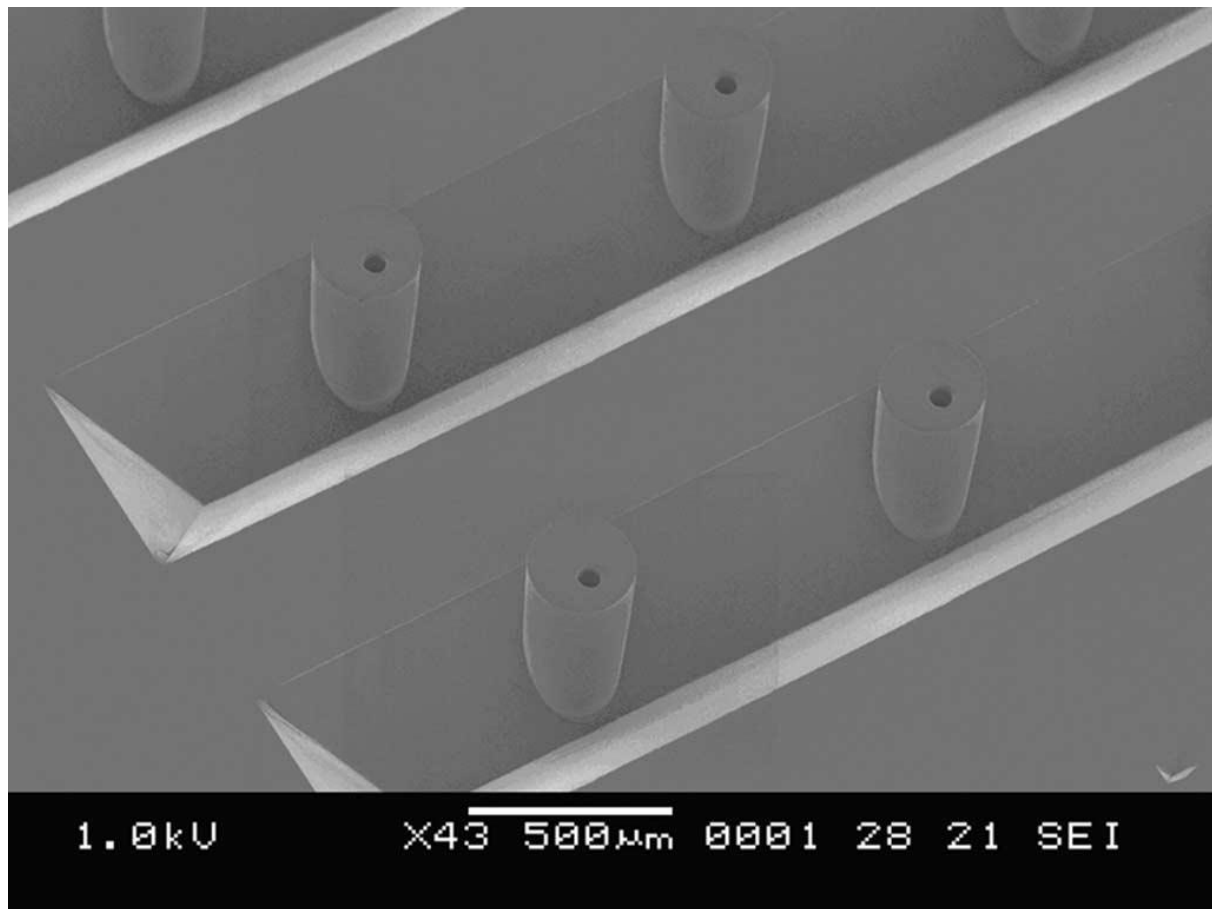


Figure 2.24: SEM at 30°. Lithographically formed SU-8 microneedles formed on top of v-grooves [42].

Table 2.3

Overview of the lithographic parameters

Process step*		1 st level: needles	2 nd level: back plate
Dehydration		120°C, 5 min	120°C, 5 min
Spin coating	(1) 20s (2) 30s	500 rpm, 100rpm/s 1000 rpm, 300rpm/s	500rpm, 100rpm/s 3000rpm, 300rpm/s
Soft bake		ramp up 90°C, 2h	ramp up 90°C, 2h
Relaxation		ramp down to RT over night	ramp down to RT over night
Exposure		180s	80s
Post exposure bake		ramp up 75°C, 20 min	ramp up 75°C, 35 min
Relaxation		ramp down to RT over night	ramp down to RT over night
Development (PGMEA)		flow-wash, 10 min	flow- wash, 45 min

To obtain an array of polymer needles a two level lithographic process is applied on the previously obtained structures. Figure 2.25 shows the various steps of the microfluidic back plate integration in detail.

Step 1 continues the process as described before, by dispensing a non-photosensitive filling layer *a* into the free-standing needle features *b*. Specific care must be taken that this polymer, e.g., non-photosensitive SU-8 epoxy resin, does not flow on top of the shaft ends of the needles. The thickness *c* of this filling layer, together with the depth of the depressions, defines the final length of the microneedles. In step 2, a second layer of photosensitive polymer *d* is applied. This layer is lithographically defined by alignment of the back plate mask (mask 1) to the needle features formed in the first SU-8 layer, which is depicted in step 3. The process parameters for the back plate lithography are listed in Table 2.3. The design contains access holes *e*, which assist in the process of development and release. Depending on a specific application the back plate thickness and the mask layout can be modified,

however, process variations then require re-optimization of lithographic parameters. Step 4 combines the development of the pattern of the backplane and the removal of the filling layer through the additional holes in the back plate hence gaining an array *f* of interconnected microneedles. In step 5 the mold is released by sacrificial layer etching method, e.g., the microneedle array can be released by etching the polysilicon selectively against nitride and SU-8 in a standard 25wt. % KOH solution at 74 °C [42].

The result of this process is shown in Figure 2.26.

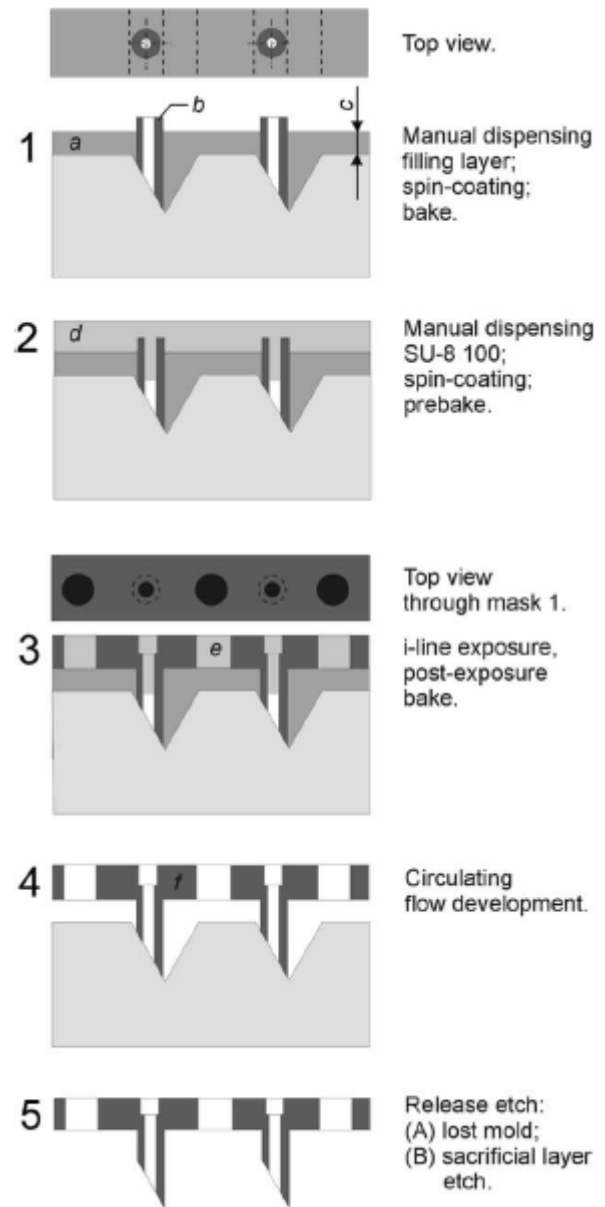


Figure 2.25: Multilevel SU-8 process with subsequent lithographic forming of a microfluidic back plate [42].

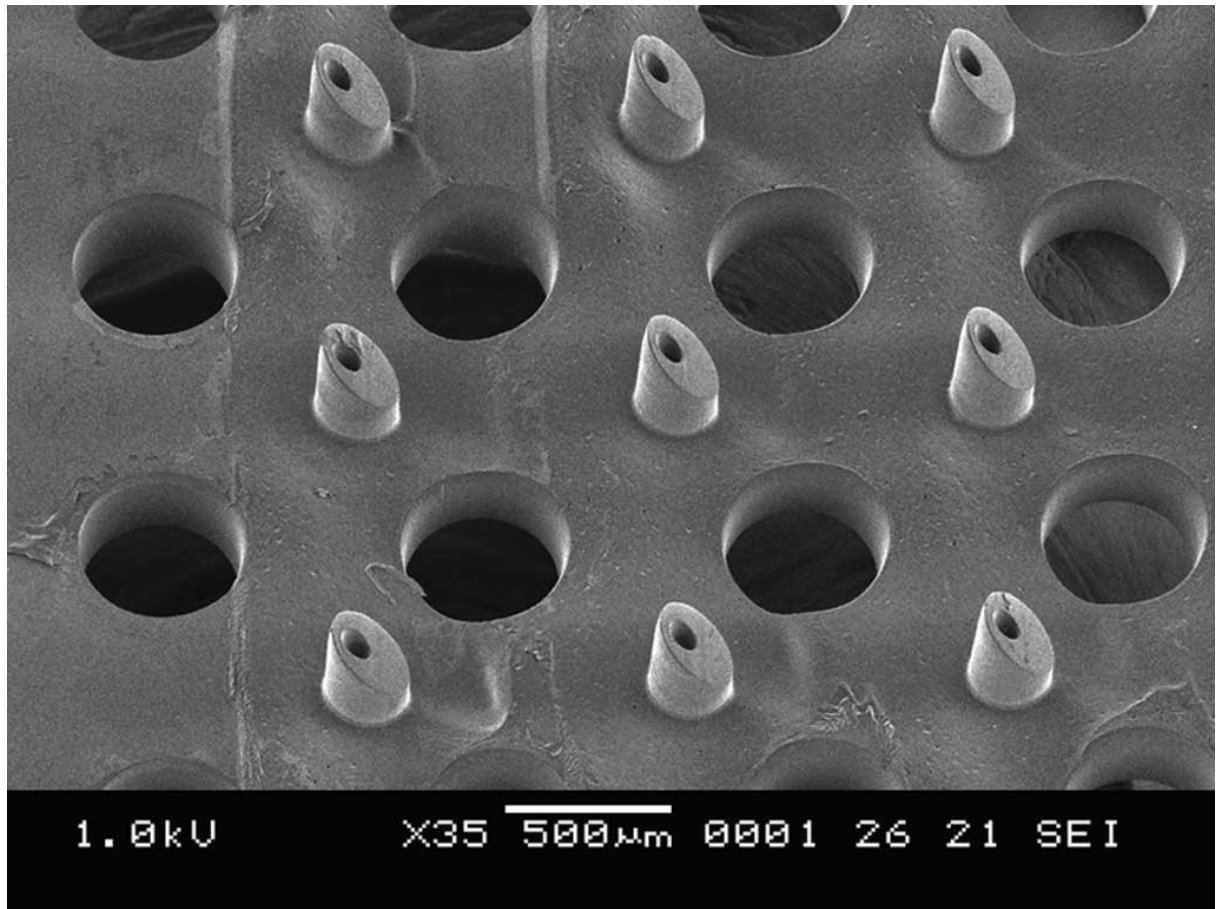


Figure 2.26: Array of needles achieved by the lithographic molding process depicted in Figures 2.23 and 2.25 [42].

2.7. Characterization of Microneedles

2.7.1. Modeling, Simulation and Finite Element Analysis before fabrication

Podder *et al.*, 2011 used the MEMS module of COMSOL to create the 3D models of both the out-of-plane and in-plane microneedles [28]. The materials of both the needles were chosen to be polysilicon (Young's modulus $E = 160 \text{ GPa}$, Poisson's ratio $\nu = 0.22$, density $\rho = 2320 \text{ Kg/m}^3$). The base planes of both the needles were considered to be fixed, while the rest of the needles were allowed to move freely. Theoretically human skin resistance is 3.18 MPa while penetrating the skin [28]. Once the skin has been penetrated, the pressure reduces to 1.6 MPa . When a Microneedle enters the skin it experiences two kinds of forces: a) Buckling force and b) Bending force.

a) *Modeling:*

A microneedle, modeled as a cantilever is shown in the Figure 2.27.

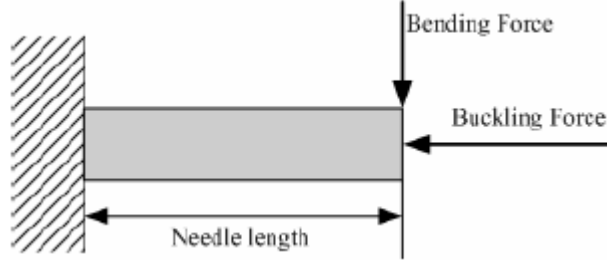


Figure 2.27: Modeling of the Micro Needle as cantilever [28]

A compressive buckling force acts on the micro-needle in the axial direction. The *maximum buckling force*, which the microneedle can withstand without breaking is given by,

$$F_{\text{MaxBuck}} = \pi^2 Y I / L^2$$

where, Y = Young's modulus, I = Geometric moment of inertia, L = Needle length.

The *maximum free bending force* that the microneedle can withstand is given by,

$$F_{\text{MaxFreeBend}} = \sigma_y I / c L$$

where, σ_y = yield stress of silicon (7 GPa) and c = distance of the outermost edge of the microneedle from the neutral axis.

The bending force has a critical effect on fracture of silicon needle structure because of silicon's brittleness. When the strain of the tip is close to the material yield strain, the structure fracture occurs.

The *resistive force* offered by the skin before the skin is punctured is given by,

$$F_{\text{Skin}} = P_{\text{Piercing}} A$$

where, P_{Piercing} = Pressure required to pierce the epidermis layer of skin = 3.18×10^6 Pa, A = cross-sectional area of the needle (tip).

The values of F_{MaxBuck} , $F_{\text{MaxFreeBend}}$ and F_{Skin} for the out-of-plane needle were found to be 50N, 1.32N and 160 mN respectively. The same for the in-plane needle were calculated as 783.6 mN, 246.5 mN and 25.5 mN respectively [28]. Since the maximum buckling force was sub-

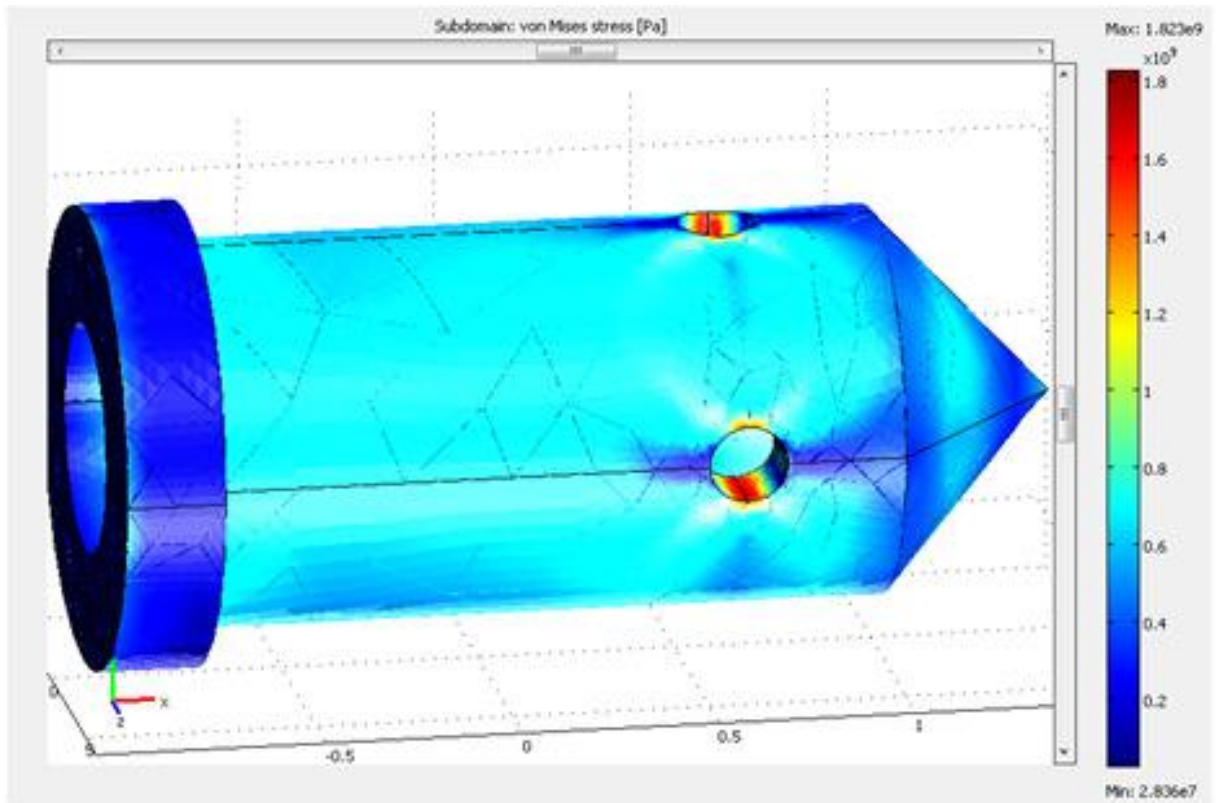
stantially larger than the skin resistance force in both cases, the out-of-plane and in-plane microneedles should be able to pierce the skin without breaking.

b) Simulation

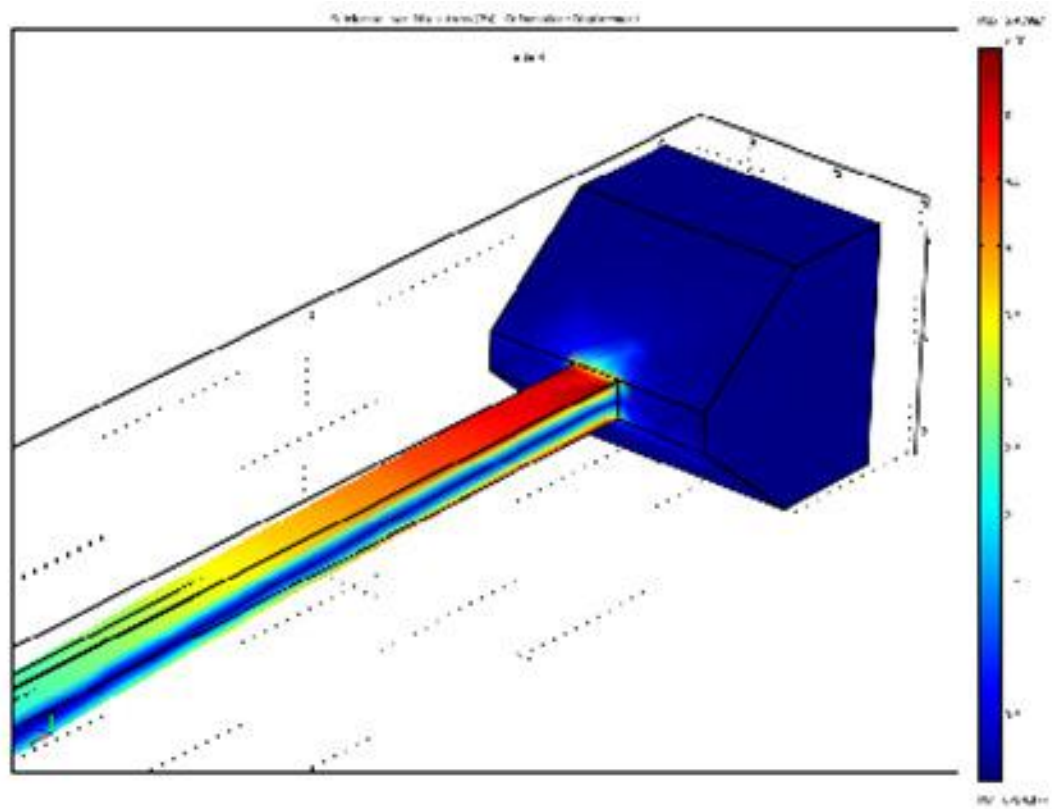
In the first step of simulation the maximum stress and deflection in the micro-needle structure were studied against different structural variables for both the out-of-plane and in-plane microneedles. It was observed that for applied buckling force, the deformation of the structure was compressive in nature and the maximum stress was generated at the needle tips for the in-plane structure [28]. But the region of maximum stress for the out-of-plane needle is around the side-ports (see Figure 2.28). It was observed that the stress was dependent on the geometry of the side-ports. On application of bending force, the deformation was deflective from the needle-axes and maximum stress was produced near the needle base for both the needles [28].

The next step was to study the maximum stress and deflection for different tip angles. It can be observed from Figure 2.29 (a, b) and 2.30 (a, b) that both the deflection and maximum stress decrease with increasing tip angle. This is expected since with the increment of the tip angle, the bending component of the applied force decreases, resulting in decrement of deflection and stress.

In the next step, the deflection, maximum stress and fluid flow rates through the needle channel under a constant pressure head was plotted for different cross-sectional area of the needle bore. It can be observed from Figure 2.31 (a) and (b) that the deflection, maximum stress and flow rate increases with increasing bore area. In case of the out-of-plane micro-needle, for a chosen bore diameter of $40\mu\text{m}$ the flow rate is almost $5\mu\text{l}/\text{second}$ and both the deflection and maximum stress are within tolerable limits. A similar study was performed for the in-plane microneedle [Figure 2.32 (a) and (b)], which allowed a flow rate of $0.064\mu\text{l}/\text{second}$ for the chosen bore area of $864\mu\text{m}^2$. The area of the wedge shaped needle-tip decreases with increasing bore area, which in turn reduces the effective force acting on the needle-tip, since a fixed distributed load (pressure) is applied. However, both the deflection and maximum stress are within tolerable limits for the in-plane needle [28].



(a)



(b)

Figure 2.28: Region of maximum stress in the (a) out-of-plane and (b) in-plane needles for buckling and bending forces respectively [28].

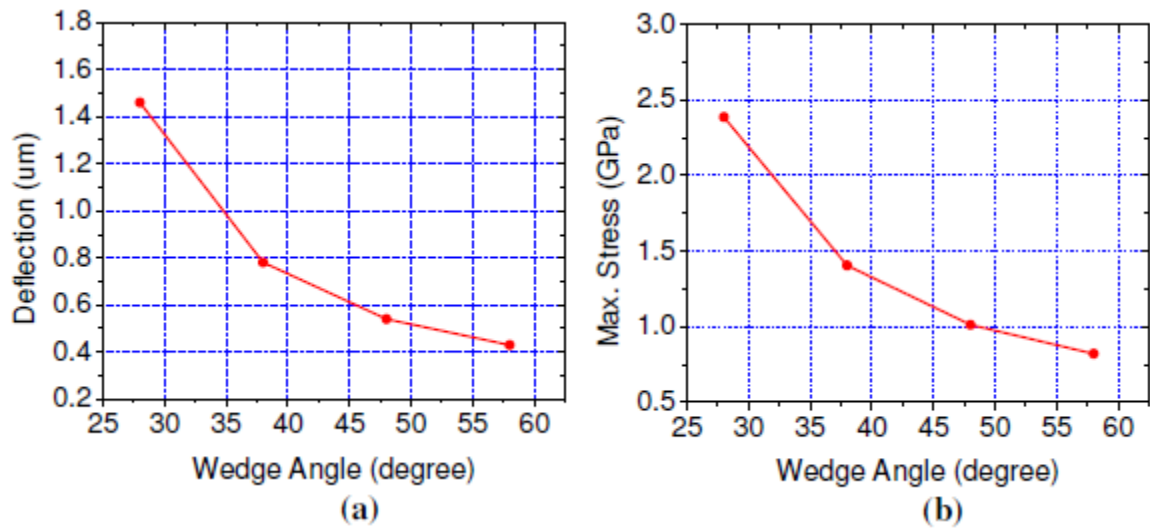


Figure 2.29: Variation of (a) Deflection and (b) Maximum stress with tip angle for out-of-plane needle [28].

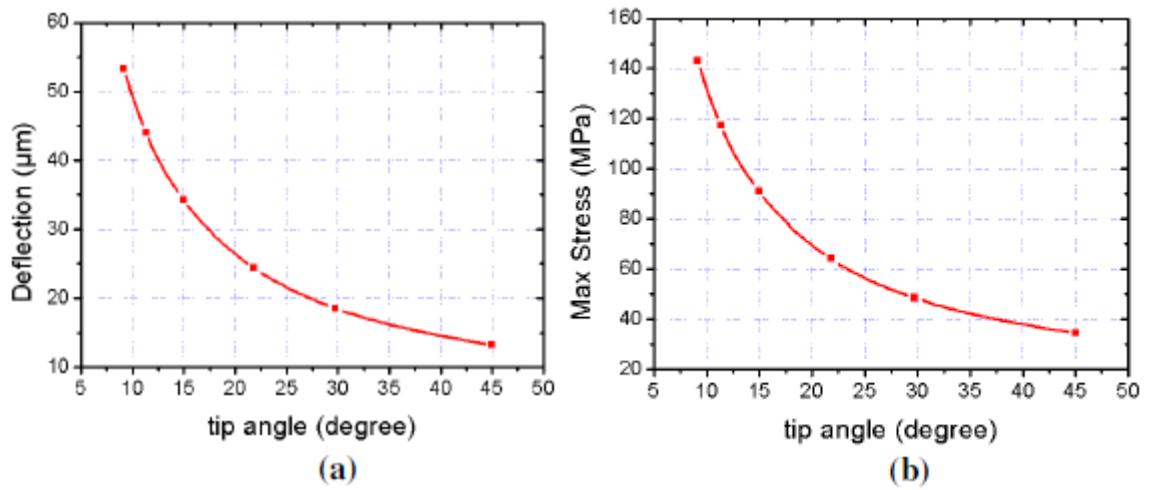


Figure 2.30: Variation of (a) Deflection and (b) Maximum stress with tip angle for in-plane needle [28].

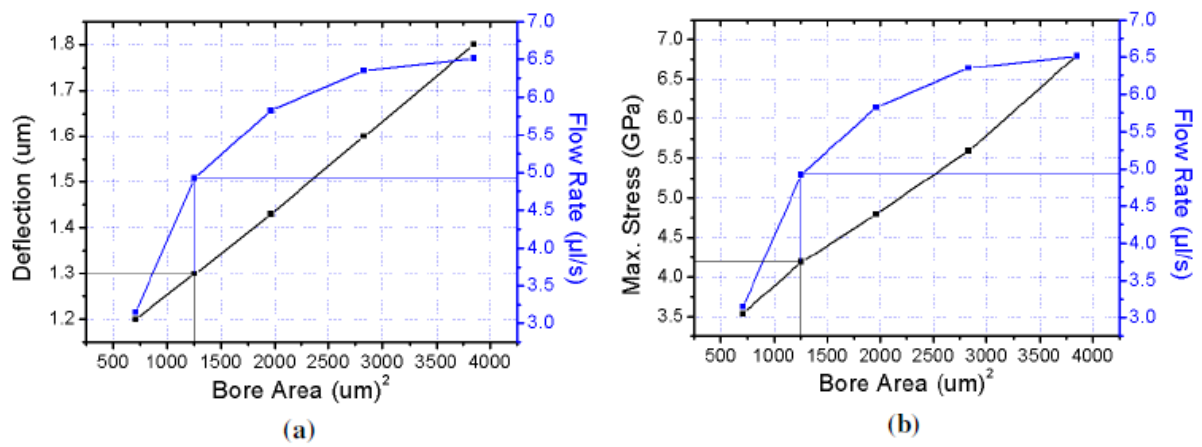


Figure 2.31: Variation of (a) deflection, (b) maximum stress and flow rate with needle bore area for out-of-plane needle [28].

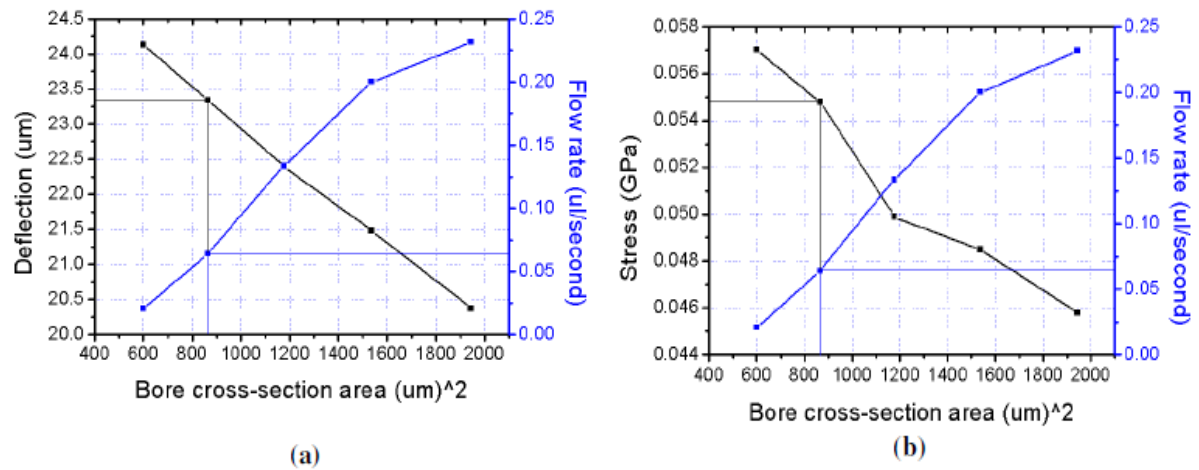


Figure 2.32: Variation of (a) deflection, (b) maximum stress and flow rate with needle bore area for in-plane needle [28].

c) FEA Analysis

Ashraf *et al.*, 2010 has used Finite Element Analysis (FEA) method to perform structural analysis and fluidic analysis, on single out-of plane hollow microneedle and 6x6 microneedle array, respectively, using ANSYS. Linear isotropic material properties of silicon (Young's modulus of 169 GPa, of 0.22 and Fracture strength of 7 GPa) were used for FEM analysis [27] [57]. In the simulation study, bending and axial stress analyses were performed by applying transverse and axial loads respectively. The range of transverse load is assumed according to the fracture strength of the material. For stress analysis the bottom of the microneedle was taken into consideration with applied tip force 8.8 N as shown in Figure 2.33.

Results show maximum stress of 6.96 GPa occurs at inner part of tip that is less than the yield strength of materials. In another study [57] they have used different element model and shown that maximum stress of 5.05 GPa occurs at the bottom of the microneedle for the applied bending force of 8.2 N, which is also below the yield strength of the material. Human skin resistance is 3.18 MPa during needle penetration [27]. So microneedle is strong enough to bear load more than 3.18 MPa. The effect of applied pressure on tip of microneedle is shown in Figure 2.34 [27].

Simulation results of axial stress analysis shows that the maximum stress 2.96 MPa occurs inside the lumen section of the microneedle at applied pressure of 3.18 MPa with negligible deflection [27]. These analyses show that the microneedle design is strong enough to penetrate into the human skin without failure.

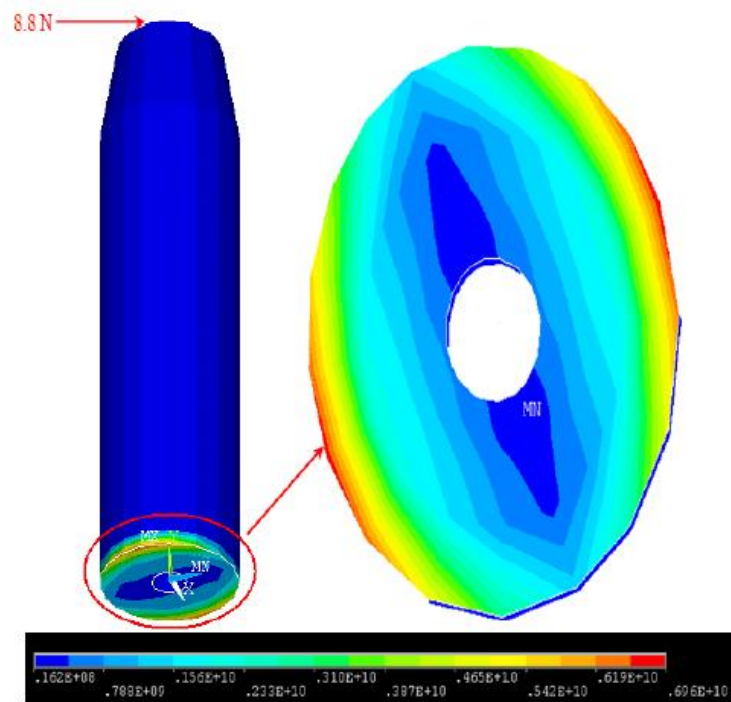


Figure 2.33: Bending stress analysis [27].

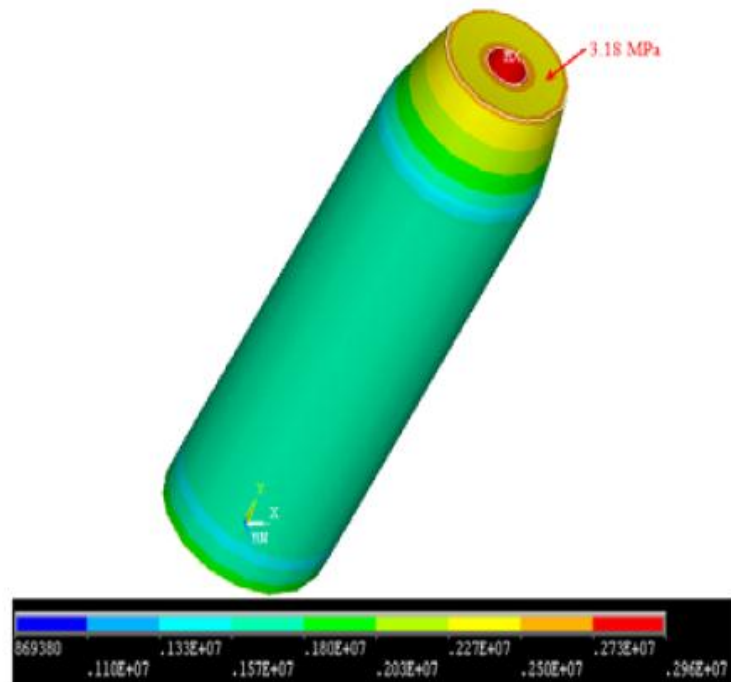


Figure 2.34: Axial stress analysis [27].

2.7.2. Mechanical Analysis

Paik *et al.*, 2004, have also performed FEM simulation (using ANSYS) to ascertain the mechanical stability of microneedles for optimizing its length, width and thickness of its shaft [58]. Their result (Figure 2.35) shows that the vertical bending load of 130mN induces a maximum stress of approximately 1GPa, which is near the fracture stress limit of silicon cantilevers used as a model for in-plane microneedles [58].

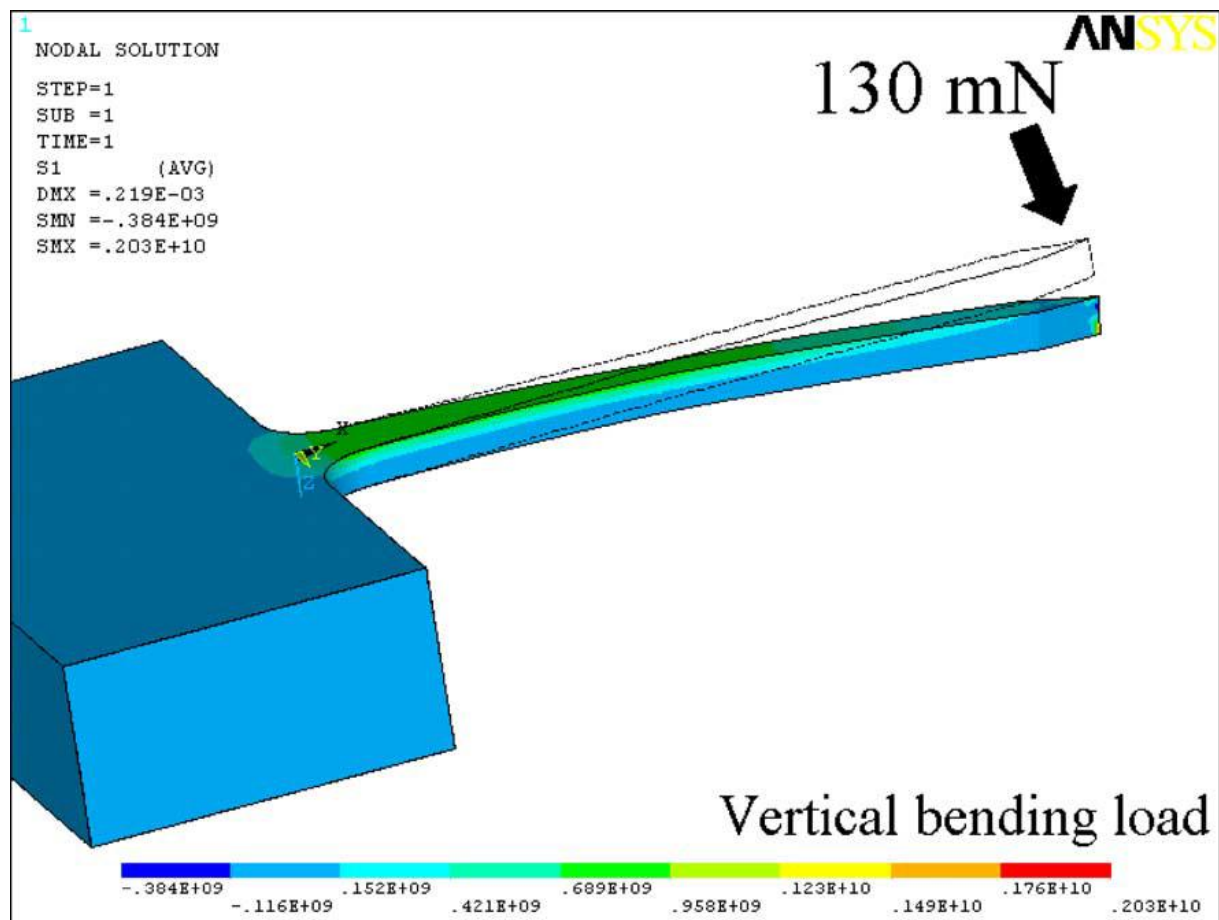


Figure 2.35: FEM simulation analysis for the stress of microneedle shaft. The vertical loading of 130mN induces maximum stress of about 1 GPa [58].

In order to investigate the mechanical stability of the microneedle array, out-of-plane bending fracture tests, in-plane buckling tests, and penetration tests for chicken breast flesh were performed. Bending fracture forces and penetration forces were measured with a load cell of 1.47N (150 gF) capacity and buckling forces were measured with another load cell of 5.88N (600 gF) capacity with 150% safe overload rate [58]. Experimental break tests of the microneedle shafts indicate that out-of-plane bending force for microneedle breakage is smaller than any other applied forces and that microneedles with the tip taper angle 30° and the isos-

celes triangle tip shape is the most robust against buckling load. The maximum average bending load, which caused microneedle shaft to be broken, was 124mN, which is consistent with the FEM simulation results of 130 mN. From the FEM simulation, bending moment more than 0.248mNm induces a maximum stress of approximately 1GPa, which is near the fracture stress limit of silicon cantilever [58]. Therefore, out-of-plan bending moment more than 0.248mNm would cause breakage of the microneedle shaft.

In-plane buckling tests were performed on the microneedle shafts different types of designs, each having sharp tip at the end of microneedle shaft. Microneedles with the tip taper angle 30° and the isosceles triangle tip shape showed better mechanical stability compared to other tip shapes, with an average buckling force of 6.28N and average penetration force required to penetrate the chicken breast flesh to be 80.9 mN. The theoretical buckling critical load of the microneedle shaft used in this analysis was 7.1N under the assumptions that the Young's modulus for silicon is 168.9 GPa [58].

2.7.3. Flow Analysis

Fluid flow characteristics are extremely important if the microneedle array is used to inject the fluidic drug or vaccine into human skin. Fluid pressure drop through the microneedle array is based on various reasons like microneedle array geometry, roughness of surface, fluid viscosity, and microneedle array density. The dimensions of microneedles are in microns, so the behavior of fluid flow is different from macro level. There is significant resistance to fluid flow through the microneedles. Poiseuille's law is considered to measure the fluid flow through microneedle array as shown below [27]:

$$Q = \frac{\pi D_1^4 (\nabla p)}{64 \mu (L)}$$

where, Q is the flow rate, D₁ is the diameter of microneedle, delP is the pressure difference between inlet and outlet of the microneedle and μ is the viscosity of fluidic drug.

Modified Bernoulli equation is considered to model the microneedles geometry. The pressure loss is calculated by considering the friction losses given by [27]:

$$\frac{P_1}{\rho g} + \frac{V_1}{2g} + Z_1 = \frac{P_2}{\rho g} + \frac{V_2}{2g} + Z_2 + \frac{fl}{d} + \frac{V^2}{2g} + \sum \frac{kV^2}{2g}$$

where, P_1 is the inlet pressure, P_2 is the outlet pressure, V_1 is the inlet velocity and V_2 is the outlet velocity and other symbols represent their conventional properties as per Bernoulli's equation.

2.7.4. CFD Analysis

Effect of different applied inlet pressures on the flow rate was simulated by Ashraf *et al.*, 2010, on single row of microneedle array (6 microneedles). The static pressure 20 kPa to 140 kPa was applied at the microneedle inlet. Isothermal fluid domain was chosen for analysis during the simulation. Ethanol was considered for flow analysis in isothermal domain. The simulation results for the applied inlet static pressure are shown in Figure 2.36.

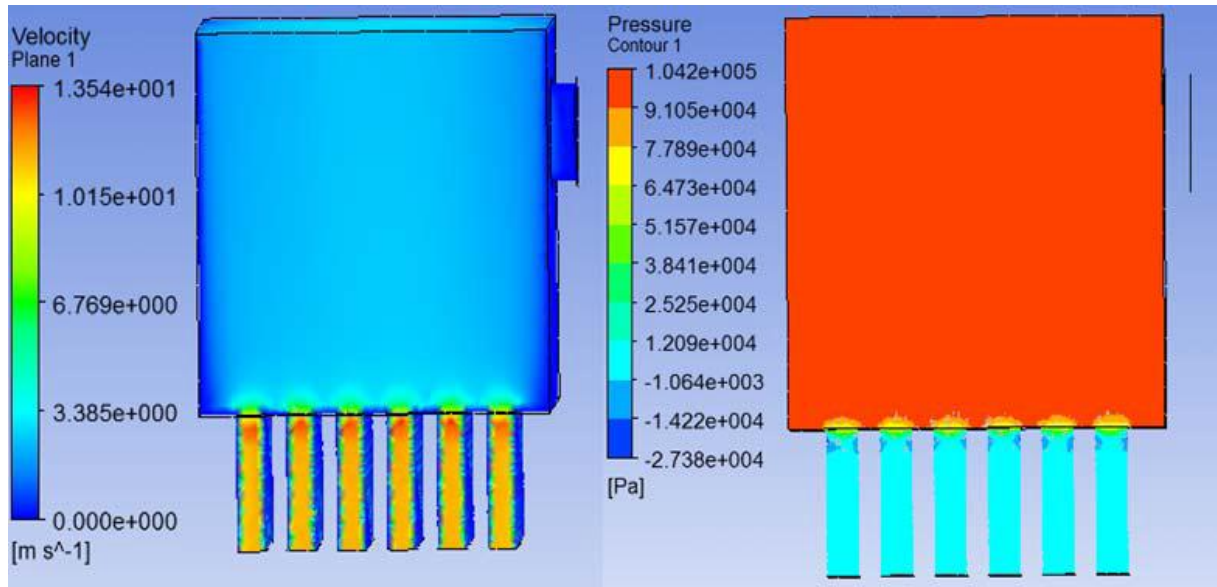


Figure 2.36: Velocity and pressure distribution in CFD static analysis [27].

The result shows that the fluid velocity is negligible in the reservoir due to large area. Velocity of fluid increases in the microneedle lumen section and along the length due to small area [27]. Due to frictional losses between fluid and wall, the fluid velocity is less near wall as compared to the central region of lumen section. Pressure is high and remains constant in the reservoir. It decreases in the lumen because the fluid is flowing towards the outlet (Pressure at outlet considered to be 0 kPa).

2.8. Delivery of vaccines using microneedle

This section is primarily focused on the transdermal delivery of vaccines and antigenic proteins using the microneedle described in section 2.6.

2.8.1. Coating of vaccines on microneedles

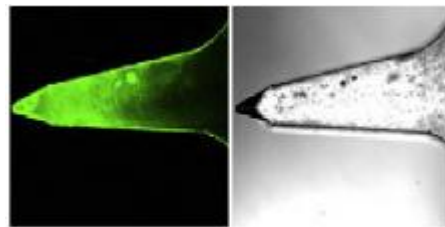
Microneedles have been coated by a variety of processes, most of which involve dipping or spray coating the microneedles using an aqueous solution having high viscosity for efficient retention during drying; a surfactant to facilitate wetting of the microneedle surface; a vaccine; a preservative and in some cases a stabilizing agent to protect the drug from damage during drying and storage [39]. Coating of thin film of solution on individual microneedles tips helps in better localization of vaccine and does not contaminate the base substrate.

Layer-by-layer coating technique i.e., alternately dipping into two solutions containing oppositely charged solutes, to form a polyelectrolyte multilayer is an advanced coating technique and has been found to be efficient in coating of protein antigens [39]. Spray coating of solution onto the microneedles involves an angled gas jet to spray the surface of individual microneedle shafts.

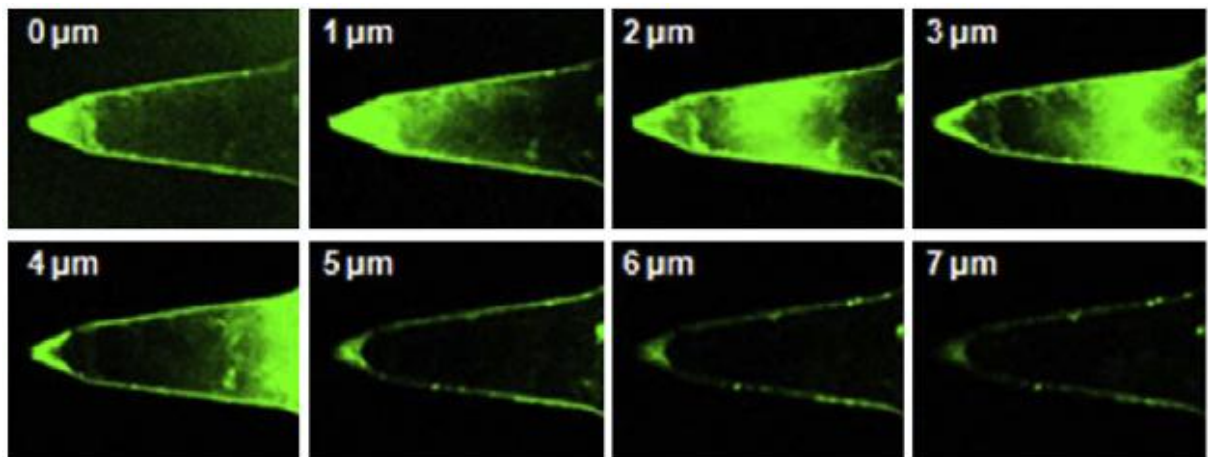
Kim *et al.*, 2010, have used dip coating method to coat 3-8 mg/ml solution of influenza VLP vaccine on stainless steel microneedle array [41]. The coating solution was composed of 0.25-1.0% (w/v) carboxymethylcellulose (CMC) sodium salt (a viscosity enhancer, enable thicker coating by increasing coating solution residence time on microneedles during drying), 0.5% (w/v) Lutrol F-68 NF (a surfactant, generate uniform coating by reducing surface tension) in PBS. Trehalose at a concentration of 5-30% (w/v) was used as a stabilizer to prevent the loss of VLP HA (hemagglutinin) activity during drying. This standard coating formulation was able to coat influenza VLP vaccine onto microneedles and on transdermal administration the vaccine coating was efficiently dissolved and released into the skin almost completely [41].

Han *et al.*, 2009, have coated ovalbumin antigen on grooves-embedded PLA microneedles using different pre-coating solutions. First coating method used a solution containing 0.01% PLL (poly-L-lysine) in phosphate-buffered saline (PBS) at room temperature for 2 h [50]. Second solution used 3% APTS (3-aminopropyltriethoxysilane) in ethanol for 1 h at room temperature. Third method used a solution of 2.5% GPTS (3-glycidoxypyltrimethoxysilane) with 5% acetic acid in ethanol, kept at room temperature for 2 h. After microneedle coating

was finished, protein coating was performed under ambient conditions (4 °C, 30–40% relative humidity) using an apparatus in which the microneedle was soaked for 1 h. To confirm protein coating, using above described three coating methods using PLL, APTS, or GPTS, coated microneedles were incubated in Alexa Fluor 488 conjugated goat anti-mouse solution (Molecular Probe) for 1 h at room temperature. After the microneedles were washed with PBS three times for 5 min, they were measured with confocal microscopy. Figure 2.37a shows fluorescence and gray images of the protein coated surface of each type of microneedle and Fig. 2.37b shows fluorescence images at intervals of 1 μm on the z-axis using a confocal microscope. Images show that the proteins were coated on the whole surface and the thickness of the coated protein was approximately 1-2 μm [50].



(a)



(b)

Figure 2.37: Images of protein-coated microneedles of the three types of microneedles (a) and fluorescence image on the z-axis at intervals of 1 μm on an A type microneedle (b). Microneedles were coated with Alexa Fluor 488-conjugated goat anti-mouse Ig and then imaged under a confocal microscope (the height of the microneedle is 0.9 mm) [50].

Sullivan *et al.*, 2010, have used room-temperature (23 °C) photo-polymerization of liquid vinyl pyrrolidone within a microneedle mold to form polyvinylpyrrolidone (PVP) microneedles that encapsulate the lyophilized vaccine [59]. This process avoids the need for organic solvents or elevated temperatures that can damage vaccine or other biomolecule stability. PVP

were chosen as the structural material for the polymer microneedles used in this study because it is biocompatible, mechanically strong and highly water soluble.

Chen *et al.*, 2011, have used fast nitrogen gas-jet (~ 10 m/s), at an incident angle (α) of 20° or 70° , to coat a solution containing methylcellulose and Fluvax® 2008 onto Nanopatches [54]. It resulted in a very thin (<50 nm) uniform coating of vaccine on the surface of the microprojections at $\alpha = 20^\circ$. It took about 3 min to coat each individual patch using this condition. At $\alpha = 70^\circ$, the coating became much thicker on the conical part of the microprojections, while it was still thin on the cylindrical part of the microprojections and the base of the patch. The coating thickness at the bottom of the conical part was measured to be 0.54 ± 0.05 μm [54]. It took about 5 min to coat each individual patch under this condition.

2.8.2. Preparation of skin

Pig skin, rat skin and human cadaver skin are most commonly used in studying transdermal drug delivery, due to their morphological similarities with living human skin [54] [59][35] [60]. The skin sample is processed to remove hair, subcutaneous fat and other debris to mimic the full thickness skin having thickness of about 1-1.5 mm. Then it is washed with physiological saline and stored at -20°C till its use [35]. For studies specific to vaccine delivery, the skin sample might be further processed to remove the dermis layer to better simulate the penetration requirement of microneedles meant for vaccine delivery, as they are expected to penetrate only through the stratum corneum and epidermis [61]. The stratum corneum side should be carefully wiped with 70% ethanol and deionized water before penetration. Verbaan *et al.*, 2008, prepared Dermatomed human skin by fixing full thickness skin on a Styrofoam support and then having it dermatomed to a thickness of 300–400 μm [60]. The skin was stored at -80°C until use, except for transport and confocal studies where only fresh human skin was used.

2.8.3. Penetration of skin

Sullivan *et al.*, 2010, have shown the penetration of porcine cadaver skin by PVP microneedles (Figure 2.38a), 650 μm in height, having fracture force of 0.13 ± 0.03 N per needle and encapsulating inactivated influenza virus, which successfully penetrated (Figure 2.38b) to a depth of approximately 200 μm and deposited their encapsulated payload largely within the epidermis (Figure 2.38c, d) [59].

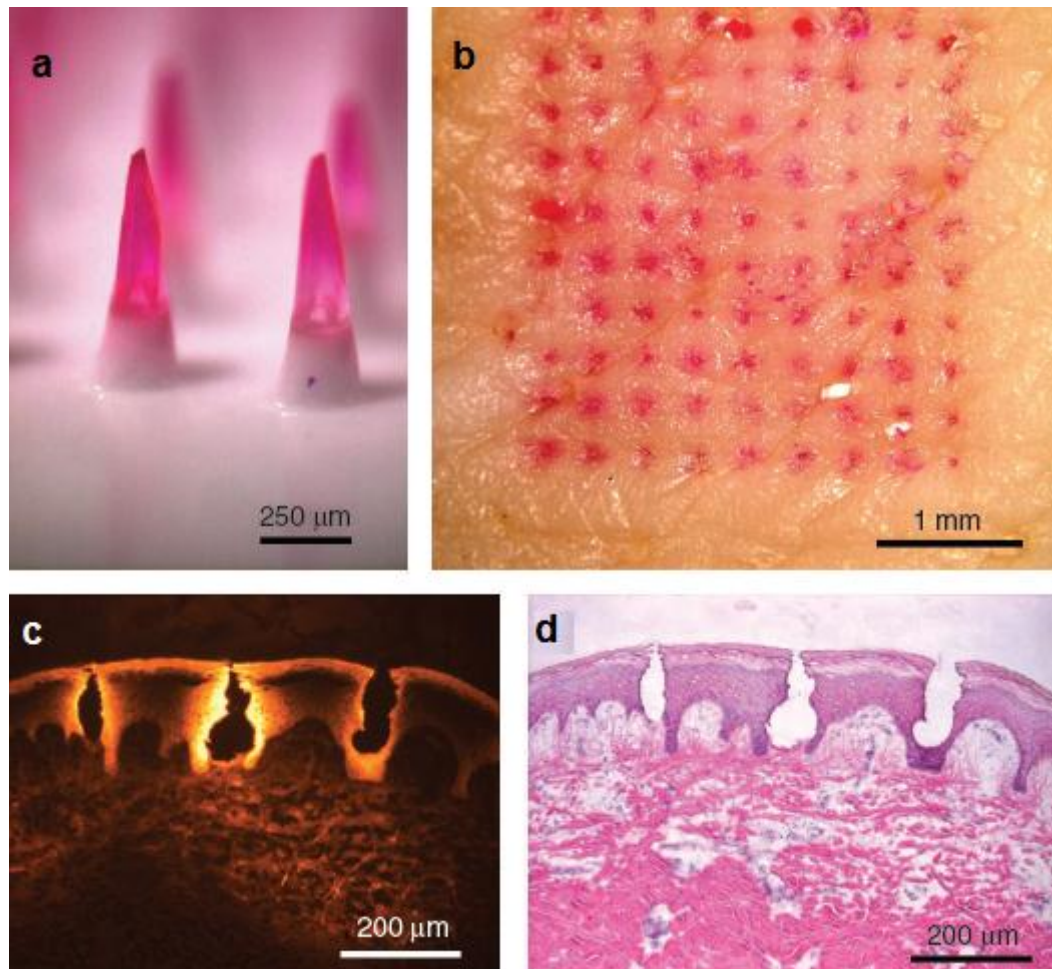


Figure 2.38: Dissolving polymer microneedle patches. (a) Side view of dissolving polymer microneedles. (b) En face view of porcine cadaver skin after insertion and removal of microneedles, showing delivery of the encapsulated compound (sulfurhodamine). (c) Fluorescence micrograph of pig skin histological section after insertion of dissolving microneedles ex vivo. (d) Bright-field micrograph of the same skin section with H&E staining [59].

Chen *et al.*, 2011, have used a custom spring-loaded plunger based applicator (with a velocity of 2 m/s and a force of 0.6 N) device for penetration of skin on the inner earlobe of mice [54].

Verbaan *et al.*, 2008, used full thickness skin or dermatomed human skin (300–400 μm) which was stretched on parafilm, to counteract the elasticity of the skin, and was supported by Styrofoam, to protect the microneedles from damage, and pierced using the electrically driven applicator [60]. The skin was pierced with the applicator using either a velocity of 3 m/s or by manual piercing of the skin. To evaluate the uniformity of piercing, the stratum corneum-side of the pierced skin was covered with 0.4% Trypan Blue dye in phosphate buffer saline (PBS: NaCl: 8 g/l, KCl: 0.4 g/l, KH₂PO₄: 0.4 g/l, Na₂HPO₄: 2.86 g/l) for 1 h. The excess dye was then removed and the skin or epidermal sheet was evaluated for the appearance of blue dots on the dermal side of the skin or epidermal sheets. To visualize the conduits in dermatomed human skin, polystyrene nanoparticles containing fluorescein 5-isothiocyanate (FITC) with a

size of 200 nm were applied to human skin pretreated with the solid metal microneedle arrays using the electrical applicator. Piercing velocity was 1 or 3 m/s. After piercing the skin was placed in a Franz diffusion cell and 200 μ L of a particle solution was applied for 1 h. Afterwards the excess formulation was removed from the skin surface and the skin was washed three times with phosphate buffer with a cotton swab. The skin was mounted on a sample holder and visualized with a confocal laser scanning microscope. The image (Figure 2.39) was captured using argon laser at 488 nm wavelength, with a 515/30 nm emission filter [60].

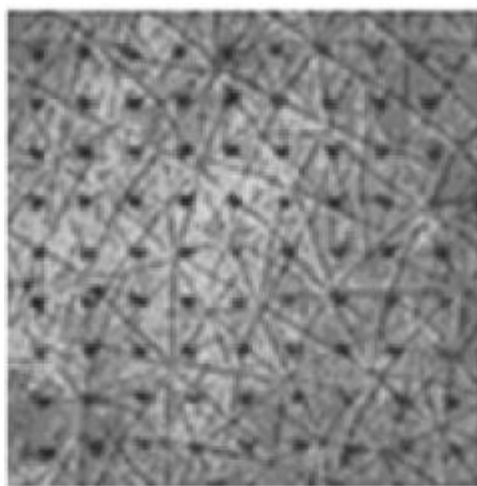


Figure 2.39: Piercing of 9×9 hollow silicon microneedle arrays across dermatomed human skin when applied with a velocity of 3 m/s. Piercing was visualized with the Trypan blue assay [60].

2.8.4. Dissolution of microneedles and Release kinetics of vaccine

Sullivan *et al.*, 2010, characterized the kinetics of dissolution of PVP (polyvinylpyrrolidone) microneedles in porcine skin and found significant dissolution to take place within 1 min, and almost 90% (by mass) dissolution after 5 min. dissolved (Figure 2.40a). Dissolution of similar microneedles encapsulating inactivated influenza vaccine was found to be slower but nonetheless increased with time, depositing $34\pm 17\%$, $63\pm 10\%$ and $83\pm 6\%$ of the polymer in the skin after 5, 10 and 15 min, respectively, and leaving almost no residue on the skin surface (Figure 2.40b) [59].

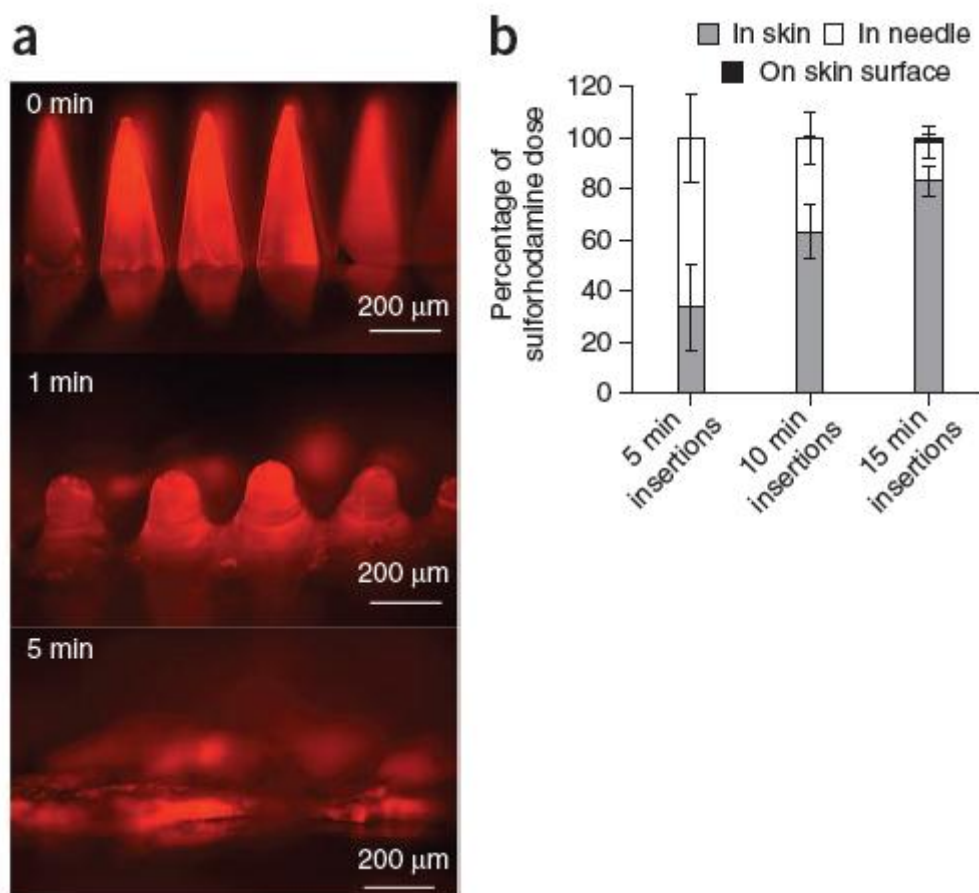


Figure 2.40: Delivery to skin using microneedles. (a) Polymer microneedle dissolution in pig skin ex vivo. Top, before insertion; middle, remaining polymer 1 min after insertion in skin; bottom, remaining polymer 5 min after insertion in skin. (b) Dissolving microneedle delivery efficiency to mice in vivo. Sulforhodamine was encapsulated within microneedles and administered to mice [59].

Kim *et al.*, 2010, assessed the release kinetics of influenza VLP vaccine delivered into human cadaver skin after labeling the VLPs with a red fluorescent compound (R-18) and visualizing them using fluorescence and multi-photon microscopy [41]. It was found that the coated VLP vaccine was efficiently released from microneedles after insertion into human cadaver skin within 2 min (Figure 2.41a). VLP-coated microneedle incubated in PBS for 1 h demonstrated complete release [41]. To assess the localization of VLP vaccine after delivery into skin, histological sections were prepared after microneedle delivery of fluorescently tagged VLP into human cadaver skin and viewed by multi-photon microscopy. The representative image in Figure 2.41b shows the microneedle insertion point (white arrow) and the deposition of VLP vaccine along the needle track in the skin. Some vaccine appears to have diffused horizontally away from the insertion site. Altogether, these results indicate that VLPs can be coated onto the surface of metal microneedles and efficiently released into the skin.

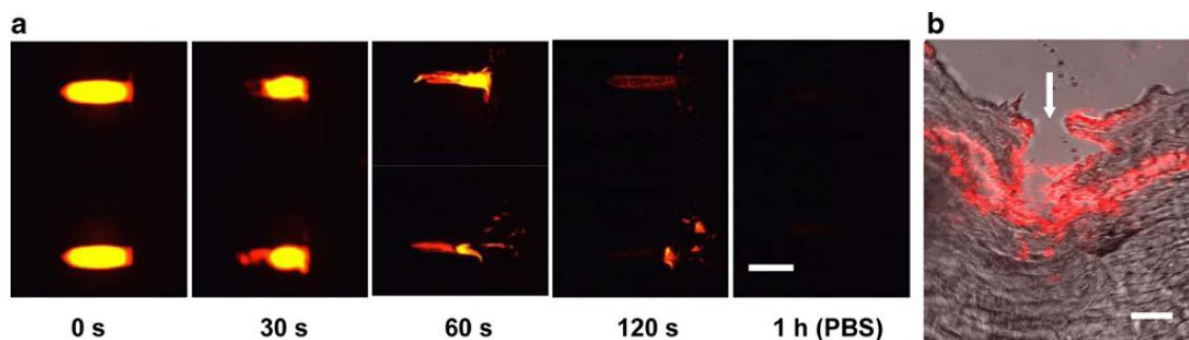


Figure 2.41: Influenza VLP vaccine delivery from coated microneedles into skin. a) Representative fluorescence micrograph of microneedles coated with red-fluorescent, R18-stained VLPs (left) and after insertion into human cadaver skin for 30, 60, and 120 s. As a positive control to confirm complete release of VLPs from the microneedles, microneedles were incubated in PBS for 1 h (right; scale bar 500 μm). b) Multiphoton fluorescence micrograph of cryo-sectioned human cadaver skin after insertion of R18-stained VLP-coated microneedle (white arrow microneedle insertion site, scale bar 300 μm) [41].

2.8.5. Permeation studies

Xie *et al.*, 2005, performed *in vitro* permeation studies with unjacketed Franz diffusion cell having a 0.785-cm² diffusion area, using a sharp-tip silicon microneedle array [35]. The receptor compartment of the Franz diffusion cell had a volume of 7 mL, and was maintained at 37 °C by means of a water bath. The receptor compartment was filled with PBS with a pH of 7.4. The solution in the receptor compartments was continuously stirred at 400 rpm using a Teflon-coated magnetic stirrer. The microneedle arrays containing the drug-loaded films (calcein and BSA) were manually pressed into rat skins. Then the full-thickness skins were clamped between the donor and receptor chambers of a vertical diffusion cell with the SC side in contact with the donor phase. The top of the cell was covered with plastic wrap to prevent water loss. The amount of the essential model drug diffused through rat skins was determined by removing aliquots of 200 μL from the receptor compartments using a syringe and immediately replacing the same volume of solution (kept at 37 °C) [35]. Calcein fluorescence was quantitated by fluorometry and compared with standard curve using a spectrofluorometer with an excitation wavelength of 494 nm and an emission wavelength of 517 nm. The concentrations of BSA solution were determined by the UV method with UV spectrophotometry. Background control samples were the chitosan films without drugs applied on treated skin with microneedle arrays.

Figure 2.42a shows the relationship of the cumulative permeated calcein amount and time. Each data point is the mean of 3 independent measurements with a 100- μg calcein loading on a 0.16-cm² surface area. Background control samples were the chitosan films without calcein. Curve *a* in Figure 2.42a represents calcein transport through rat skin in the presence of mi-

croneedles. Curve *b* in Figure 2.42a represents transdermal delivery of calcein in the absence of microneedles and the rat skin untreated with microneedles. It shows that calcein did not easily penetrate skin by passive diffusion, although it is a relatively small molecule (molecular weight, 623 D). The skin permeation rates of calcein are 50 $\mu\text{g}/\text{cm}^2/\text{h}$ with microneedles and 1 $\mu\text{g}/\text{cm}^2/\text{h}$ without microneedles [35]. The results indicate a significant increase in the permeation of calcein through skin after the microneedles treatment. Figure 2.42b shows the amount permeated through rat skin normalized by surface permeation ($\mu\text{g}/\text{cm}^2$) as a function of time (hours) from a set of various concentrations of chitosan matrix containing 6250 $\mu\text{g}/\text{cm}^2$ of BSA (molecular weight, 66,000 d). By comparing various chitosan contents, it was found that the permeation rate was strongly dependent on matrix content.

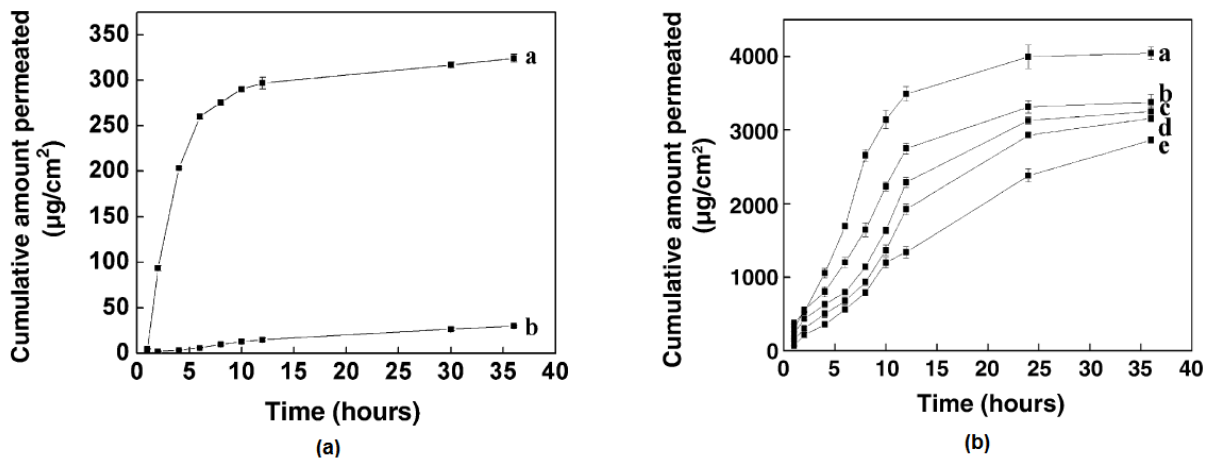


Figure 2.42: (a) In vitro transdermal permeation of calcein in the matrix of chitosan following pretreatment with or without microneedle array. (b) In vitro transdermal permeation of BSA in the matrix of chitosan loaded onto a microneedle array. Curves *a* to *e* represent 0%, 0.5%, 1%, 2%, and 3% (wt./v.) of the concentrations of chitosan from the top down, respectively [35].

Park *et al*, 2005, used a similar methodology to measure the skin permeability using PGA microneedles of different heights and tip-shapes. The ability of polymer microneedles to pierce into skin was assessed. An array of beveled-tip microneedles was inserted into the epidermis of human cadaver skin and then removed. After briefly applying Trypan blue dye to the outer, stratum corneum side of the skin and then wiping it off, the inner, viable epidermis side of the skin was examined by light microscopy to image sites where microneedles increased skin permeability and thereby permitted transport of the dye into the skin [44]. Figure 2.43(A) contains a representative optical photomicrograph that shows the resulting array of blue dots on the underside of epidermis in the same shape and location as the needle array. This indicates that the polymer microneedles successfully inserted into skin without breaking, as confirmed by subsequent microscopic examination of the needles afterwards, and increased skin perme-

ability in a highly localized manner at the sites of needle insertion. To provide additional visual evidence that polymer microneedles insert into skin, beveled-tip polymer microneedles were inserted into epidermis and left in place. The needles used in this case were notched along the sides, which may be of use in future applications as a conduit for drug transport while needles remain inserted within skin. After chemically fixing and dehydrating the skin, Figure 2.43(B) shows fully intact needles that pierced through the epidermis. In this image, the epidermis is dehydrated and therefore has collapsed down to the base of the microneedles. Figure 2.43(C) shows a companion image of skin taken after needles were inserted and removed from skin before fixation and dehydration, showing residual holes in the skin [44].

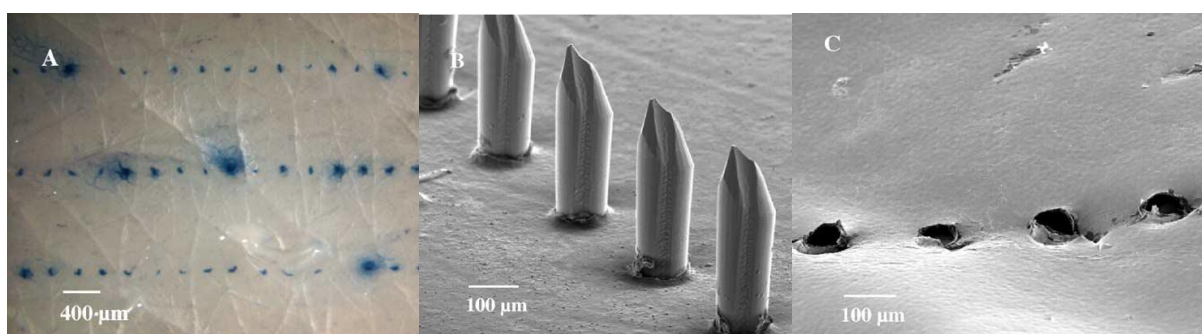


Figure 2.43: Holes pierced across human cadaver skin. (A) Optical micrograph of the underside of human cadaver epidermis pierced by an array of polymer microneedles and subsequently exposed to Trypan blue dye. (B) Microneedles pierced across human cadaver epidermis and imaged *in situ* by SEM. Microneedles remained intact after insertion. To prepare for imaging, the skin was dehydrated, which caused it to collapse down to the base of the microneedles. (C) SEM image of human cadaver epidermis after microneedles were inserted and removed. The residual holes in skin are evident [44].

2.8.6. Transport studies and Transdermal diffusion

McAllister *et al.*, 2003, determined the rates of transdermal transport by piercing human cadaver epidermis with microneedles. Epidermis was isolated by incubating in 60°C water for 2 min and gently removing epidermis. Because the primary barrier to transdermal transport is the stratum corneum (the upper 10–15 μm of the epidermis), the use of epidermis rather than full-thickness skin is a well-established model for transdermal drug delivery [61]. Although, removing the diffusional barrier of dermis may overestimate the skin permeability by up to a factor of 2 for above microneedles, using full-thickness skin could underestimate permeability by a factor of 5 because of the presence of excess dermis. Epidermis mounted in Franz diffusion chambers at 37°C was bathed in the receiver compartment (lower, viable epidermis side) with PBS and in the donor compartment (upper, stratum corneum side) with 1mM calcein, 100 units/ml insulin (Humulin-R), 80 μM Texas red-labeled BSA (Molecular Probes), or polystyrene latex nanospheres at concentrations of 2.5×10^{14} nanospheres per ml (25-nm radius) and

2.4×10^{13} nanospheres per ml (50-nm radius). To prevent insulin aggregation, 10 mM n-octyl β -D-glucopyranoside was added to donor and receiver solutions when insulin was present [61]. Skin permeability was determined by measuring solute concentrations in the receiver compartment over time by calibrated spectrofluorometer (calcein, BSA, and nanospheres) or RIA (insulin). Epidermis samples with arrays of microneedles either inserted or inserted and then removed were chemically fixed with formalin and then freeze dried after dehydration using graded ethanol substitution. Gold-coated samples were examined by scanning electron microscopy. Figure 2.44 illustrates the result of this experiment.

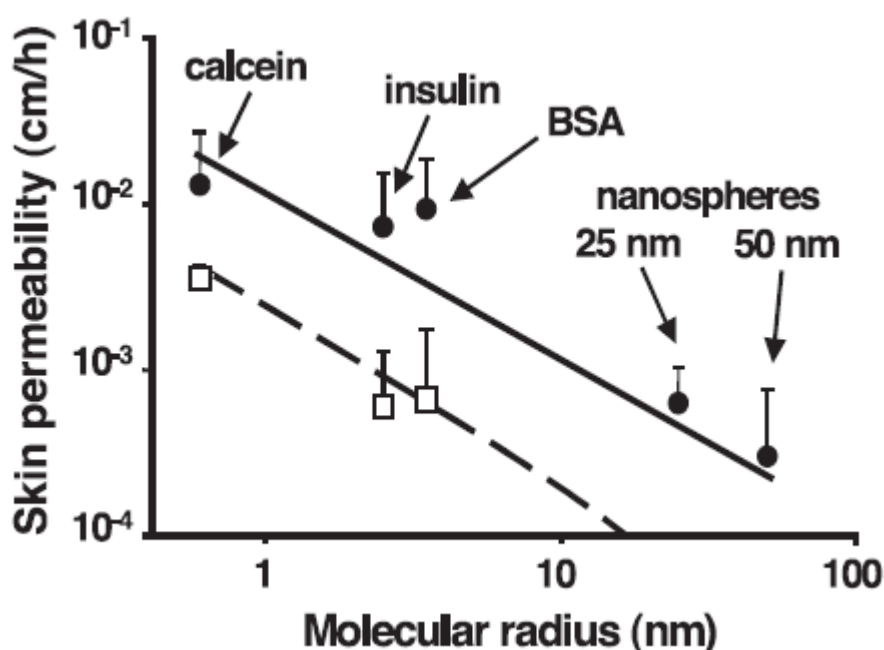


Figure 2.44: Skin permeability to molecules and particles of different sizes after treatment with microneedles. The permeability of human cadaver epidermis was increased by orders of magnitude with a 400-needle array inserted (box) and after the array was removed (dot) for calcein, insulin, BSA, and latex nanospheres of 25 nm and 50 nm radius. Permeability to nanospheres with needles inserted was below the detection limit, on the order of 10^{-4} cm/h. In the absence of microneedles, permeability to all compounds was below their detection limits, on the order of 10^{-6} to 10^{-4} cm/h. Mean values \pm SD are shown for at least six replicates. Predictions are shown for needles inserted (dashed line) and needles removed (solid line) by using a model requiring no adjustable parameters. Model predictions are within the 95% confidence interval of each experimental data point, which supports the interpretation that transport occurred by diffusion through water-filled holes across the skin [61].

2.8.7. Stability of vaccine

Delivery of vaccines is more difficult than the delivery of other types of drugs because of the stability challenges [39]. For transdermal vaccine delivery, preservation of protein integrity is important because a change in protein structure can lead to impaired vaccination efficacy and an altered immune response [39]. So far, only a few limited studies have been performed on

the stability of therapeutic proteins, delivered transdermally by microneedles. Different approaches of drug delivery by microneedles may induce different types of protein degradation, as summarized in Table 2.4 [39].

Table 2.4

Hypotheses of microneedle induced protein degradation mechanisms, which may occur during protein delivery by microneedles [39]

Stress factor	Type of degradation	Type of microneedles	Factors involved
Interface induced	Aggregation Adsorption Unfolding	Hollow microneedles, coated microneedles and drug patch for the “poke and flow” approach	Microneedle bore, applied pressure on microneedle, materials/surface properties, formulation (e.g., presence of a surfactant)
High protein concentration	Aggregation	Coated/dissolving microneedles	Microneedle coating/molding solution
Temperature induced	Aggregation Unfolding Chemical degradation	Dissolving microneedles	Microneedle polymerization/ transition temperature, dissolving microneedle after application
Metal catalyzed	Aggregation Oxidation	Hollow and solid metal microneedles	Formulation impurities
Air exposure	Aggregation Adsorption Oxidation Unfolding	Coated/dissolving microneedles and drug patch for “poke and flow” approach	Storage conditions of microneedles
pH induced	Aggregation Unfolding Chemical degradation	Coated/dissolving microneedles and drug patch for “poke and flow” approach	Dissolving microneedle after application, pH of coating solution/patch solution/molding solution

Sullivan *et al.*, 2010, assessed the stability of the inactivated influenza vaccine in dissolving PVP microneedles. They identified two steps during the fabrication of PVP microneedles that might cause damage: the initial lyophilization of vaccine and the subsequent encapsulation within microneedles during polymerization [59]. To analyze the individual effects of lyophilization and PVP, they administered inactivated influenza virus intramuscular (IM) in mice as the original vaccine solution (Unproc.); after lyophilization (Lyo.), as the original vaccine solution mixed with PVP (Unproc. + Lyo.) and after lyophilization and encapsulation within PVP microneedles (Lyo. + PVP) (Figure 2.45) [59]. Compared to naive mice, all four vaccinated groups showed elevated influenza-specific IgG titers and hemagglutination inhibition (HAI) titers (Figure 2.45).

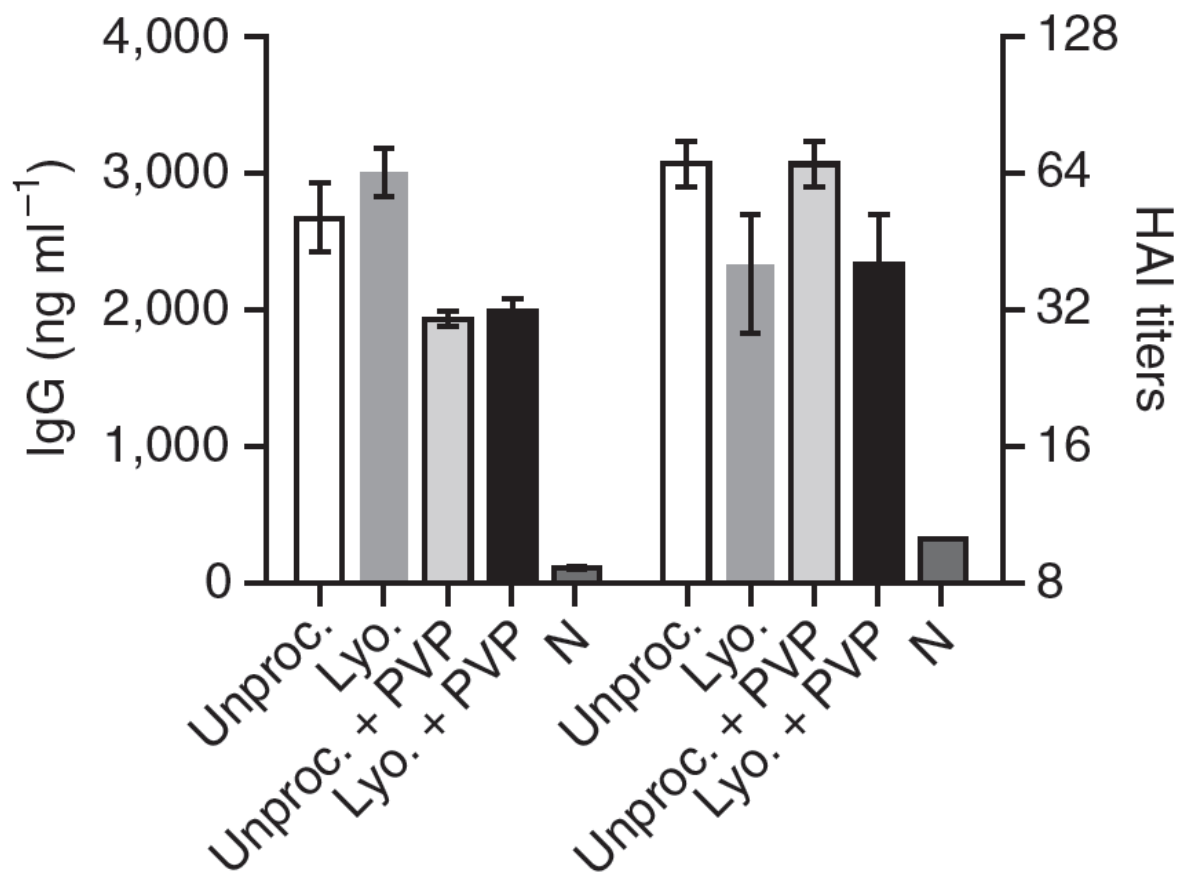


Figure 2.45: Effect of PVP and lyophilization on vaccine immunogenicity. Mice ($n = 3$) were immunized IM with 20 μg inactivated influenza virus (A/PR/8/34) that was either lyophilized or in solution with or without PVP added. Serum IgG antibody titers and HAI were measured 14 d after immunization. Unproc., unprocessed inactivated influenza virus in PBS; Lyo., lyophilized inactivated influenza virus re-dissolved in PBS; Unproc. + PVP, unprocessed inactivated influenza virus in PBS mixed with PVP; Lyo. + PVP, lyophilized inactivated influenza virus encapsulated in PVP; N, naïve mice. Error bars represent SD from three to five independent experiments [59].

2.8.8. Characterization of immune responses

The immune response induced by vaccines delivered by microneedles is dose dependent, and mostly independent of the depth of delivery, density of microneedles, and area of application [50].

a) Humoral immune responses

Sullivan *et al.*, 2010, determined the efficacy of skin immunization with dissolving PVP microneedles BALB/c mice that received a single dose of 6 μg of whole, encapsulated, inactivated influenza virus. The microneedle patches were applied on the caudal dorsal area of skin for approximately 15 min, which was sufficient to dissolve the microneedles and deliver at

least 80% of the antigen into skin [59]. Induction of humoral immune responses after IM immunization, which is the standard influenza vaccination method, was compared with those generated using dissolving microneedles at the same vaccine dose (Figure 2.46a–d).

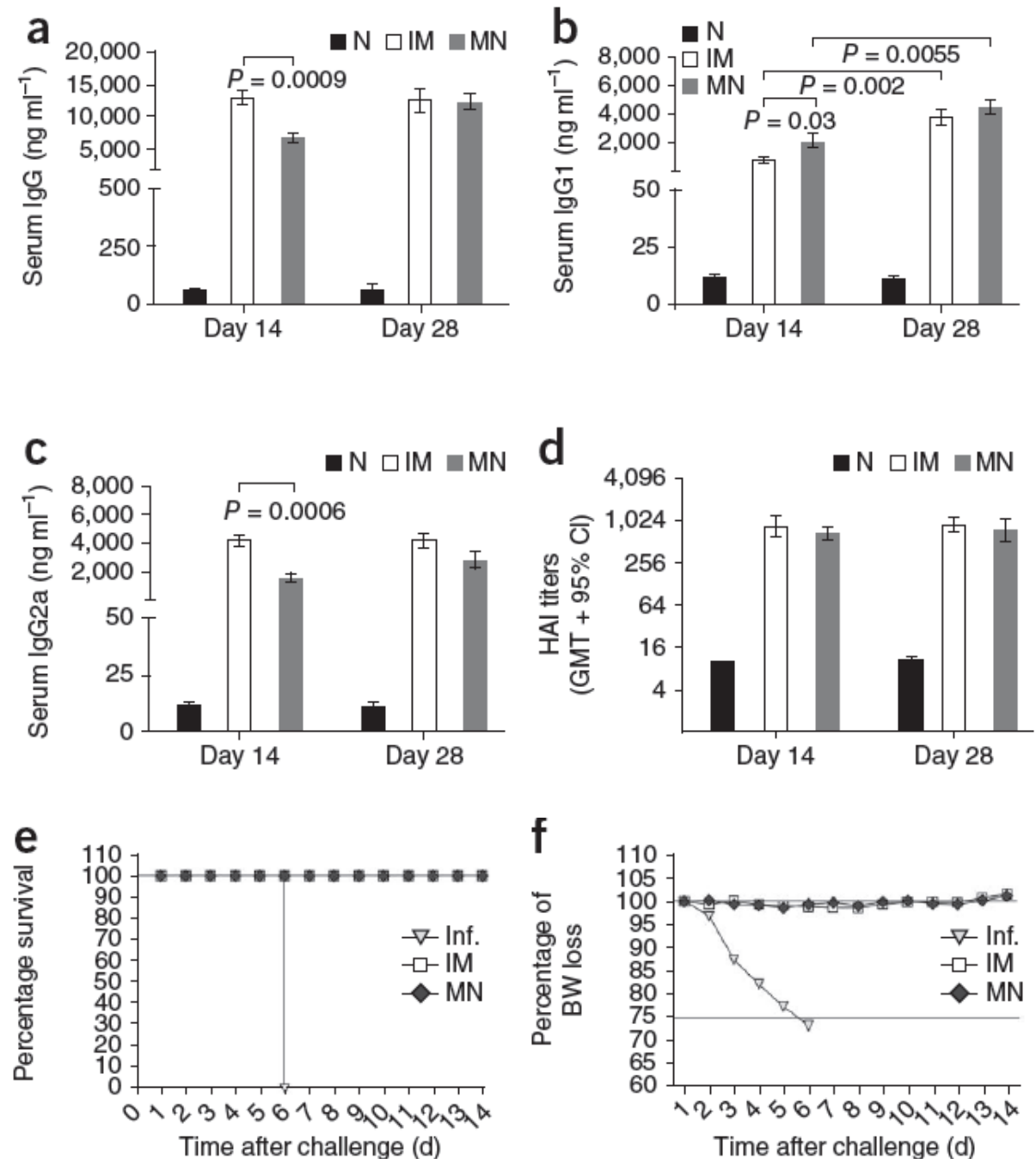


Figure 2.46: Microneedle immunization studies. (a) Serum influenza-specific IgG titers 14 and 28 d after immunization. Mice ($n = 12$) were immunized IM with inactivated influenza virus (A/PR/8/34) or via a microneedle patch encapsulating the same amount of virus. (b) IgG1 titers; (c) IgG2a titers and (d) HAI titers on days 14 and 28. (e) Survival rates of immunized and naive mice upon lethal challenge with five times the LD₅₀ of homologous influenza virus. (f) Percentage of body weight changes upon lethal challenge. N, naïve group; IM, intramuscularly immunized group; MN, microneedle-immunized group; and Inf., unimmunized challenged group [59].

Blood was collected on days 14 and 28 after immunization to determine the concentrations of influenza-specific antibodies. Although, influenza-specific IgG titers, after day 14, was slightly lower in mice immunized with microneedles than that in IM group (Figure 2.46a); the titers were at similar levels for both IM and microneedle groups at day 28. It was also found that, at day 14, microneedle-immunized mice had more pronounced IgG1 titers than the IM group (Figure 2.46b), whereas the IM-immunized mice showed significantly stronger IgG2a responses than the microneedle group (Figure 2.46c). At day 28 there were no significant differences in the isotype levels between the groups. This can be attributed to the fact that the IM group had T helper type 1 (Th1)-biased responses early after immunization (IgG1/IgG2a ratio = 0.2), but levels of these isotypes were similar after 1 month (IgG1/IgG2a = 0.9). In contrast, the microneedle group showed a slight predominance of IgG1 production overtime (IgG1/IgG2a in the range of 1.35 to 1.53) (Figure 2.46b, c). HAI activity is generally used as the serological measure for functional antibodies associated with protection. HAI titers detected in the microneedle group were similar to each other on days 14 and 28 and to IM group titers too (Figure 2.46d), demonstrating that a single microneedle immunization induced high levels of functional antibodies [59].

b) Protection against lethal viral challenge

It is also important to determine whether microneedle immunization can confer protective immunity. To ascertain this, immunized groups of mice were challenged with five times the half-maximal lethal dose (LD₅₀) of mouse-adapted PR8 influenza virus 30 d after vaccination [59]. All immunized animals survived challenge (Figure 2.46e) and lost <5% body weight (Figure 2.46f), showing that vaccine delivery with dissolving microneedles provided protection equal to the IM group. In contrast, the unimmunized group did not survive beyond 6 d after challenge (Figure 2.46f) [59]. These results establish the efficacy of transdermal vaccination using microneedles.

PART III: REPORT ON THE PRESENT INVESTIGATION

Chapter 3: Fabrication of Microneedles

3.1. Desired characteristics of microneedles for vaccine delivery

An efficient microneedle should have a sharp 3D tip to reduce insertion force and a large base to increase fracture force [50]. For robust, painless penetration of human skin, primarily stratum corneum and epidermis, and to target abundant clusters of antigen-presenting cells for vaccine delivery microneedle should be 50-100 μm in length [53]. Microneedles must withstand the bending and buckling forces experienced during penetration of the skin, preferably without breaking. Material of microneedles should be biocompatible for their widespread use and customer acceptance. Vaccine delivery should be a fast and hassle-free procedure, and in this context polymeric dissolving microneedle have bright prospect. Skin damage caused due to penetration by microneedle must be minimal and should be recovered within 2-3 hours [62]. Maintaining the stability of vaccines during microneedle fabrication and/or coating is a huge challenge, but indispensable. Vaccines delivered using microneedles must meet the efficacy and induce humoral immune response to a comparable level, if not better, to that of other modes of delivery, such as, intramuscular, subcutaneous, oral etc.

3.2. Design and Simulation

Simulation was carried out on IntelliSuite v8.7, using IntelliFab module to optimize process parameters of different fabrication approaches and to confirm the feasibility of the process before continuing with actual fabrication.

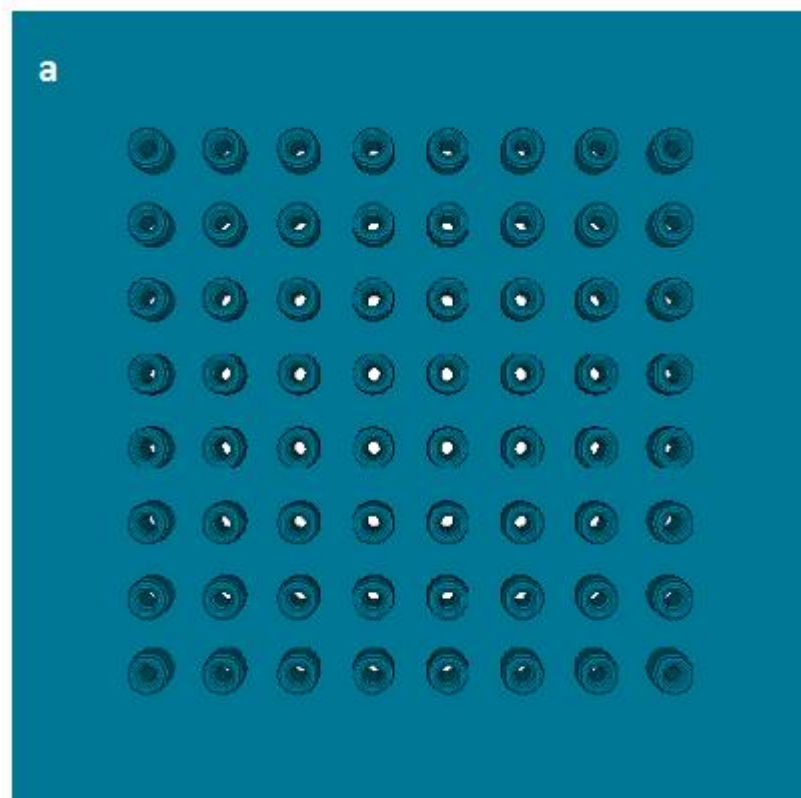
3.2.1. Hollow Cylindrical Silicon Microneedles

Hollow silicon microneedles array of cylindrical shape, having height of 60 μm , suitable for transdermal vaccine delivery targeted to the APC-rich epidermis layer of skin, was designed and their fabrication process was simulated. Table 3.1 illustrates the fabrication process sequence used in simulation and Figure 3.1 illustrates the result of the simulation.

Table 3.1

Process sequence used in the simulation of hollow cylindrical silicon microneedle array fabrication

#	Type	Material	Process	Process ID	Process Option
1	Definition	Si	Czochralski	100	
2	Etch	Si	Clean	RCA	Partial Etching
3	Deposition	SiO ₂	Thermal	Wet	Conformal Deposition
4	Deposition	PR-System8	Spin	810	Conformal Deposition
5	Exposure	UV	Contact	Suss	
6	Etch	SiO ₂	Wet	BOE	Partial Etching
7	Etch	Si	RIE	Cl ₂ _CF ₄	Partial Etching
8	Etch	PR-System-8	Plasma	O ₂	Sacrifice
9	Deposition	PR-S1800	Spin	S1805	Conformal Deposition
10	Exposure	UV	Contact	Suss	
11	Etch	Si	Plasma	SF ₆	Etch Through
12	Etch	PR-S1800	Wet	1112A	Sacrifice
13	Etch	Si	RIE	Cl ₂ _CF ₄	Partial Etching
14	Deposition	PR-System8	Spin	810	Conformal Deposition
15	Exposure	UV	Contact	Suss	
16	Etch	Si	RIE	Cl ₂ _CF ₄	Partial Etching
17	Etch	PR-System-8	Plasma	O ₂	Sacrifice
18	Etch	Si	Clean	Piranha	Partial Etching
19	Etch	SiO ₂	Wet	BOE	Partial Etching



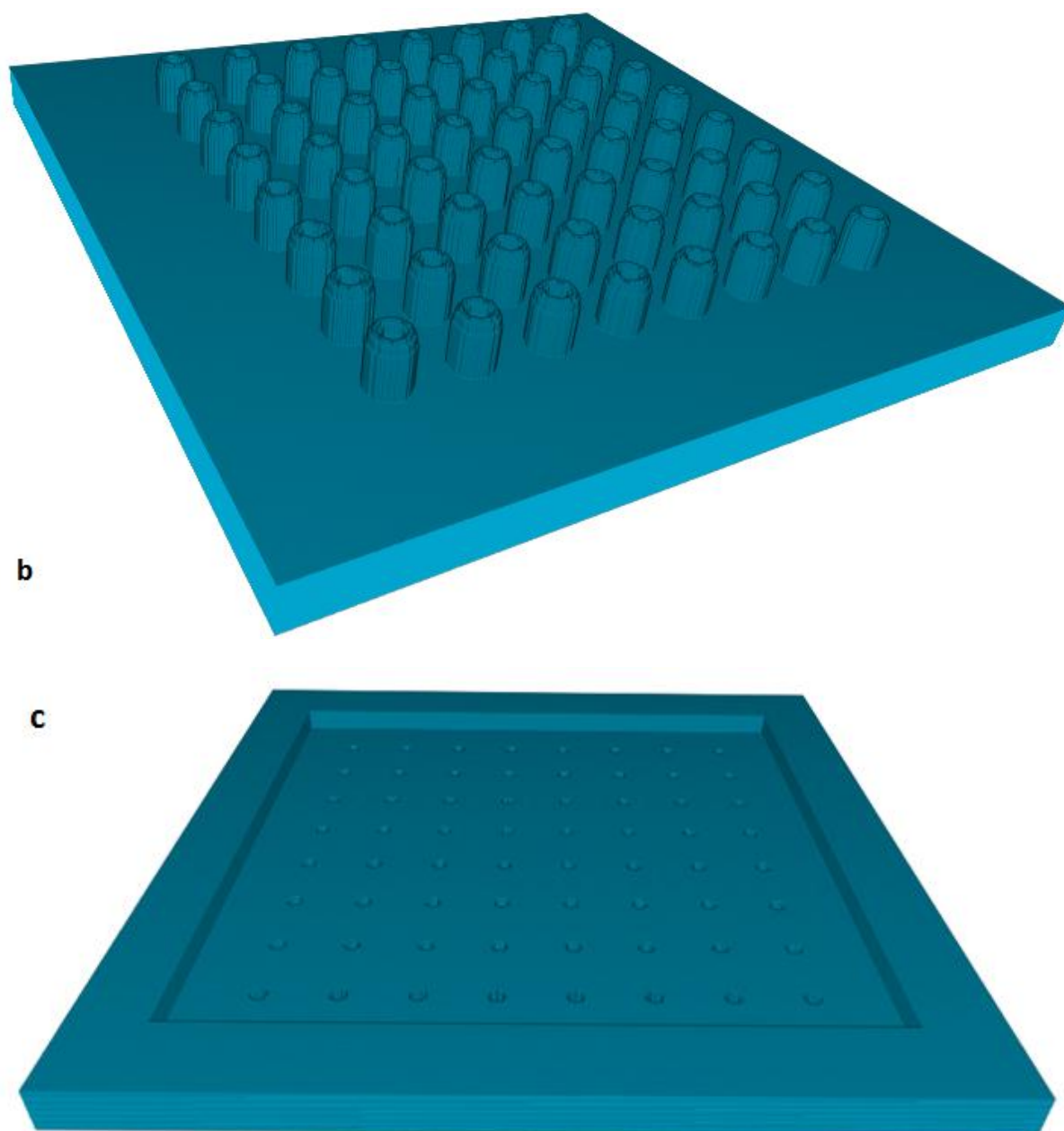


Figure 3.1: Simulation of hollow cylindrical silicon microneedle array with backside reservoir, (a) top view, (b) tilted top view and (c) back side of microneedle array showing the reservoir for fluidic vaccine.

3.2.2. 3D sharp-tip Hollow Silicon Microneedles

Hollow silicon microneedles, having 3D sharp tip and 200 μm height, were designed and their fabrication process was simulated. Table 3.2 illustrates the fabrication process sequence (as described by Zhang *et al.*, 2009) used in simulation, Figure 3.2 shows the mask layout and Figure 3.3 shows the results of simulation of such microneedle array.

Table 3.2

Process sequence used in the simulation of 3D sharp tip hollow cylindrical silicon microneedle array fabrication using bi-mask technique [45]

#	Type	Material	Process	Process ID	Process Option
1	Definition	Si	Czochralski	100	
2	Deposition	SiO ₂	Thermal	Wet	Conformal Deposition
3	Deposition	PR-AZ5214	Spin	001	Conformal Deposition
4	Exposure	UV	Contact	Suss	
5	Etch	SiO ₂	RIE	CHF ₃ _CF ₄	Partial Etching
6	Etch	Si	RIE	Cl ₂ _CF ₄	Partial Etching
7	Deposition	PR-AZ5214	Spin	001	Conformal Deposition
8	Exposure	UV	Contact	Suss	
9	Etch	SiO ₂	Wet	BOE	Etch Through
10	Etch	Si	DRIE	SF ₆ _C ₄ F ₈	Partial Etching
11	Etch	PR-AZ5214	Wet	1112A	Etch Through
12	Deposition	PR-AZ5214	Spin	001	Conformal Deposition
13	Exposure	UV	Contact	Suss	
14	Etch	SiO ₂	RIE	CHF ₃ _CF ₄	Partial Etching
15	Etch	Si	DRIE	SF ₆ _C ₄ F ₈	Partial Etching
16	Etch	PR-AZ5214	Wet	1112A	Etch Through
17	Deposition	PR-AZ5214	Spin	001	Conformal Deposition
18	Exposure	UV	Contact	Suss	
19	Etch	SiO ₂	RIE	CHF ₃ _CF ₄	Partial Etching
20	Etch	PR-AZ5214	Wet	1112A	Etch Through
21	Etch	Si	RIE	Cl ₂ _CF ₄	Partial Etching
22	Etch	SiO ₂	Wet	BOE	Sacrifice

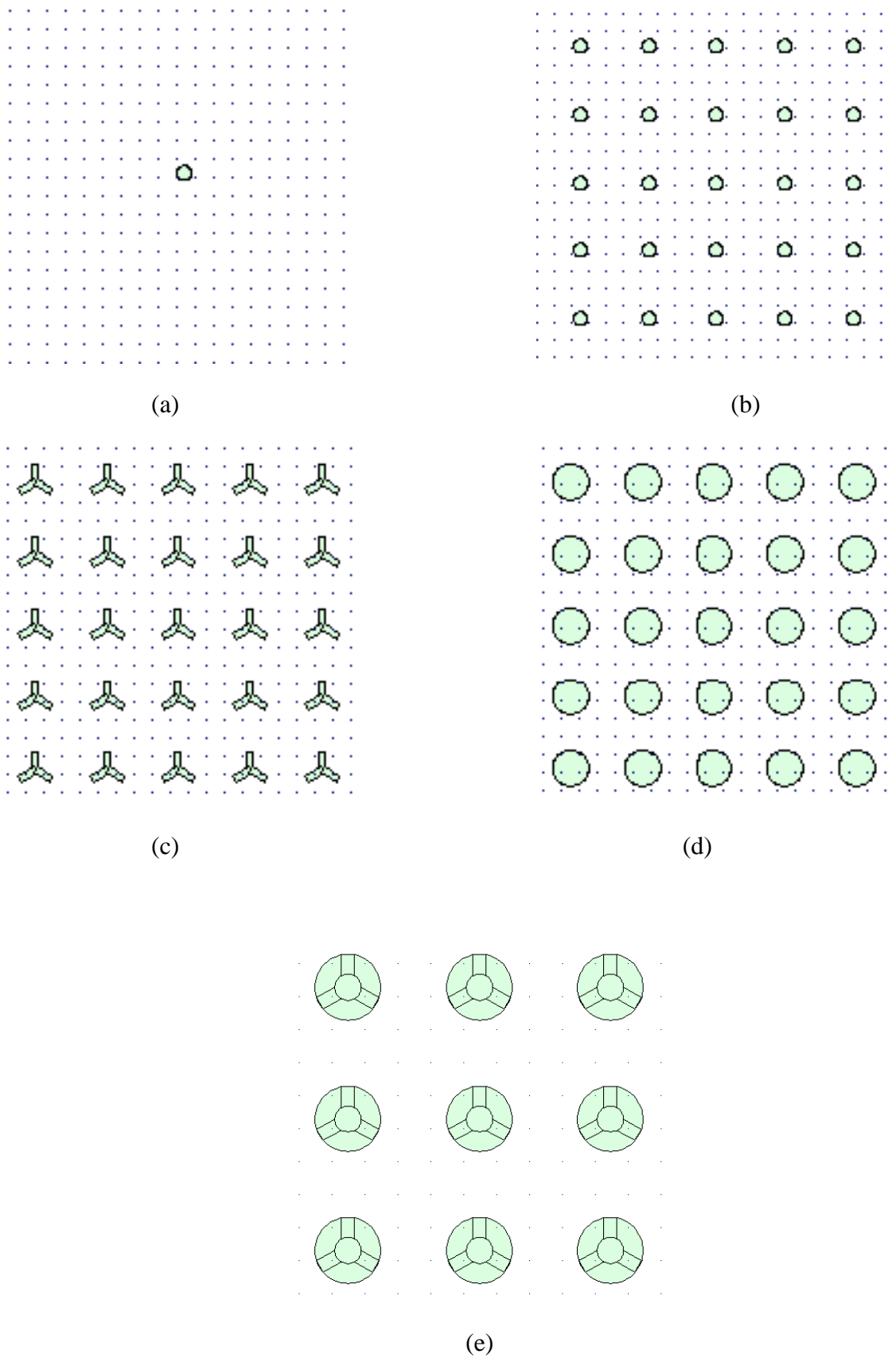
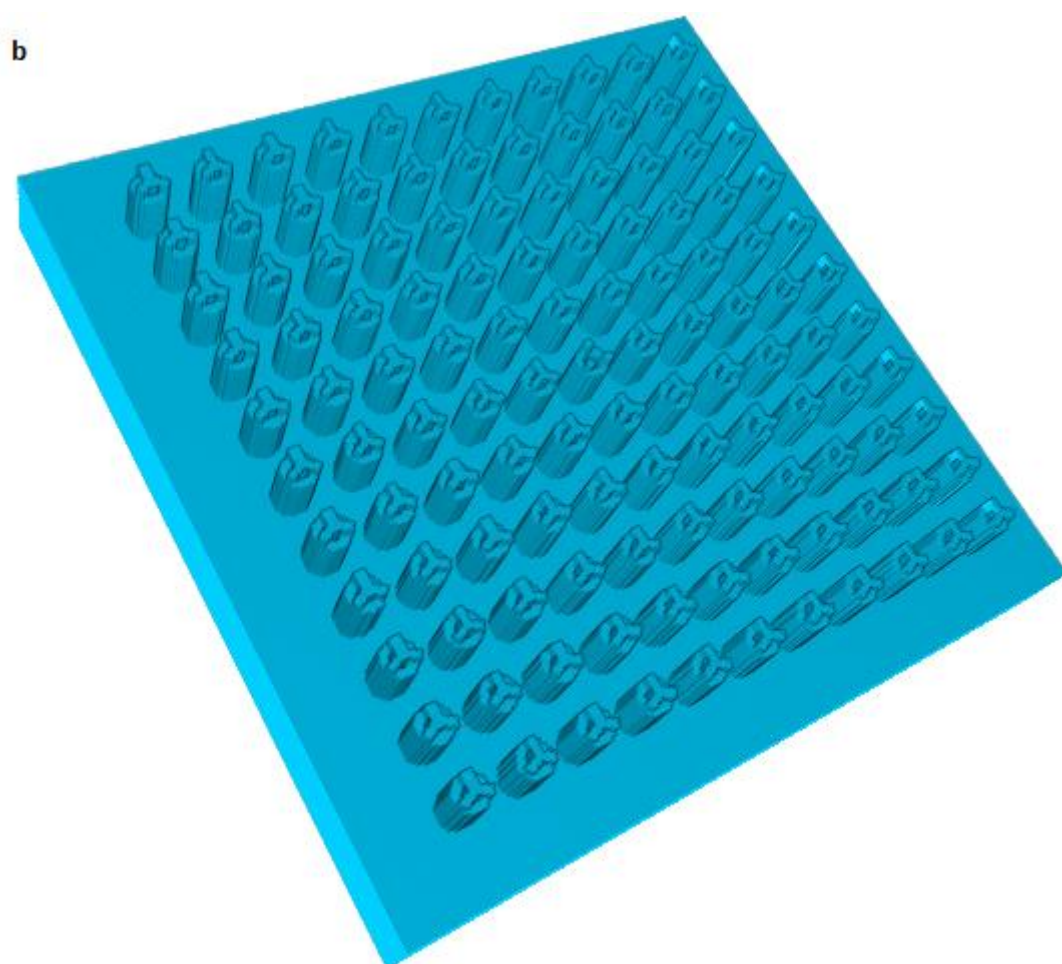


Figure 3.2: Mask layout, (a) layer 0 (b) layer 1 (c) layer 2 (d) layer 3 (e) all layers superimposed.



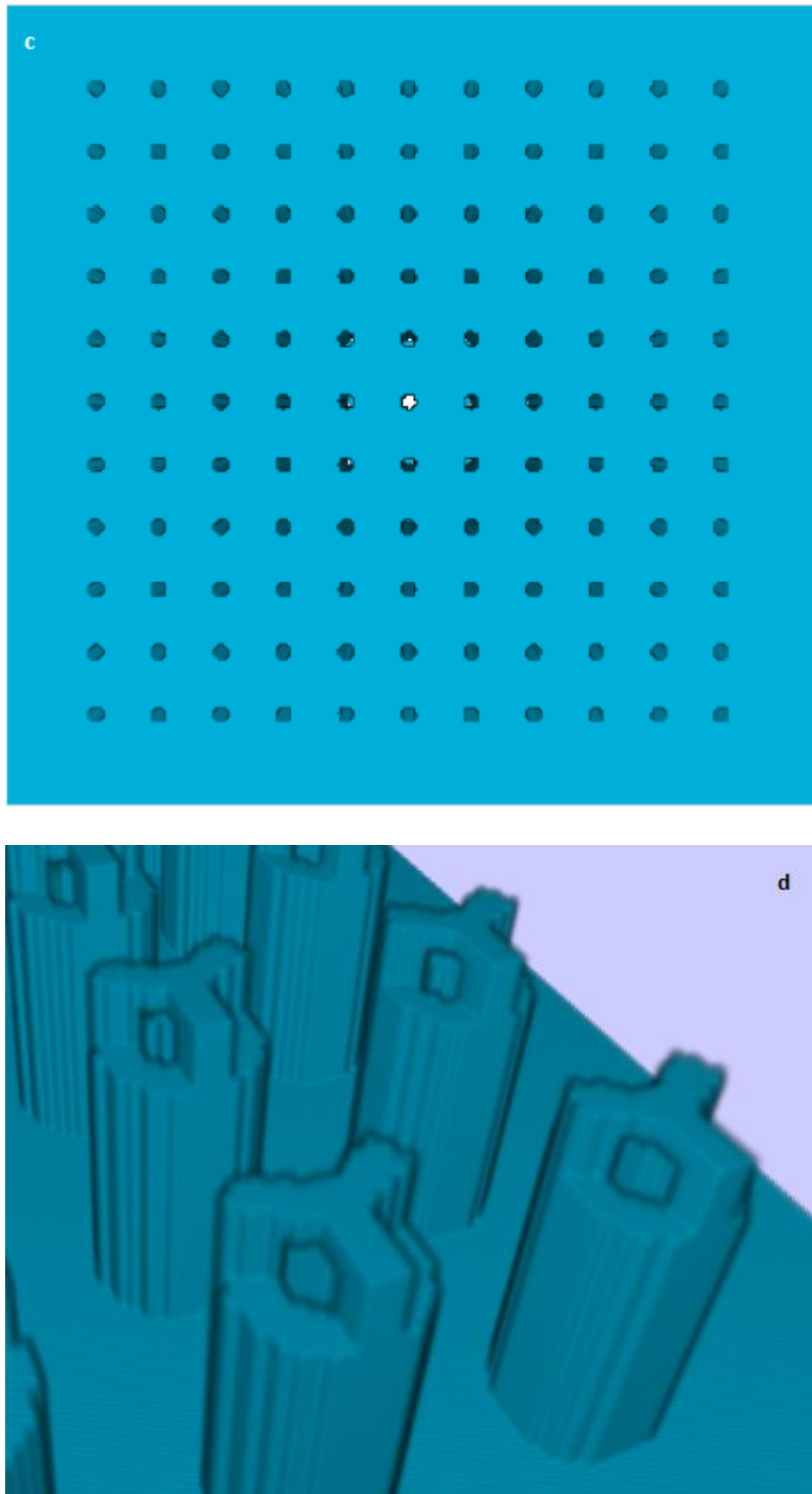


Figure 3.3: Simulation of hollow silicon microneedle array with 3D tip, (a) side view, (b) tilted top view, (c) bottom view and (d) structure of the microneedle tip.

3.2.3. Tapered-tip Solid Silicon Microneedles

Tapered-tip solid silicon microneedle array fabrication was simulated in using IntelliFab. The simulation results in sharp tip dense array of microneedles having height of 70 μm , which can be efficiently used for transdermal delivery of coated vaccines.

Table 3.3

Process sequence used in the simulation of tapered-tip solid silicon microneedle array fabrication

#	Type	Material	Process	Process ID	Process Option
1	Definition	Si	Czochralski	100	
2	Etch	Si	Clean	RCA	Partial Etching
3	Deposition	SiO ₂	Thermal	Wet	Conformal Deposition
4	Deposition	PR-S1800	Spin	S1805	Conformal Deposition
5	Exposure	UV	Contact	Suss	
6	Etch	SiO ₂	RIE	CHF ₃ _CF ₄	Partial Etching
7	Etch	PR-S1800	Wet	1165	Partial Etching
8	Etch	Si	Wet	TMAH	Partial Etching

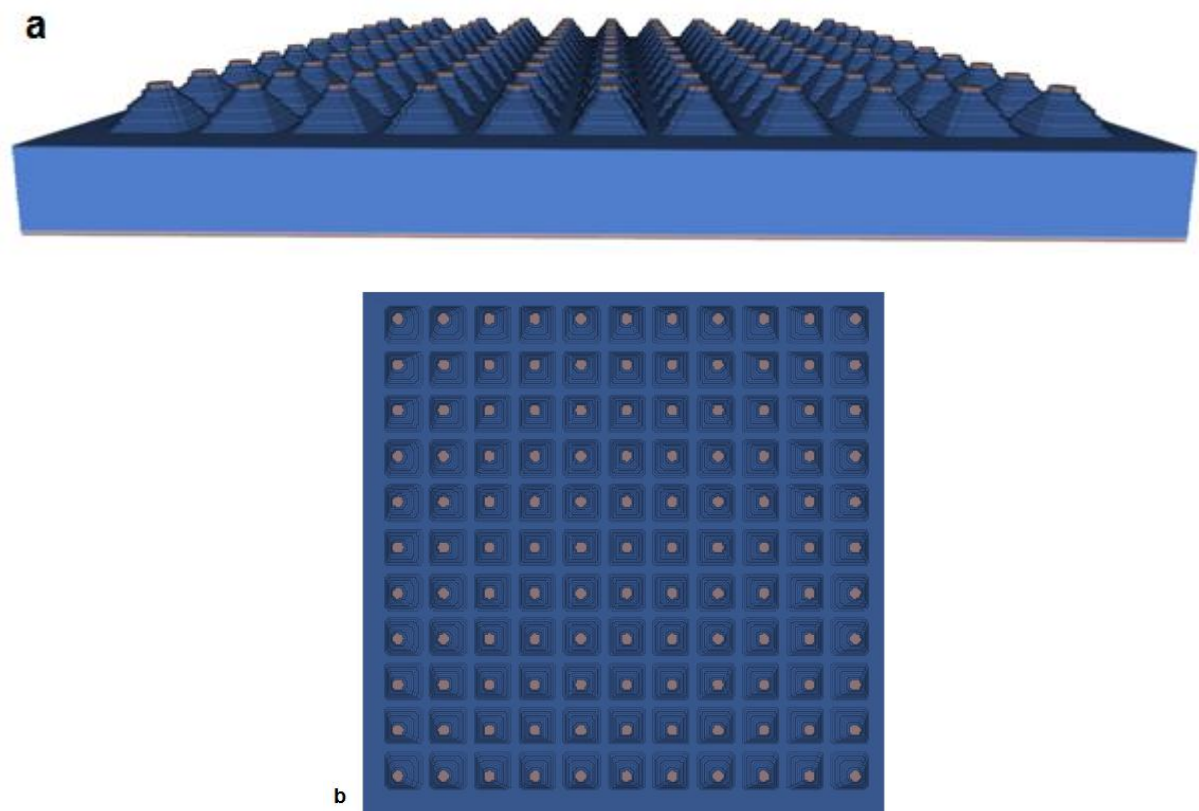


Figure 3.4: Simulation of tapered-tip solid silicon microneedle array, (a) tilted side view, (b) top view.

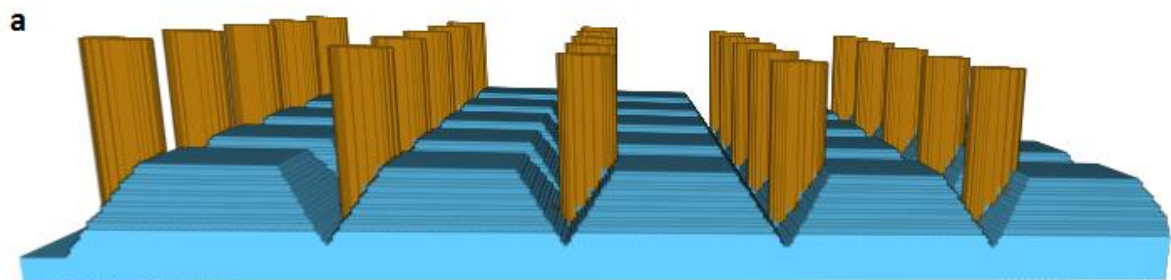
3.2.4. Chisel-tip Hollow SU-8 Microneedles

Fabrication of chisel-tip hollow SU-8 microneedle array with sharp tip was simulated. Microneedles were of 200 μm height, cylindrical with central lumen, efficient for transdermal delivery of fluidic drug and vaccine. These types of microneedles are totally biocompatible and bio-degradable [42]. Table 3.4 represents the process sequence used to fabricate such structures during simulation and Figure 3.5 shows the results of simulation.

Table 3.4

Process sequence used in the simulation of chisel-tip hollow microneedles fabrication

#	Type	Material	Process	Process ID	Process Option
1	Definition	Si	Czochralski	100	
2	Deposition	SiO ₂	Thermal	Wet	Conformal Deposition
3	Deposition	PR-S1800	Spin	S1805	Conformal Deposition
4	Exposure	UV	Contact	Suss	
5	Etch	SiO ₂	RIE	CHF ₃ _CF ₄	Partial Etching
6	Etch	Si	Wet	TMAH	Partial Etching
7	Etch	SiO ₂	Wet	BOE	Sacrifice
8	Etch	PR-S1800	Wet	1165	Sacrifice
9	Deposition	SiO ₂	Thermal	Wet	Conformal Deposition
10	Deposition	PR-AZ5214	Spin	001	Planarization
11	Exposure	UV	Contact	Suss	
12	Etch	SiO ₂	Wet	BOE	Sacrifice



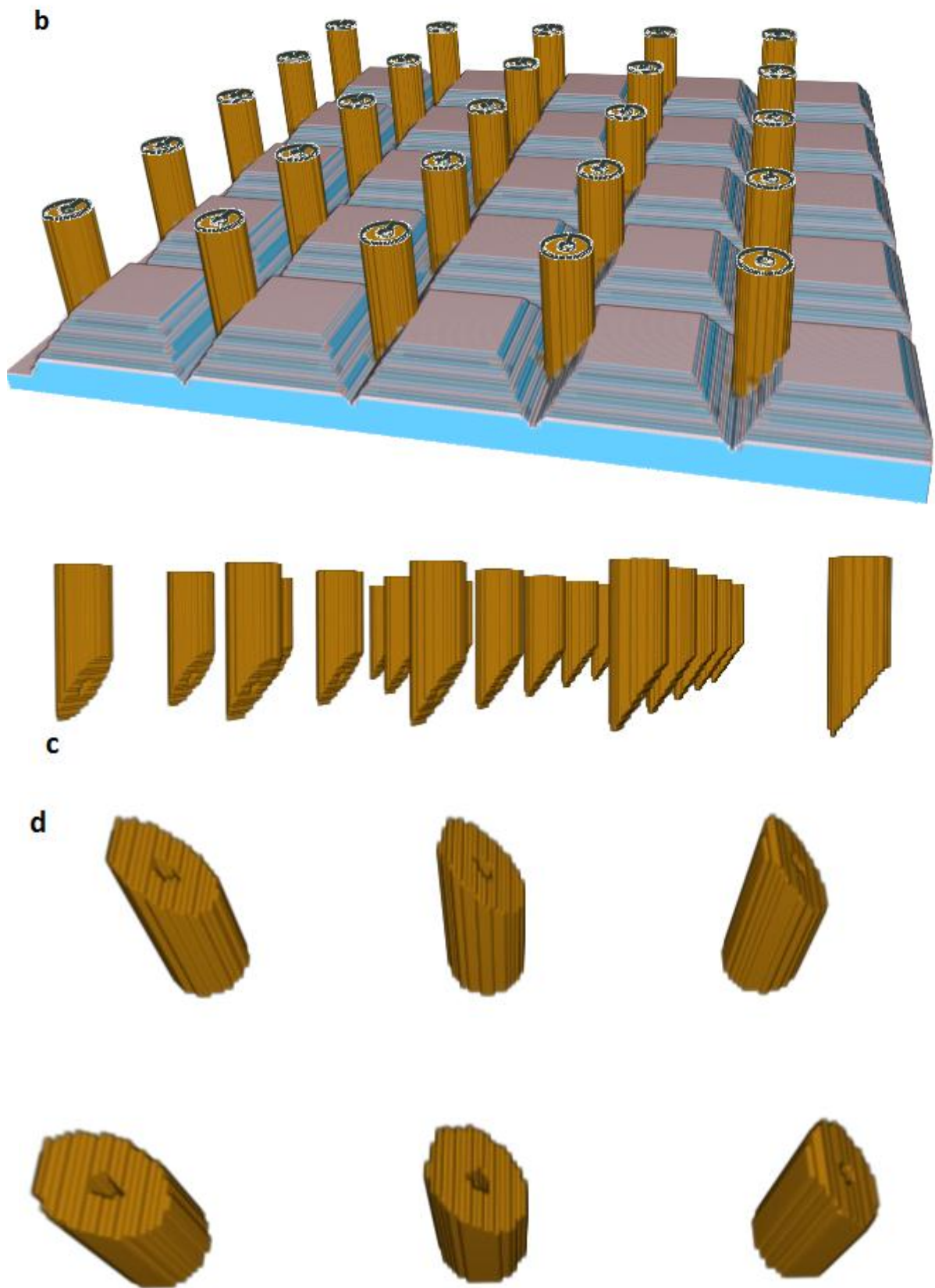


Figure 3.5: Simulation of chisel-tip hollow SU-8 microneedles, (a) tilted side view, (b) tilted side view showing the sacrificial oxide layer coating, (c) side view showing the sharp tip of SU-8 microneedles and (d) tilted top view showing the central microchannel in each microneedle.

3.2.5. In-plane Sharp-tip Silicon Microneedle

Fabrication method followed by Paik *et al.*, 2004, in making in-plane hollow silicon microneedle array was adopted for simulation and feasibility study [58]. Table 3.5 and Figure 3.6 illustrate the fabrication process sequence and its result obtained from simulation.

Table 3.5

Process sequence used in the simulation of in-plane sharp-tip silicon microneedle array fabrication

#	Type	Material	Process	Process ID	Process Option
1	Definition	Si	Czochralski	100	
2	Etch	Si	Clean	RCA	Partial Etching
3	Deposition	SiO ₂	PECVD	N ₂ O	Conformal Deposition
4	Deposition	PR-S1800	Spin	S1805	Conformal Deposition
5	Exposure	UV	Contact	Suss	
6	Etch	SiO ₂	Wet	BOE	Partial Etching
7	Etch	PR-S1800	Wet	Lift-off	Partial Etching
8	Etch	Si	DRIE	SF ₆ _C ₄ F ₈	Partial Etching
9	Deposition	Si ₃ N ₄	LPCVD	SiH ₂ Cl ₂	Conformal Deposition
10	Etch	Si ₃ N ₄	RIE	CHF ₃ _O ₂	Partial Etching
11	Etch	Si	Plasma	SF ₆	Partial Etching
12	Etch	Si ₃ N ₄	Wet	H ₃ PO ₄	Etch Through
13	Deposition	PR-S1800	Spin	S1805	Planarization
14	Exposure	UV	Contact	Suss	
15	Deposition	PR-S1800	Spin	S1805	Conformal Deposition
16	Exposure	UV	Contact	Suss	
17	Etch	SiO ₂	RIE	CHF ₃ _CF ₄	Etch Through
18	Etch	Si	Wet	KOH	Partial Etching
19	Etch	PR-S1800	Wet	1112A	Etch Through
20	Etch	SiO ₂	RIE	CHF ₃ _CF ₄	Partial Etching
21	Etch	PR-S1800	Wet	1112A	Etch Through
22	Etch	Si	DRIE	SF ₆ _C ₄ F ₈	Partial Etching
23	Deposition	SiO ₂	PECVD	N ₂ O	Conformal Deposition
24	Deposition	PR-S1800	Spin	S1805	Conformal Deposition
25	Exposure	UV	Contact	Suss	
26	Etch	SiO ₂	RIE	CHF ₃ _CF ₄	Etch Through
27	Etch	Si	DRIE	SF ₆ _C ₄ F ₈	Etch Through
28	Etch	PR-S1800	Wet	1112A	Etch Through
29	Etch	SiO ₂	RIE	CHF ₃ _CF ₄	Etch Through

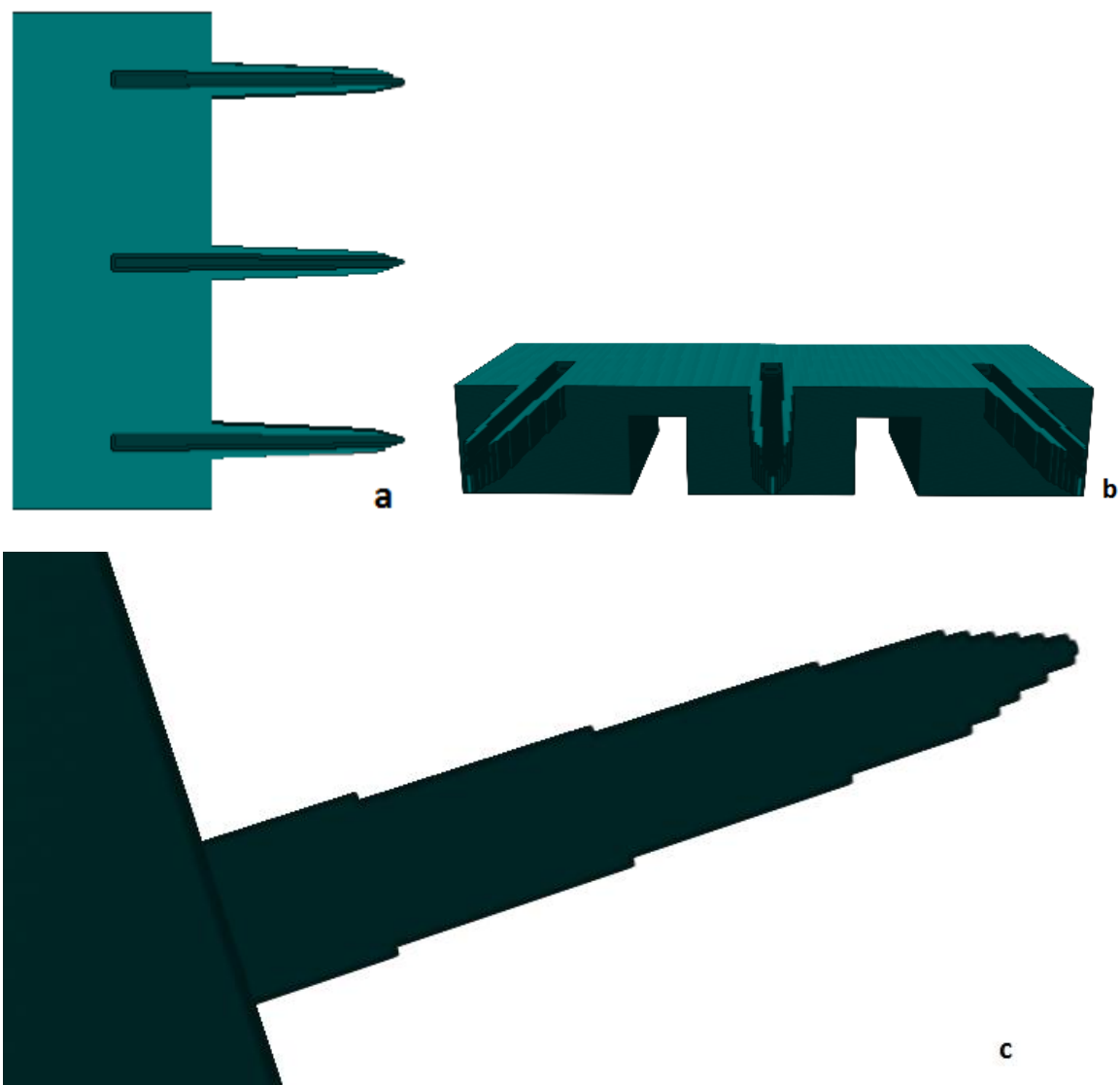


Figure 3.6: Simulation of in-plane sharp-tip silicon microneedle array, (a) top view, (b) front side view and (c) microneedle tip structure.

3.3. Fabrication methodologies

The microneedle array fabrication processes were simulated using the IntelliSuite package to confirm the feasibility of the process before continuing with actual fabrication.

3.3.1. Fabrication of Hollow Cylindrical Silicon Microneedle Array

Fabrication process started with RCA cleaning of a p-type single-crystal <100> silicon wafer of 2" diameter, having thickness of 275 μm and resistivity of 4-7 ohm-cm. A wet oxide layer of thickness 1000 nm was deposited on both sides of the wafer using pyrogenic thermal oxidation furnace. A 20 μm thick layer of SU-8 2100 was spin-coated onto the wafer and exposed using a dark field mask as shown in Figure 3.7 to transfer the patterns on underlying SiO_2 layer. SU-8 in the exposed areas was crosslinked during development and post-bake giving 20 μm tall cylindrical structures. Oxide from the exposed areas (not covered by SU-8) was etched off using buffered oxide etchant (BOE). Then, reactive ion etching (RIE) was carried out to etch silicon and produce hollow cylindrical microneedle array, using STS-RIE 320 PC system. Profilometry (XP2) was carried out to determine the feature heights. Scanning electron micrographs were recorded using a Zeiss SEM. Table 3.6 lists all the parameters of different processes used in this fabrication. The fabricated microneedle should schematically look like Figure 3.8.

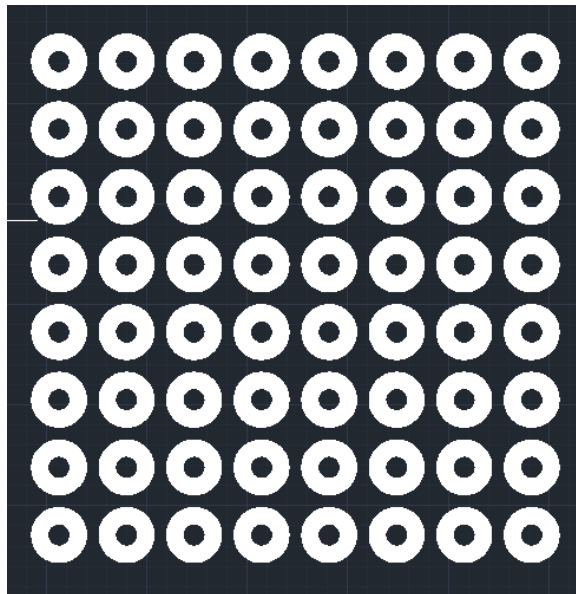


Figure 3.7: Layout of 8 x 8 mask (dark-field) for pattern transfer onto SiO_2 . Diameter of inner lumen and the outer circle is 70 μm and 165 μm , respectively. Center-to-center distance is 210 μm .

Table 3.6

Process parameters for fabrication of hollow cylindrical silicon microneedle array

RCA	Organic Clean: 5:1:1 H ₂ O:H ₂ O ₂ :NH ₄ OH solution (80 °C); 15 min. Bubble Rinse (DI) 5 min. Oxide Strip: 20:1 H ₂ O: HF solution (80 °C); 30 sec. Rinse < 30 sec. Ionic Clean: 6:1:1 H ₂ O:H ₂ O ₂ : HCl solution; 15 min. Rinse 5 min. N ₂ drying.
Oxidation	Wet, field pyrogenic oxidation, H ₂ and O ₂ , 1050 °C
Spinning SU-8 2100	Dehydration: 120 °C for 5 min. Spinning: 300 rpm for 15 sec, then 3000 rpm for 30 sec.
Soft bake	65 °C for 15 min, ramp up to 90 °C with 5 °C step, 90 °C for 30 min
Relaxation	Ramp down to RT, 2 hrs.
Exposure	Dose = 230 J/cm ² , Power = 500 W, Wavelength = 436 nm, Exposure time = 25 sec
Development	Developer: PGMEA (Propylene Glycol Methyl Ether Acetate)
Post bake	65 °C for 15 min, ramp up to 90 °C with 5 °C step, 90 °C for 30 min
Relaxation	Ramp down to RT, 2 hrs.
Oxide etch	Etchant: BOE (5:1 NH ₄ F: HF (49%)), Etch rate = 2 nm/sec, Etch time = 10 min.
RIE (Si)	CF ₄ = 40 sccm, SF ₆ = 40 sccm, O ₂ = 5 sccm, Pressure = 100 mTorr, Power = 100 W, Load position = 31 %, Tune position = 10 %, APC angle = 90 °, Etch rate = ~1.5 µm/min Etch time = 40 min

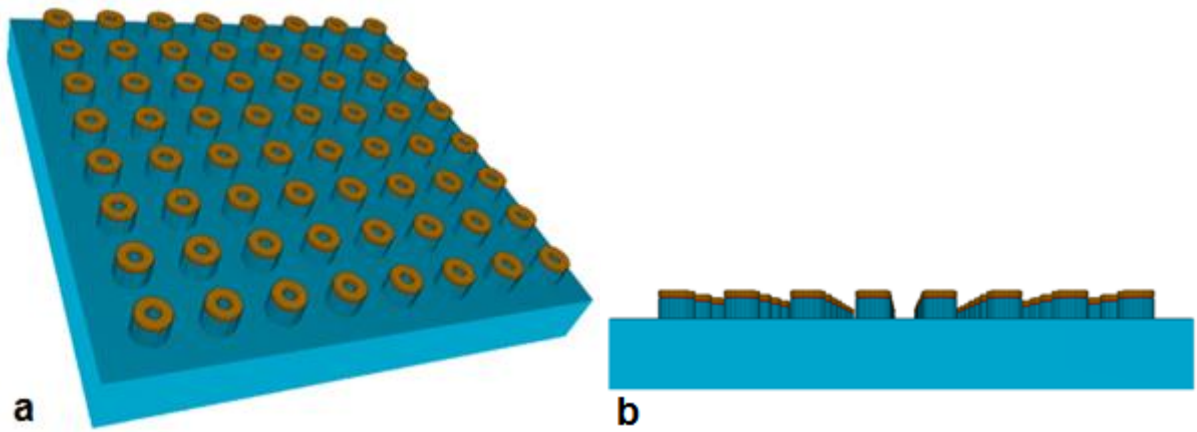


Figure 3.8: Schematic representation of fabricated hollow cylindrical silicon microneedle array (8x8)

(a) tilted top view and (b) side view.

3.3.2. Fabrication of Tapered-tip Solid Silicon Microneedle Array

Single-crystal silicon wafer having diameter of 51 mm and thickness of 275 μm with $\langle 100 \rangle$ orientation was cleaned by RCA process. A wet oxidation process was followed to coat the wafer with 1000 nm thick SiO_2 . An 8 μm thick positive photoresist, S1805 layer was spun onto the oxide layer and exposed using a bright-field mask, shown as in Figure 3.9 to transfer the pattern on the oxide layer. SiO_2 was removed from the exposed areas using reactive ion etching (STS-RIE) and CHF_3/CF_4 chemistry. Then silicon was etched anisotropically using 25% TMAH etchant to achieve sharp-tip pyramidal shape solid silicon microneedles. Profilometry (XP2) was carried out to determine the feature heights. Table 3.7 lists all the parameters of different processes used in this fabrication. The fabricated microneedle should schematically look like Figure 3.10.

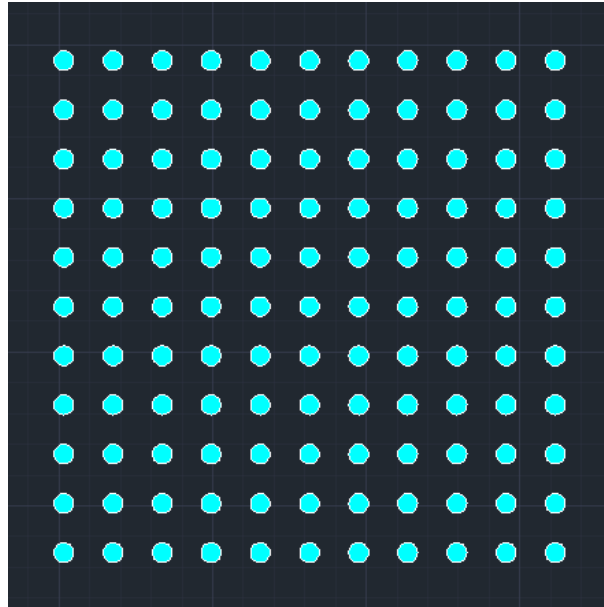


Figure 3.9: Mask layout (bright-field) for pattern transfer onto SiO₂

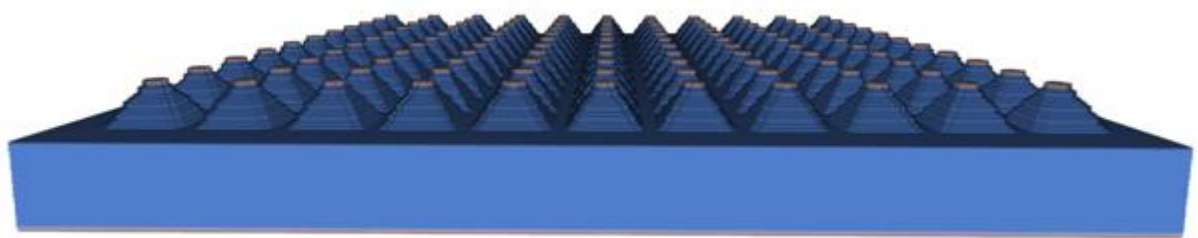


Figure 3.10: Schematic representation of fabricated tapered-tip solid silicon microneedle array (11x11) (side view)

Table 3.7

Process parameters for fabrication of tapered-tip solid silicon microneedle array

RCA	Organic Clean: 5:1:1 H ₂ O:H ₂ O ₂ :NH ₄ OH solution (80 °C); 15 min. Bubble Rinse (DI) 5 min. Oxide Strip: 20:1 H ₂ O: HF solution (80 °C); 30 sec. Rinse < 30 sec. Ionic Clean: 6:1:1 H ₂ O:H ₂ O ₂ : HCl solution; 15 min. Rinse 5 min. N ₂ drying.
Oxidation	Wet, field pyrogenic oxidation, H ₂ and O ₂ , 1050 °C
Spinning	Dehydration: 120 °C for 5 min.

S-1805	Spinning: 300 rpm for 15 sec, then 3000 rpm for 30 sec.
Soft bake	65 °C for 15 min
Exposure	Dose = 230 J/cm ² , Power = 500 W, Wavelength = 436 nm, Exposure time = 25 sec
Development	Developer: PGMEA (Propylene Glycol Methyl Ether Acetate)
Oxide etch (RIE)	i) CF ₄ = 90 sccm, CHF ₃ = 30 sccm (ER = 0.5 nm/min) ii) CF ₄ = 25 sccm, O ₂ = 3.1 sccm (ER = 27.5 nm/min) Pressure = 100 mTorr, Power = 100 W, Load position = 31 %, Tune position = 10 %, APC angle = 90 °, Etch depth = 1000 nm, Etch time = ~40 min using (ii)
Si etch	Etchant: TMAH, Concentration: 25%, Temperature: 90 °C, Etch rate = 50 µm/hr. Etch depth = 100/1.414 = 70 µm (see Figure 3.11)

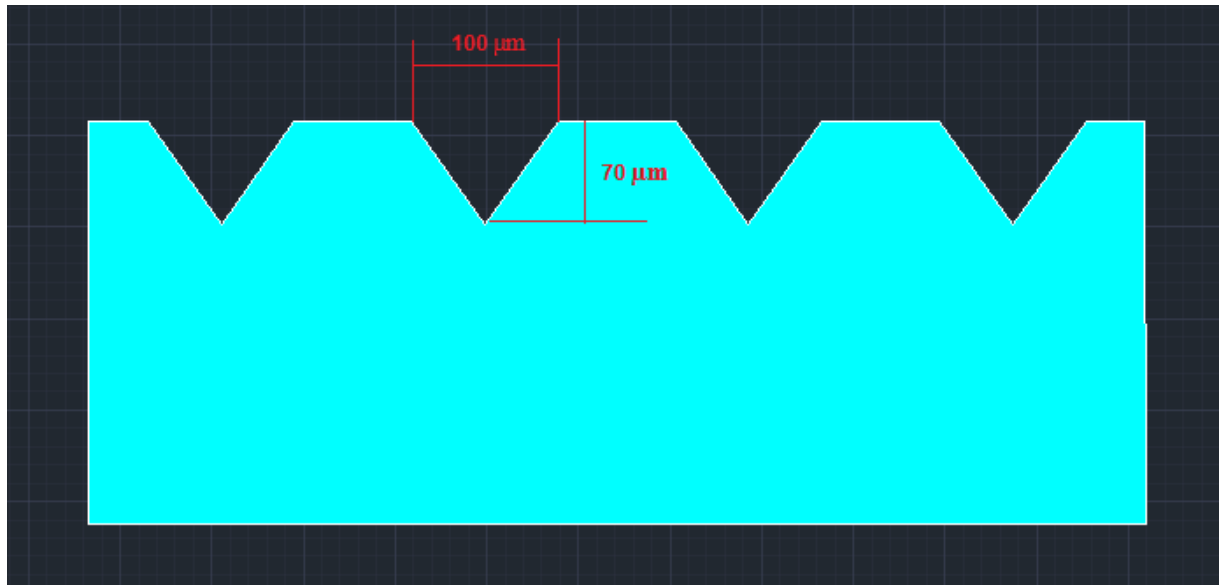


Figure 3.11: Silicon etch-depth calculation. Mask feature diameter is 40 µm. Center to center distance of mask features is 140 µm. Exposed window is 100 µm. ($W_1 - W_2 = 1.414 \times \text{Etch depth}$)

Chapter 4: Results and Discussions

4.1. Fabrication Results of Hollow Cylindrical Silicon Microneedle Array

Fabrication of hollow cylindrical silicon microneedle array was carried out as per the method described in sectioned 3.3.1. Figure 4.1 shows the SEM image of the microneedle array and Figure 4.3 shows the surface Profilometry analysis of fabricated hollow microneedles.

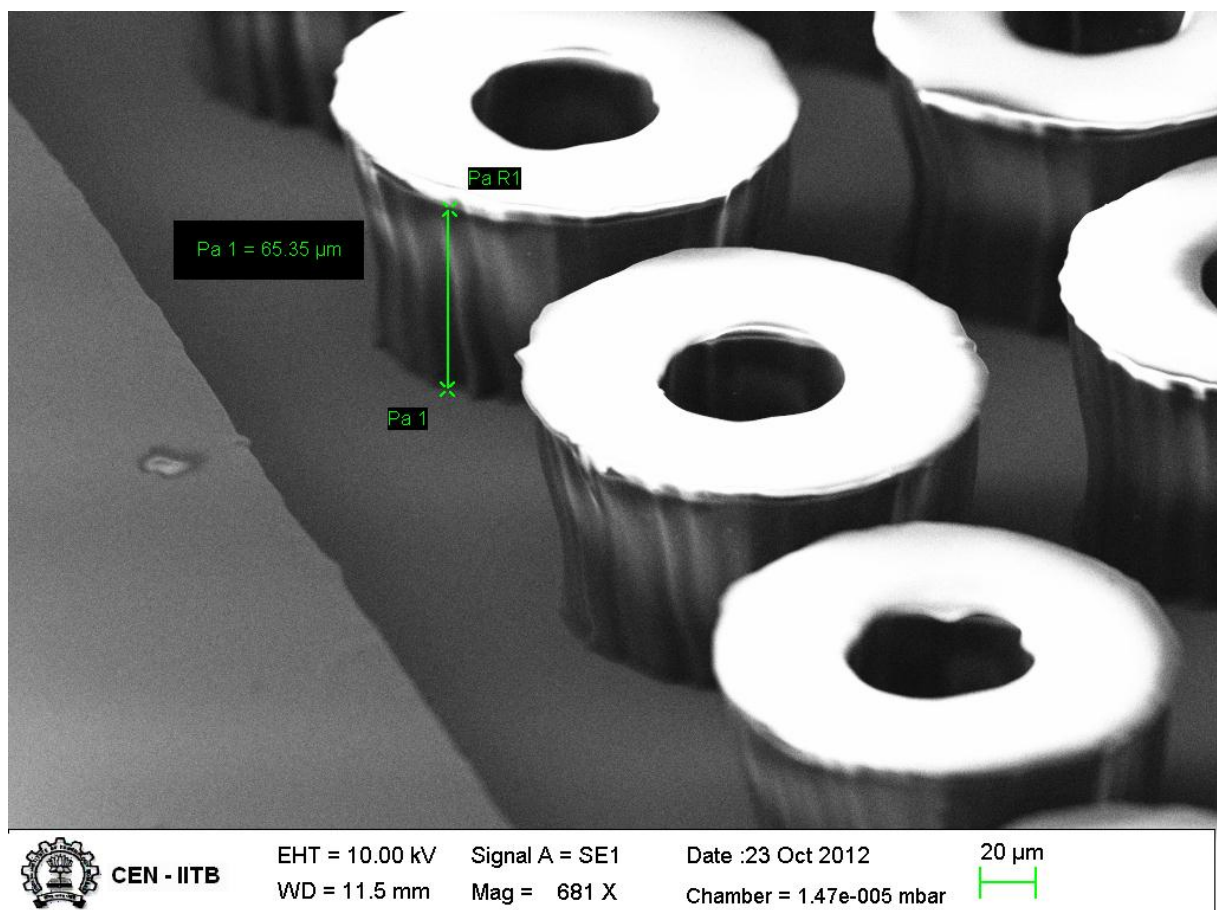


Figure 4.1: SEM image ($\alpha=60^\circ$) of a portion of the microneedle array showing height of an individual microneedle to be 65.35 μm .

The microneedles obtained were of 65 μm height ($n=10$, s.d. = 700 nm) which is comparable with the microneedle height obtained in the simulation carried out before starting fabrication process. Microneedles fabricated in this process by RIE, using optimized novel recipe of gases and other parameters, were of nearly vertical structure which, in its own credit, is quite ground-breaking. It surpasses the limitation of RIE in etching more than 10 μm . To the knowledge of the author, there has been no published report till date where a perfect vertical high-aspect ratio structure has been made out of silicon solely by using RIE. It is a common practice in research community to use deep reactive ion etching or DRIE (Bosch process) to fabricate high-aspect ratio vertical structure. DRIE uses gases like C_4F_8 (Octafluorocyclobutane) for deposition of a chemically inert passivation layer similar to Teflon and also requires high power and higher amount of gases as compared to RIE [19]. Further, experiments using this optimized recipe will ensure fabrication of structures with very high aspect ratio and low process cost and less time.

Slight indentation has been noticed at the base of the structures where the diameter of the base is marginally less from that at the top of the features. This can be attributed to the notching effect (as illustrated in Figure 2.9) due to thick layer of SU-8.

The average diameter of inner lumen of the microneedles was found to 67 μm ($n=10$) (Figure 4.2) which also is comparable to the simulation results. The average outer diameter of microneedles was 168 μm ($n=10$). A slight reduction in inner diameter and increase in outer diameter as well as center-to-center distance (Figure 4.4) of microneedle is noticed when compared to the actual mask patterns (Figure 3.7). This can be attributed to the reflow of thick SU-8 layer under high temperature during post-exposure baking. The SU-8 masks were not stripped because of the provision of further processes on the sample.

Surface profilometry (Figure 4.6) was also carried out to measure the feature heights on the microneedle arrays. Average height of microneedle obtained by profilometry was 52 μm ($n=20$). This result was significantly different than the average of actual heights measured by SEM studies. This can be attributed to the use of inadequate force on stylus (0.05 mg) during profilometry or non-uniformity of microneedle structures over different areas of the arrays.

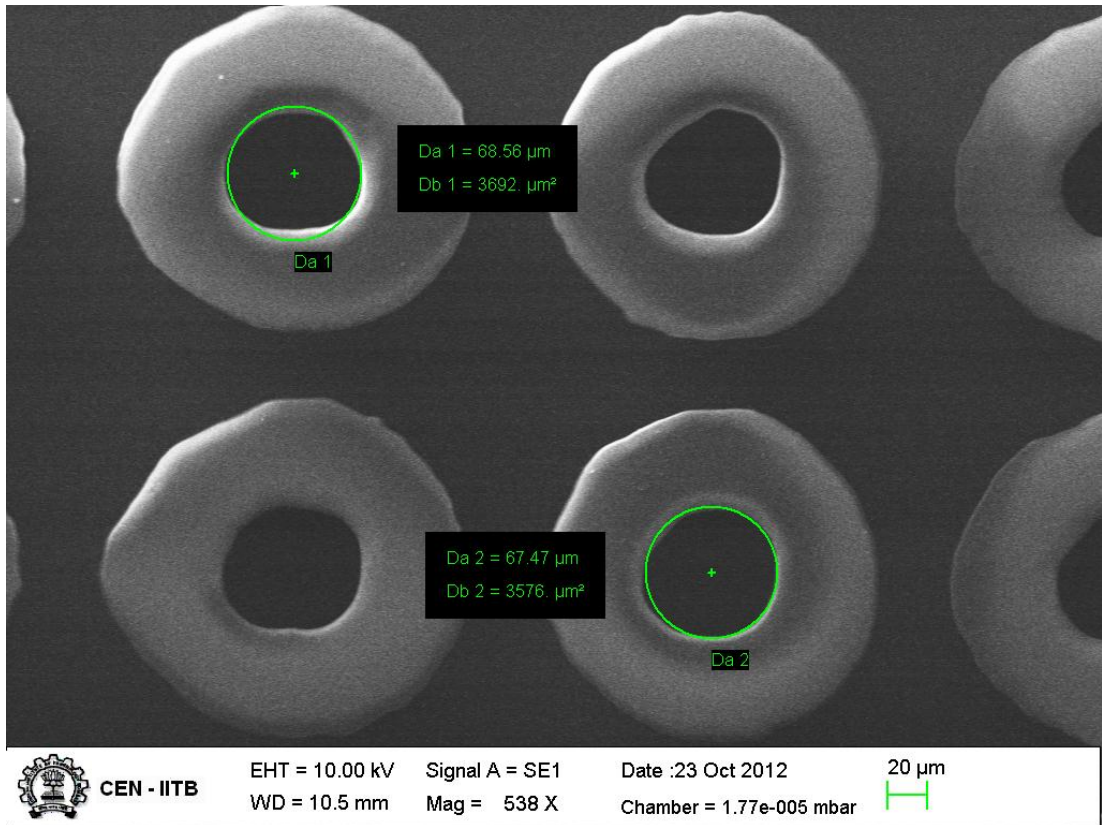


Figure 4.2: SEM image showing the diameter and area of the inner lumen of two individual microneedles.

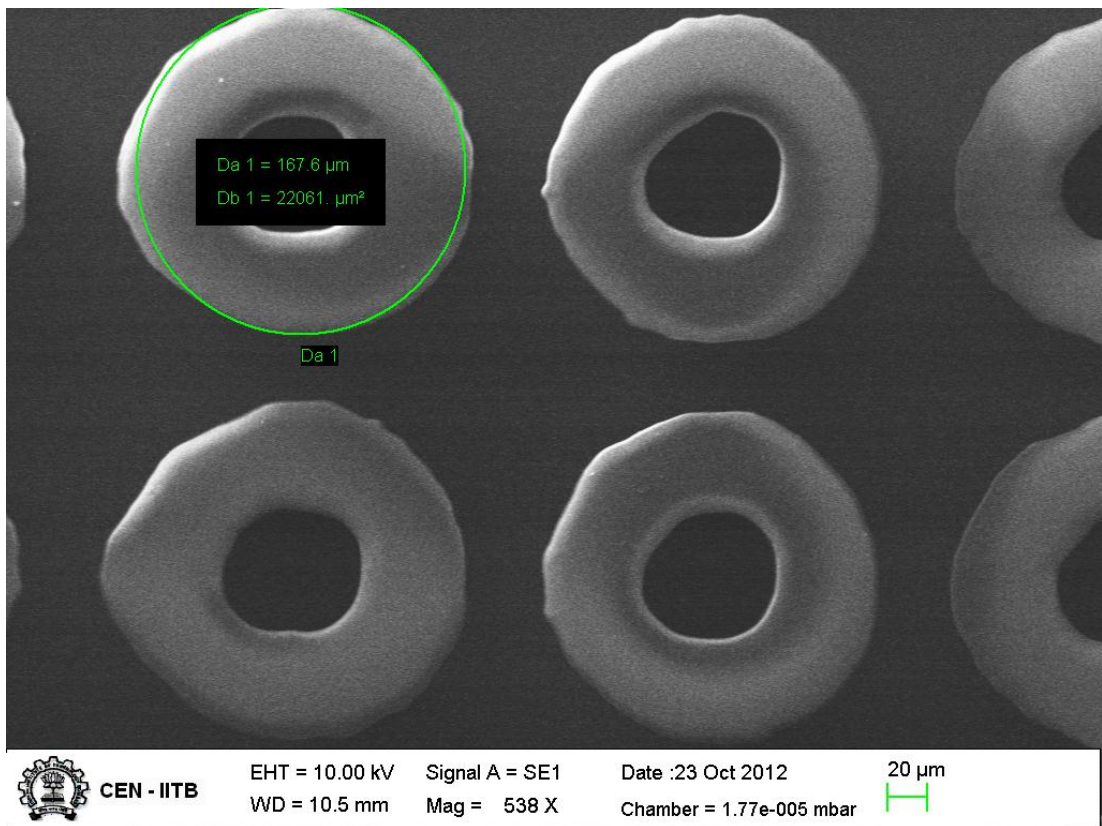


Figure 4.3: SEM image showing the outer diameter and total area of an individual microneedle.

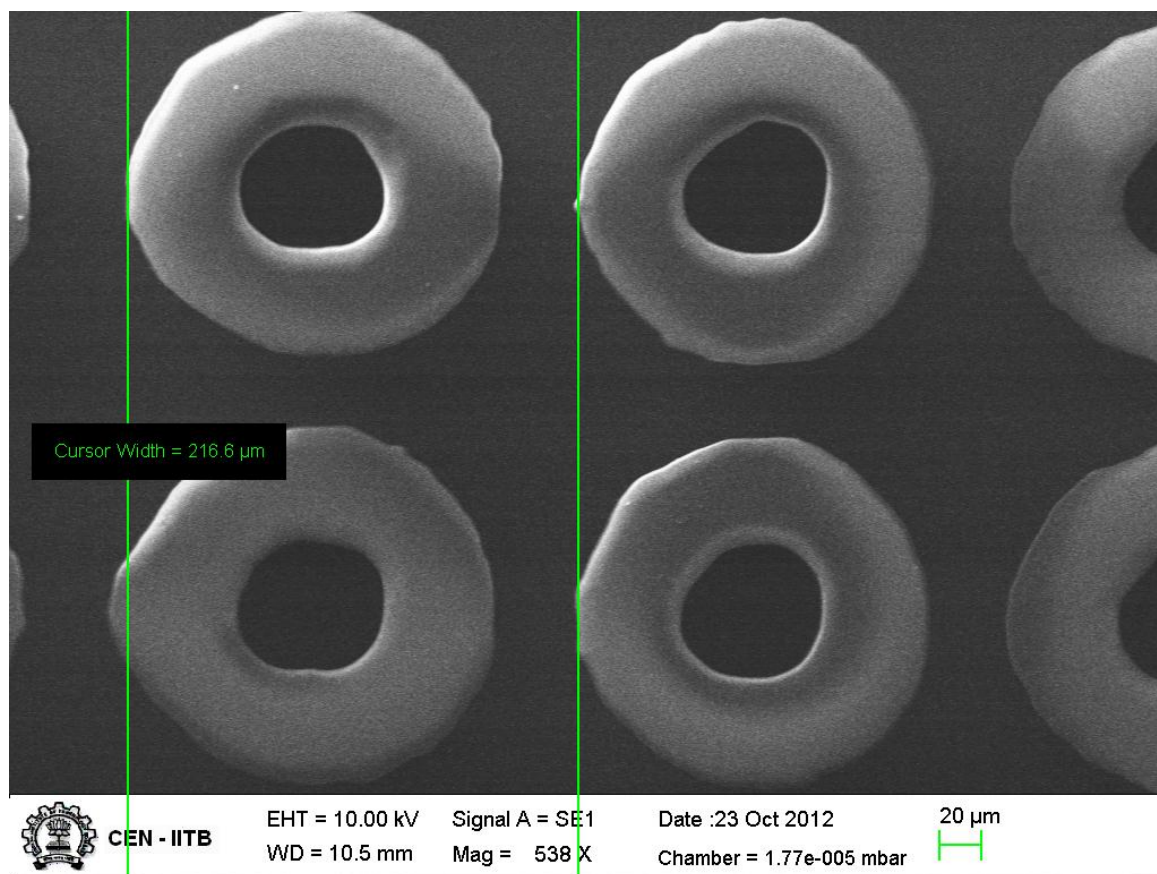


Figure 4.4: SEM image showing the center-to-center distance between two adjacent columns of microneedles.

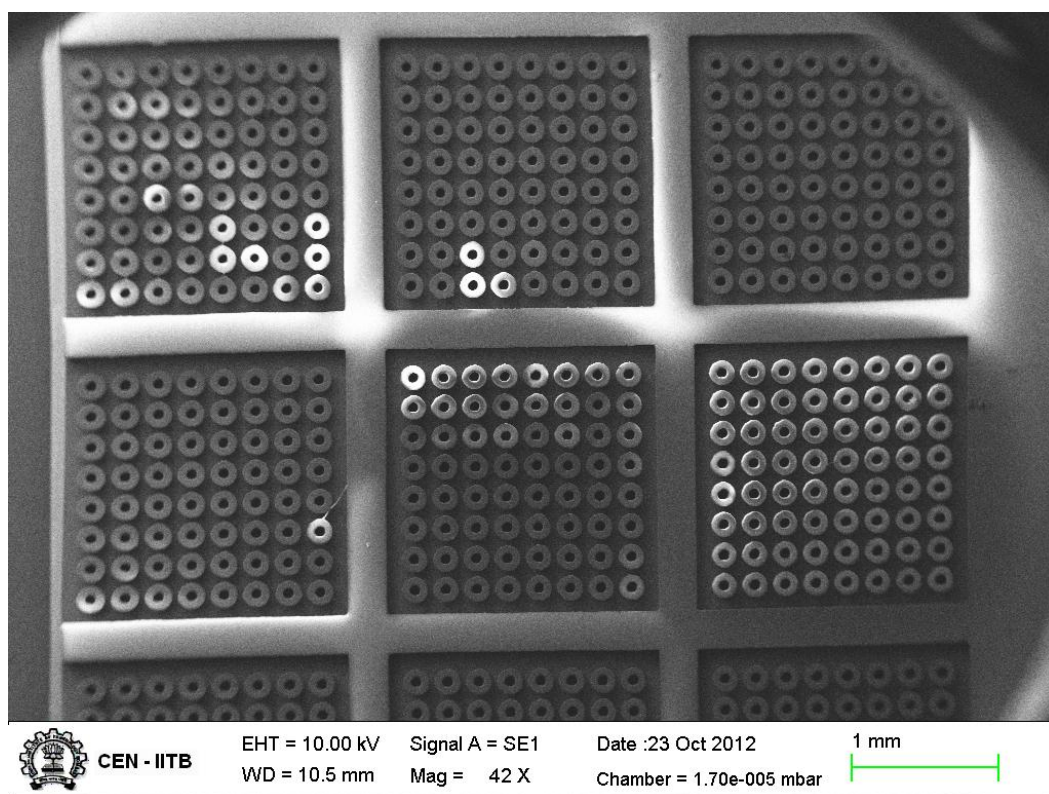


Figure 4.5: SEM image (bird's eye view) of an array of (8x8) hollow silicon microneedle arrays.

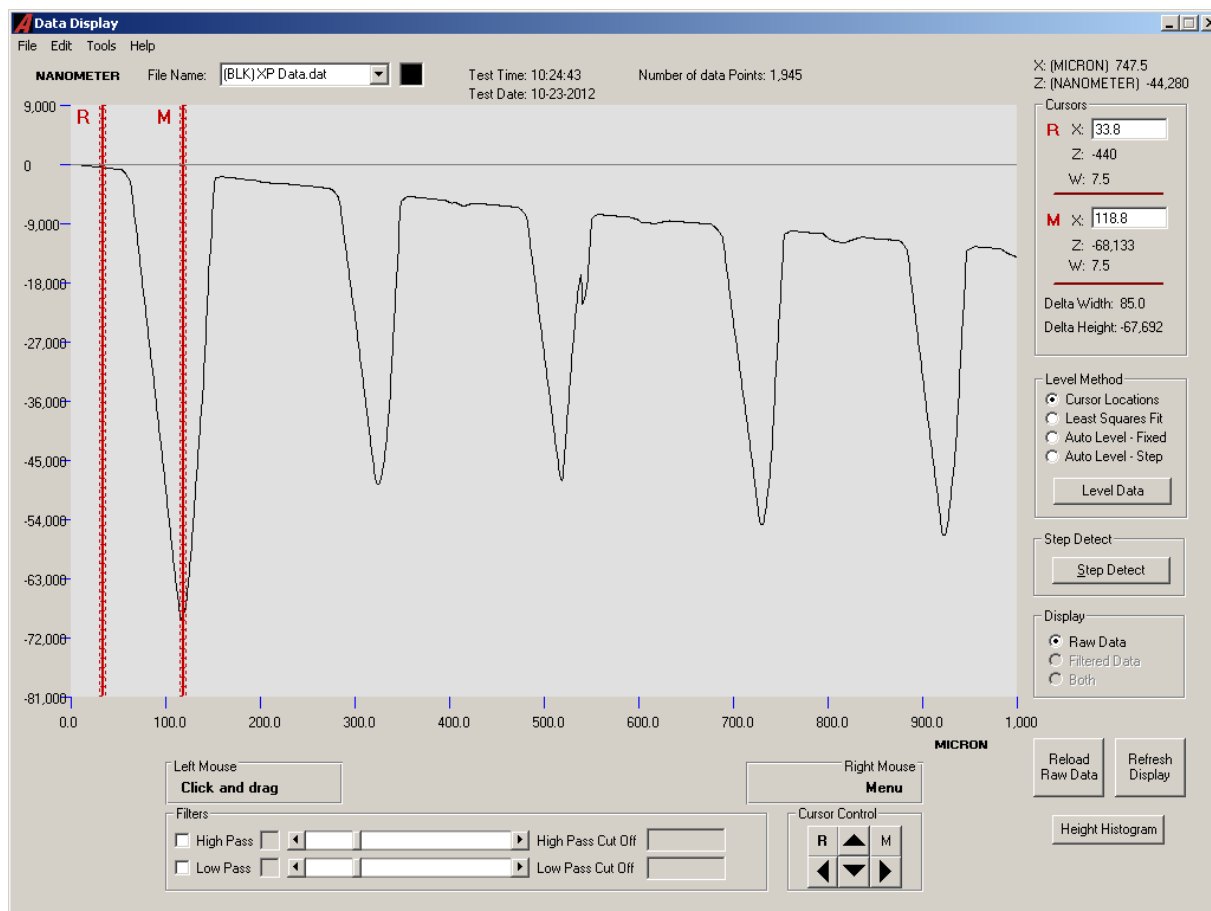


Figure 4.6: Surface Profilometry of microneedle array showing feature heights of five individual microneedles.

4.2. Fabrication Results of Tapered-tip Solid Silicon Microneedle Array

Fabrication of tapered-tip solid silicon microneedle arrays has been illustrated in section 3.3.2. Surface profilometry was carried out on resulting microneedle arrays to determine their feature heights (Figure 4.7). Average heights of microneedles found using profilometry was 66 μm (n=10). The tip diameter of almost all the microneedles was 40 μm (Figure 4.8). These findings support the results of simulation to a great extent. SEM studies on this sample could not be performed due to the lack of availability of slots on the NORDIKO metal sputter system for gold coating required for SEM imaging.

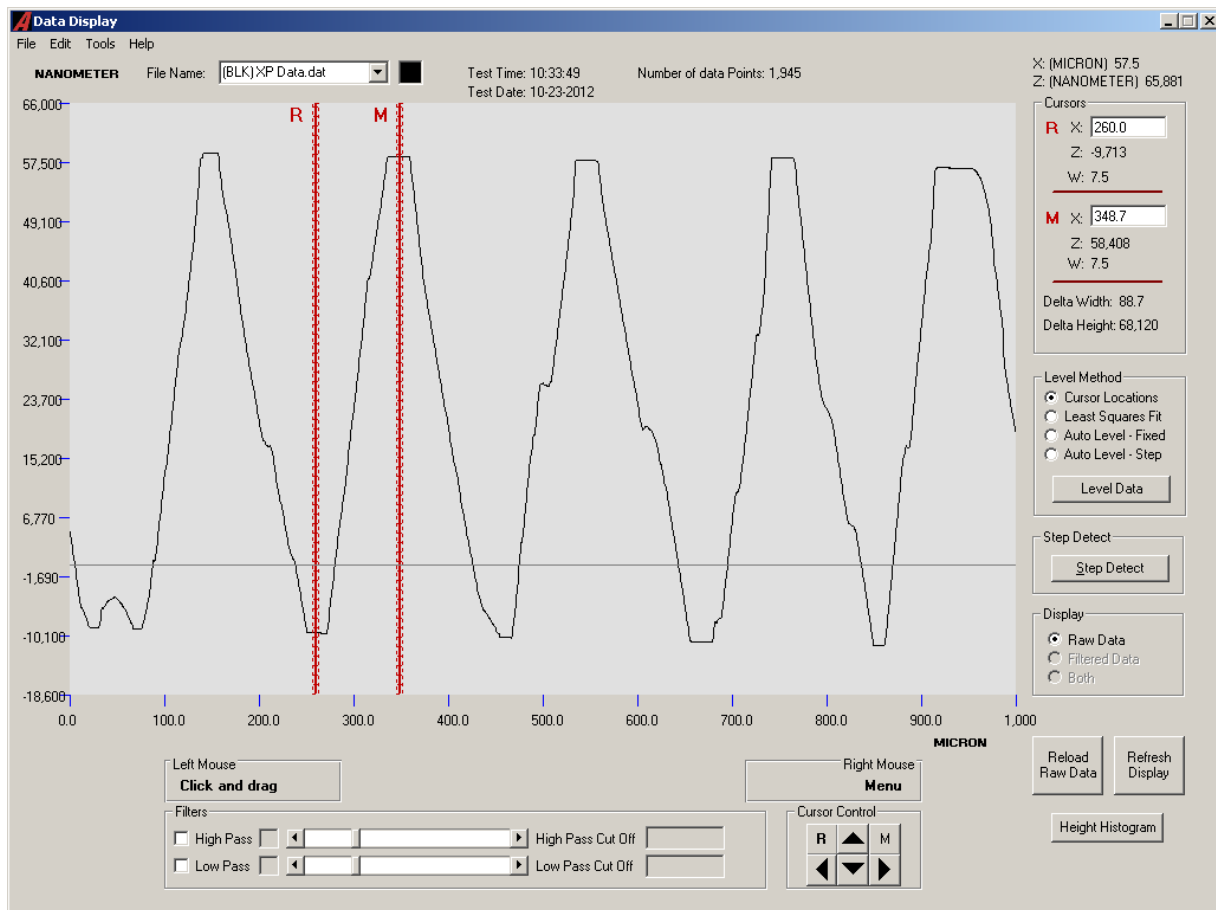


Figure 4.7: Surface Profilometry of microneedle array showing feature heights of five individual microneedles.

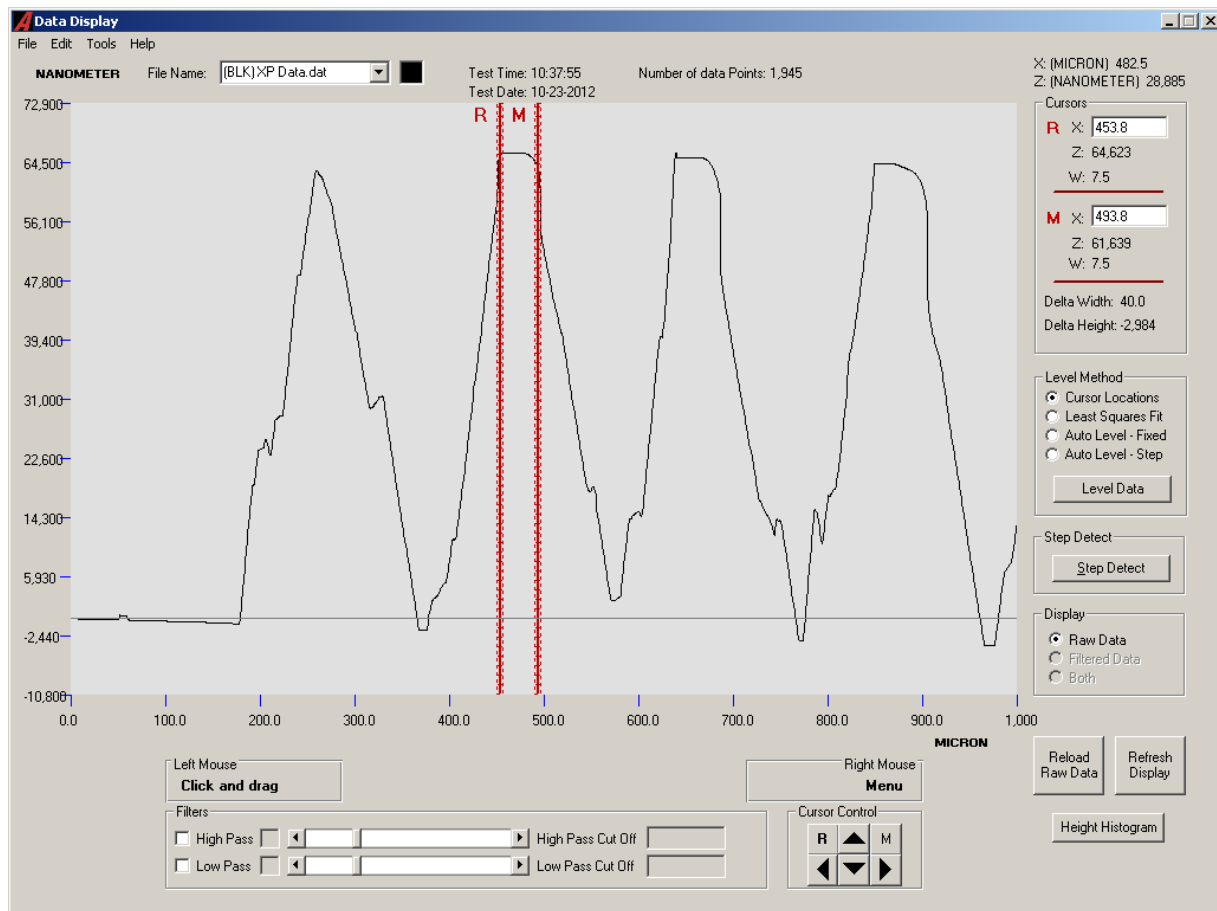


Figure 4.8: Surface Profilometry of microneedle array showing tip diameter of an individual microneedle.

Chapter 5: Conclusions and Future Work

The present study demonstrated the fabrication of microneedles which might be suitable for transdermal vaccination. The finding of optimized recipe for using RIE to etch high-aspect ratio structure surely demands prudent research. Based on the extensive reviews of previously reported works as covered in this article, the promising scope of microneedles in painless transdermal delivery of vaccines can evidently be realized.

Fabrication of dissolving polymeric microneedles for delivery of encapsulated vaccines and sharp-tip hollow microneedles for fluidic vaccine delivery poses greatest prospect in this field and hence shall be investigated, in future, along with their mechanical and fluidic characterization. The studies of efficient coating of different vaccines against diseases like influenza, hepatitis B, MMR, typhoid etc., improving their stability for proper induction of immune response – and its characterization, the effects of microneedles penetration on skin morphology and the kinetics of its recovery, shall be the primary focus of the next stage of this study.

References

1. Vaccines.gov (U.S. Department of Health and Human Services) (2012, Oct 18). Glossary [Online]. Available: http://www.vaccines.gov/more_info/glossary/index.html#v
2. WHO (2012, Oct 18). Vaccines [Online]. Available: <http://www.who.int/topics/vaccines/en/>
3. Delves *et al*, “Vaccines,” in *Roitt's Essential Immunology*, 12th ed. Wiley-Blackwell, 2011, ch. 13.
4. Historyofvaccines.org (The College of Physicians of Philadelphia) (2012, Oct 18). How vaccines work [Online]. Available: <http://www.historyofvaccines.org/content/how-vaccines-work>
5. Historyofvaccines.org (The College of Physicians of Philadelphia) (2012, Oct 18). Different Types of Vaccines [Online]. Available: <http://www.historyofvaccines.org/content/articles/different-types-vaccines>
6. Madhavi Y, “Vaccine policy in India,” *PLoS Med*, vol. 2, issue. 5, e127, pp. 387-391, May 2005, doi: 10.1371/journal.pmed.0020127.
7. India.gov.in (2012, Oct 19). Universal Immunisation Programme [Online]. Available: <http://india.gov.in/citizen/health/viewscheme.php?schemeid=1217>
8. Cdc.gov (Centers for Disease Control and Prevention) (2012, Oct 19). Vaccines & Preventable Diseases [Online]. Available: <http://www.cdc.gov/vaccines/vpd-vac/default.htm#basics>
9. Cdc.gov (Centers for Disease Control and Prevention) (2012, Oct 19). Immunization Schedules [Online]. Available: <http://www.cdc.gov/vaccines/schedules/index.html>
10. M.D. Plotkin and A. Stanley, *Mass Vaccination: Global Aspects - Progress and Obstacles* (Current Topics in Microbiology & Immunology), vol. 304, Springer-Verlag Berlin and Heidelberg GmbH & Co. K., 2006, ISBN: 978-3-540-29382-8. Available: <http://link.springer.com/book/10.1007/3-540-36583-4/page/1>
11. Cdc.gov (Centers for Disease Control and Prevention) (2012, Oct 19). Vaccine Administration [Online]. Available: http://www.cdc.gov/vaccines/pubs/pinkbook/downloads/appendices/d/vacc_admin.pdf
12. S. Mitragotri, “Immunization without needles,” *Nat. Rev. Immunol.*, vol. 5, issue. 12, pp. 905-916, Dec 2005.

13. R Cranenburgh (BioPharm International) (2012, Oct 20). Needle-Free Methods of Vaccination [Online]. Available:
<http://www.biopharminternational.com/biopharm/Downstream+Processing/Needle-Free-Methods-of-Vaccination/ArticleStandard/Article/detail/485192>
14. S. Bennett and C. Potter, "Pushing the boundaries of needle-free injection," *Drug Delivery Report*, pp. 24–27, 2006.
15. T. A. Peterson, "Microstructured transdermal systems for intradermal vaccine and drug delivery," *Pharm. Tech. Eur.*, vol. 18, issue.12, pp. 21–36, Dec 2006.
16. H. S. Garmory *et al.*, "The use of live attenuated bacteria as a delivery system for heterologous antigens," *J. Drug Target*, vol. 11, pp.471–479, 2003.
17. I. Lambkin *et al.*, "Toward targeted oral vaccine delivery systems: selection of lectin mimetics from combinatorial libraries," *Pharm. Res.*, vol. 20, issue. 8, pp. 1258–1266, 2003.
18. J. Beadle, "Preparing for pandemic," *Euro BioPharm Rev.*, pp. 50–54, 2006.
19. A Behl, "Transdermal Drug Delivery Using Microneedles," Dept. of BSBE, IIT Bombay, Mumbai, M.Tech. Dissertation, June 2012.
20. O. Huber, "Structure and function of desmosomal proteins and their role in development and disease," *Cell Mol. Life Sci.*, vol. 60, pp. 1872–1890, 2003.
21. J. Hadgraft, "Skin, the final frontier," *Int. J. Pharm.*, vol. 224, pp. 1–18, 2001.
22. B. G. Weniger and M. J. Papania (2012, Oct 20). Alternative vaccine delivery methods [Online]. Available: <http://www.spritze-ohne-nadel.de/sites/spritze-ohne-nadel.de/files/injex/studien/112%20WenigerPapania-AltVacDeliv-Chap61-Vaccines-Final-2008Feb.pdf>
23. M. R. Prausnitz, S. Mitragotri, R. Langer, "Current status and future potential of transdermal drug delivery," *Nature Reviews*, vol. 3, pp. 115–124, 2004.
24. M. Steinhoff *et al.*, "Keratinocytes in epidermal immune responses," *Curr. Opin. Allergy Clin. Immunol.*, vol. 1, pp. 469–476, 2001.
25. F. M. Hendriks *et al.* Mechanical Properties of Different Layers of Human Skin [Online]. Available: <http://www.mate.tue.nl/mate/pdfs/249.pdf>
26. R. T. Tregear, "The mechanical properties of skin," *J. Soc. Cosmetic Chemists*, vol. 20, pp. 467-477, 1969.
27. M. W. Ashraf *et al.*, "Fabrication and Analysis of Tapered Tip Silicon Microneedles for MEMS based Drug Delivery System," *Sensors & Transducers*, vol. 122, issue 11, pp. 158-172, Nov 2010.

28. P. K. Podder *et al.*, “Design, Simulation and Study of MEMS Based Micro-needles and Micro-pump for Biomedical Applications,” in *Proceedings of the 2011 COMSOL Conference*, Bangalore, India, 2011.
29. Y. C. Kim *et al.*, “Microneedles for drug and vaccine delivery,” *Adv. Drug Deliv. Rev.*, 2012, doi:10.1016/j.addr.2012.04.005.
30. Y. C. Kim *et al.*, “Delivery Systems for Intradermal Vaccination,” *Curr. Top. Microbiol. Immunol.*, vol. 351, pp. 77–112, 2011, doi: 10.1007/82_2011_123.
31. M. R. Prausnitz *et al.*, “Microneedle-based vaccines,” *Curr. Top. Microbiol. Immunol.*, vol. 333, pp. 369–393, 2009, doi: 10.1007/978-3-540-92165-3_18.
32. Clinical Resolution. MTS-Roller™ [Online].
Available: <http://www.microneedle.com/main/mts-personal.html>
33. J. Jiang *et al.*, “Coated microneedles for drug delivery to the eye,” *Invest. Ophthalmol. Vis. Sci.*, vol. 48, pp. 4038–4043, 2007.
34. Y. Zhang and L.C. Yu, “Single-cell microinjection technology in cell biology,” *Bioessays*, vol. 30, pp. 606–610, 2008.
35. Y. Xie *et al.*, “Controlled transdermal delivery of model drug compounds by MEMS microneedle array,” *Nanomedicine, Nanotechnology, Biology, and Medicine* 1, pp. 186, 2005, doi:10.1016/j.nano.2005.03.001.
36. L. M. Yu *et al.*, “A microfabricated electrode with hollow microneedles for ECG measurement,” *Sensors and Actuators, A: Physics*, vol. 151, pp. 19, 2009, doi:10.1016/j.sna.2009.01.020
37. B. Ma *et al.*, “A PZT Insulin Pump Integrated with a Silicon Micro Needle Array for Transdermal Drug Delivery,” in *Electronic Components and Technology Conference*, pp. 677-681, 2006.
38. M. W. Ashraf *et al.*, “Micro Electromechanical Systems (MEMS) Based Microfluidic Devices for Biomedical Applications,” *Int. J Mol. Sci.*, vol.12, issue. 6, pp. 3648–3704, 2011.
39. K. V. D. Maaden *et al.*, “Microneedle technologies for (trans) dermal drug and vaccine delivery,” *J. Control. Release*, 2012, doi:10.1016/j.jconrel.2012.01.042
40. J. A. Matriano *et al.*, “Macroflux (R) microprojection array patch technology: a new and efficient approach for intracutaneous immunization,” *Pharm. Res.* vol. 19, pp. 63–70, 2002.
41. Y. C. Kim *et al.*, “Formulation of microneedles coated with influenza virus-like particle vaccine,” *AAPS PharmSciTech*, vol. 11, issue. 3, pp. 1193–1201, 2010.

42. R. Luttge, "Integrated Lithographic Molding for Microneedle-Based Devices," *J. MEMS*, vol. 16, issue. 4, pp. 872-884, Aug. 2007, doi: 10.1109/JMEMS.2007.899339.
43. S. Liu, "The development and characteristics of novel microneedle arrays fabricated from hyaluronic acid, and their application in the transdermal delivery of insulin," *J. Control. Release*, vol. 161, pp. 933-941, 2012, doi:10.1016/j.jconrel.2012.05.030.
44. J. -H. Park, "Biodegradable polymer microneedles: Fabrication, mechanics and transdermal drug delivery," *J. Control. Release*, vol. 104, pp. 51-66, 2005, doi:10.1016/j.jconrel.2005.02.002.
45. P. Zhang, "Design and fabrication of MEMS-based microneedle arrays for medical applications," *Microsyst. Technol.*, vol. 15, pp. 1073-1082, 2009.
46. Z. Ding *et al.*, "Microneedle arrays for the transcutaneous immunization of diphtheria and influenza in BALB/c mice," *J. Control. Release*, vol. 136, pp. 71-78, 2009.
47. X.F. Chen *et al.*, "Site-selectively coated, densely-packed microprojection array patches for targeted delivery of vaccines to skin," *Adv. Funct. Mater.* vol. 21, pp. 464-473, 2011.
48. Y. Hiraishi *et al.*, "Bacillus Calmette-Guerin vaccination using a microneedle patch," *Vaccine*, vol. 29, pp. 2626-2636, 2011.
49. H.S. Gill *et al.*, "Cutaneous vaccination using microneedles coated with hepatitis C DNA vaccine," *Gene Ther.*, vol. 17, pp. 811-814, 2010.
50. M. Han *et al.*, "Improvement in antigen-delivery using fabrication of a grooves-embedded microneedle array," *Sensors and Actuators B*, vol. 137, pp. 274-280, 2009, doi:10.1016/j.snb.2008.11.017.
51. B. Chen *et al.*, "Silicon microneedles array with biodegradable tips for transdermal drug delivery," *Microsyst. Technol.*, vol. 14, pp. 1015-1019, 2008, doi: 10.1007/s00542-007-0530-y.
52. J. Ji *et al.*, "Microfabricated Silicon Microneedle Array for Transdermal Drug Delivery," *Institute of Physics Publishing, Journal of Physics*, Conference Series 34, pp. 1127-1131, 2006, doi:10.1088/1742-6596/34/1/186.
53. A. P. Raphael *et al.*, "Targeted, Needle-Free Vaccinations in Skin using Multilayered, Densely-Packed Dissolving Microprojection Arrays," *Small*, vol. 6, no. 16, pp. 1785-1793, 2010, doi: 10.1002/smll.201000326.
54. X. Chen *et al.*, "Improving the reach of vaccines to low-resource regions, with a needle-free vaccine delivery device and long-term thermostabilization," *J. Control. Release*, vol. 152, pp. 349-355, 2011, doi:10.1016/j.jconrel.2011.02.026.

55. X. Chen *et al.*, "Dry-coated microprojection array patches for targeted delivery of immunotherapeutics to the skin," *J. Control. Release*, vol. 139, pp. 212–220, 2009, doi:10.1016/j.jconrel.2009.06.029.
 56. M.A.F. Kendall, "Device for Delivery of Bioactive Materials and Other Stimuli," WIPO Patent, WO 2005/072630, Aug 11, 2005.
 57. M.W. Ashraf *et al.*, "Design, analysis and fabrication of MEMS-based silicon microneedles for bio-medical applications," in *Electrical Engineering/Electronics Computer Telecommunications and Information Technology (ECTI-CON), 2010 International Conference on*, pp.950-953, 19-21 May 2010.
 58. S. –J. Paik *et al.*, "In-plane single-crystal-silicon microneedles for minimally invasive microfluid systems," *Sensors and Actuators A*, vol. 114, pp. 276–284, 2004, doi:10.1016/j.sna.2003.12.029.
 59. S. P. Sullivan *et al.*, "Dissolving polymer microneedle patches for influenza vaccination," *Nature Medicine*, vol. 16, no. 8, 2010, doi:10.1038/nm.2182.
 60. F. J. Verbaan *et al.*, "Improved piercing of microneedle arrays in dermatomed human skin by an impact insertion method," *J. Control. Release*, vol. 128, pp. 80–88, 2008, doi:10.1016/j.jconrel.2008.02.009.
 61. D. V. McAllister *et al.*, "Microfabricated needles for transdermal delivery of macromolecules and nanoparticles: Fabrication methods and transport studies," *PNAS*, vol. 100, no. 24, pp. 13755–13760, Nov. 2003, doi: 10.1073/pnas.2331316100.
 62. J. Gupta *et al.*, "Kinetics of skin resealing after insertion of microneedles in human subjects," *J. Control. Release*, vol. 154, pp. 148–155, 2011, doi:10.1016/j.jconrel.2011.05.021.
 63. S. M. Bal *et al.*, "Advances in transcutaneous vaccine delivery: Do all ways lead to Rome?," *J. Control. Release*, vol. 148, pp. 266–282, 2010, doi:10.1016/j.jconrel.2010.09.018.
-

This project has been gracefully funded by National Program on Micro and Smart Systems (NPMASS). The fabrication works were carried out at the Centre of Excellence in Nanoelectronics (CEN), IIT Bombay. The simulation studies were carried out at Microelectronics Computation Laboratory (MCL) at Dept. of EE, IIT Bombay.